# Development of Steel Slit Wall Dampers with Embedded Condition Assessment Capabilities

2010

Andrés Jacobsen Pohlenz

# TABLE OF CONTENTS

**CHAPTER 6 Paint as a means for condition assessment**



**CHAPTER 7 Distributed online test to collapse**



**CHAPTER 8 Summary and conclusions**

**ACKNOWLEDGMENTS**

# CHAPTER 1

# Introduction

## 1.1 Background

In seismic design of steel structures, passive dampers have gained popularity as a response to the shortcomings of conventional structural design, for example [1], [2]. Their purpose is to concentrate hysteretic behavior in specially designed zones that undergo interstory drift levels smaller than those of other structural elements, thus delaying inelastic behavior in the gravity load-resisting elements of the structure.

Steel plate shear walls (SPSW hereafter) are one kind of passive damper device. A SPSW consists of steel plates which are connected to boundary beams and columns over the height of a frame. As a damper device, the SPSW concentrates damage. The level of damage in SPSWs can be used to evaluate the health of the structure after an earthquake.

### 1.1.1 Steel shear walls

Steel shear walls have been used for building design for both new constructions and seismic upgrades of existing structures. Steel shear walls, provided with heavy stiffening, are able to resist large lateral forces and dissipate earthquake-induced energy. Unstiffened thin plate steel shear walls were proposed in response to the high costs of heavy stiffening. Thin plate steel shear walls provide energy dissipation for small interstory drifts as the wall buckles [3]. This response is commonly accompanied by significant pinching in the hysteresis, but strength deterioration is compensated for by the development of a tension field. This approach was extended by experiments to investigate the behavior and failure mode of steel plate shear walls with different slenderness ratios [4], and the reduction of the earthquake-induced forces in beam-to-column connections when steel plate shear walls are used [5].

Slitted shear walls were originally introduced as a means of improving the seismic behavior of reinforced concrete walls [6], [7]. A type of passive damping device, that consists of a steel plate shear wall with vertical slits (SW hereafter) have been previously devised [8] (Figure 1.1). In this system, the steel plate segments between the slits behave as a series of flexural links, which undergo large flexural deformations relative to their shear deformation, providing a ductile response without significant out-of-plane stiffening of the wall. The stiffness and strength of the SWs can be controlled fairly independently of one another by changing the slit design (i.e., slit length, number of slit tiers, and distance between slits) [8], [9]. The introduction of slits in the SW limits the

out-of-plane deformation, therefore there is little need for out-of-plane stiffening [8]. The SW does not have to occupy the full beam span and may be integrated into the walls of residential buildings, where walls with doors or window openings may be the only locations where earthquake-resisting elements can be installed.

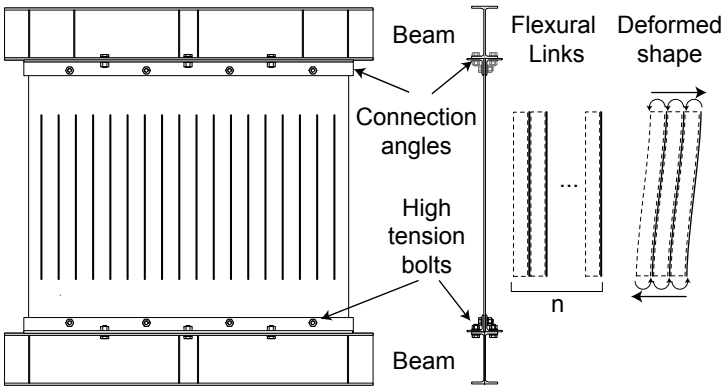


Figure 1.1. Slitted Steel Shear Wall

### 1.1.2 Condition Assessment – Health Monitoring

Structural condition assessment [10] focuses on techniques for evaluating the integrity of a structure after an earthquake event to ascertain the danger that it represents for re-occupation of the building. This evaluation can be performed through health-monitoring (for example [11], [12]) or through performance-evaluation analyses that rely on detailed computer models of the structure. The health-monitoring process involves the observation of a structural system over time using periodically sampled dynamic response measurements from an array of sensors, the extraction of damage-sensitive features from these measurements, and the statistical analysis of these features to determine the current state of system health. Unfortunately, the required technologies remains untested against actual large earthquakes, and the cost of implementing it restricts its use to important structures, such as large spatial structures, bridges, dams and high-rise buildings. The small number of sensors used in these structures is only sufficient to identify the existence of damage by observing global changes in the vibration modes and frequencies. These restrictions encourage the development of a more straightforward method of estimating the damage sustained by a structure, where the visual inspection of structural elements (SWs in this particular case) can determine the level of damage that the full structure has sustained based on the maximum drift angles that the structure was designed to withstand.

### 1.1.3 Online Test

Two approaches are commonly used for simulating the earthquake responses of structures. One is the numerical simulation by which the equations of motion are formulated for a spatially discretized model, and solved numerically by time integration algorithms in the time domain. The other is the experimental simulation by imposing the ground motions directly on the tested specimens. In the numerical simulation, a sophisticated model with a larger number of degrees of

freedom can be implemented to provide accurate responses. The solution procedure for this large model, however, is time-consuming, and the convergence of this solution procedure is always a critical problem especially when material and geometric nonlinearities are considered simultaneously. The experimental approach cannot handle full-scale structural models effectively. It is very expensive and nearly impracticable to test a full-scale model of such a structural system, all the while, a reduced-scale model is unable to duplicate the prototype behavior particularly when it involves strong nonlinearities. Therefore, it is not necessarily easy to accurately simulate the seismic responses of a large and complex structural system by using either a single analytical method or a single experimental method.

The online hybrid test [13]-[15] (also called the pseudo dynamic test) is appealing since it can make use of the benefits of both the analysis and test methods. In this test system, the equations of motion are solved numerically in a computer, while the restoring forces are obtained from a physical test. The online hybrid test has a history of more than thirty years, and many applications have demonstrated its effectiveness. The test, when combined with substructuring techniques, is called a substructure online hybrid test, and is particularly appealing for the earthquake response simulation of large-scale structures [16]-[24].

## 1.2 Objective

Adding condition assessment capabilities to SWs has the benefit of extending their application to monitoring purposes, whilst retaining their original function as damper devices. In this manner the SW damper fulfills a double purpose. In this study, a modified slit design for SW is proposed to include condition assessment capabilities. Unlike the conventional SWs in which the distance between slits is constant, the proposed SW features slitting with unequal distances. This enables strain patterns that vary significantly over the plate and an eventual gradual spread of yielding with the increase of interstory drift. This gradual spread is the key for this application of condition assessment, in which the correlation between the yield region and the maximum interstory drift is employed. A reliable method is needed to identify of the yield region in the unequally slitted SWs. In practice, the problem of recording the spreading of the maximum strains through the full extent of a SW has not been solved for the application required in this study. Brittle paint offers an inexpensive alternative to record the spreading of strains in the plate through flaking since the flaking of brittle paint provides a permanent recording of the maximum strains experienced within the SW. An evaluation of the viability of using commercially available paints is conducted, focusing on the selection of a compound that flakes under strain, the evaluation is conducted experimentally supported by analytical verifications.

The difference in the buckling drift angle between flexural links of different aspect ratios presents an alternative to achieve condition assessment capabilities. The possibility of using link rotation angles is explored for use as a parameter for the evaluation of damage sustained by an SW with unequal slitting.

In an initial stage the monitoring system is intended to identify a number of drift angles that can

be considered as fundamental in the design stage of buildings with a small margin of error. The key drift angles that need to be identified are: the limit state of elastic behavior of the structure, the limit state for life safety condition and the limit state for heavy damage in the structure.

To summarize, the objectives of this study are to explore the possibility of introducing condition assessment capabilities to SW dampers. Two alternatives to achieve this objective are proposed, namely the correlation between the strain patterns developed in the SW with the maximum drift angles achieved, and the correlation between the initiation of inelastic buckling of the flexural link and the drift angles. A series of quasi-static and online tests were conducted to investigate the seismic behavior of the proposed SW designs and provide information for engineers to facilitate the implementation of these techniques.

## 1.3 Organization

This dissertation consists of eight chapters. Chapter 1 presents the introduction of this study and Chapter 8 presents the conclusions. Chapters 2 to 7 constitute the main part of the dissertation: (1) a summary of previous research on steel shear walls; (2) development of slit walls with unequal slitting; (3) online test of a three-story building with slit walls; (4) buckling initiation as a means for condition assessment; (5) paint as a means for condition assessment; and (6) distributed online test to collapse. The contents of these six chapters are summarized as follows:

Chapter 2 presents a review of the most significant experimental and numerical research on steel plate shear walls. Special attention is given to steel plate shear walls with perforations. Perforations in the steel plates can significantly reduce the design forces on boundary elements by weakening the shear walls. Several alternatives that have been considered to reduce the strength of the infill plates are presented, comprising the introduction of circular openings and vertical slits.

Chapter 3 presents the conceptual work to introduce condition assessment capabilities in SWs through the tracing of strains. Several modified slit designs are evaluated and compared to obtain the most suitable for condition assessment purposes. Afterwards, the condition assessment performance of the SWs is studied, and design equations are proposed to resolve the basic properties (strength and stiffness) of the SW. A parametric study is conducted on isolated flexural links to quantify their performance with regards to energy dissipation and out-of-plane buckling initiation. Empirical equations based on geometric characteristics are developed to predict the behavior of flexural links.

Chapter 4 presents a practical application of the SW design proposed in Chapter 3 and the testing of a structure with an online testing scheme. The design of the prototype structure, and the SW is examined. A brief description of the online test scheme and substructuring techniques is also presented. The results from the online test are examined as the overall behavior of the structure featuring unequally slitted SW, and also the local behavior of these SW is discussed. Finally the results from cyclic tests that followed the online test are discussed to provide insight on the behavior of SW under large lateral drift demands.

Chapter 5 presents an alternative method of achieving condition assessment capabilities through

the tracing of the inelastic buckling behavior of the flexural links in slit walls Two types of flexural links, based on the independent behavior of flexural links, are introduced to achieve this objective: (1) "Monitoring links" that develop inelastic buckling at predetermined drift angles and (2) "Cushion links" that prevent the spreading of strains in between the monitoring links. An experimental verification on scaled specimens of the design proposed follows. The hysteretic performance, as well as the monitoring capabilities of the new design of SWs are evaluated.

Chapter 6 presents a means of recording through the flaking of paint the strain patterns that develop in the SW presented in Chapter 3. A parametric study on different types of commercially available paints is conducted. In the study, several compounds are tested under monotonic load. The strain patterns developed in the paint are compared to finite element model results. Later in the chapter, the performance of the spreading of the flaking of the paint is examined under experimental conditions in three SW specimens subjected to the loadings described in Chapter 4.

Chapter 7 presents an extension of the online testing framework used in Chapter 4 in order to geographically distribute the physical testing substructures. The proposed framework is then applied to evaluate the seismic performance of large-scale steel structures from the onset of damage through collapse. In this approach, only the critical subassemblies of the structural system leading to the collapse mechanism are evaluated experimentally while the global response of the remaining structure is captured numerically. The selection of the subassemblies and the sensitivity in enforcing boundary conditions between experimental and numerical substructures in order to capture the initiation of collapse is examined in detail. The hybrid test results are compared to a full scale earthquake simulator test to examine both the global response and the distribution of stresses in the frame.

# REFERENCES


[1] T.T. Soong and G.F. Dargush, Passive energy dissipation systems in structural engineering, New York: Wiley & Sons, 1997.

[2] C. Christopoulos, A. Filiatrault, and V.V. Bertero, *Principles of passive supplemental damping and seismic isolation*, IUSS Press University of Pavia, Italy, 2006.

[3] H. Mimura and H. Akiyama, "Load-deflection relationship of earthquake–resistant steel shear walls with a developed diagonal tension field," *Trans. AIJ*, vol. 260, 1977, pp. 109 - 144.

[4] V. Caccese, M. Elgaaly, and R. Chen, "Experimental study of thin steel-plate shear walls under cyclic load," *J. Struct. Eng.-ASCE*, vol. 119, 1993, pp. 573-573.

[5] R.G. Driver, G.L. Kulak, D.J.L. Kennedy, and A.E. Elwi, "Cyclic test of four-story steel plate shear wall," *J. Struct. Eng.-ASCE*, vol. 124, 1998, pp. 112-130.

[6] K. Mutoh, O. Miyashita, M. Osada, and H. Kanayama, "Stress and deformation of slit wall, using FEM," *Summaries of Technical Papers of Annual Meeting AIJ*, Chugoku, Japan: 1968, pp. 543-544.

[7] S. Omori, K. Toyama, T. Cho, and T. Takahashi, "Test on RC shear wall with slits,"

*Summaries of Technical Papers of Annual Meeting AIJ*, Kanto, Japan: 1966, pp. 204-205.

[8] T. Hitaka and C. Matsui, "Experimental study on steel shear wall with slits," *J. Struct. Eng.-ASCE*, vol. 129, 2003, pp. 586 - 595.

[9] T. Hitaka, C. Matsui, and J. Sakai, "Cyclic tests on steel and concrete-filled tube frames with Slit Walls," *Earthq. Eng. Struct. D.*, vol. 36, 2007, pp. 707 - 727.

[10] A.E. Aktan, D.N. Farhey, A.J. Helmicki, D.L. Brown, V.J. Hunt, K.L. Lee, and A. Levi, "Structural identification for condition assessment: experimental arts," *J. Struct. Eng. - ASCE*, vol. 123, 1997, pp. 1674 - 1684.

[11] S.W. Doebling, C.R. Farrar, and M.B. Prime, "A summary review of vibration-based damage identification methods," *Shock Vib. Dig.*, vol. 30, 1998, pp. 91-105.

[12] H. Sohn, C.R. Farrar, F.M. Hemez, D.D. Shunk, D.W. Stinemates, B.R. Nadler, and J.J. Czarnecki, *A review of structural health monitoring literature: 1996–2001.*, Cambridge: Los Alamos National Laboratory, 2003.

[13] Takanashi K, Udagawa K, Tanaka H. Earthquake response analysis of steel frames by computer-actuator online system. *Proceedings of the 5th Japan Earthquake Engineering Symposium*, November 1978; 1321-1328.

[14] Mahin SA, Shing PB. Pseudodynamic method for seismic testing. *Journal of Structural Engineering*, ASCE 1985; **111**(7): 1482-1501.

[15] Shing PB, Nakashima M, Bursi OS. Application of pseudodynamic test method to structural research. Earthquake Spectra 1996; **12**(1): 29-56.

[16] Nakashima M, *et al*. Feasibility of pseudo dynamic test using substructuring techniques. *Proceedings of 9th World Conference on Earthquake Engineering*, Tokyo, 1988, **4**: 47-52.

[17] Nakashima M, Kaminosono T, Ishida M, Ando K. Integration techniques for substructure pseudodynamic test. *Proceedings of 4th U.S. National Conference on Earthquake Engineering*, Palm Springs, CA, 1990; **2**: 515-524.

[18] Tsutsumi H, Sato K, Ando K. Substructure pseudo dynamic test with rotation control. *Proceedings of 4th U.S. National Conference on Earthquake Engineering*, Palm Springs, CA, 1990; **2**: 525-534.

[19] Kanda M, Adachi J, Shirai N, Nakanishi M. Implicit integration scheme based on initial stress method for substructure online hybrid test. *Journal of Structural and Construction Engineering*, Architectural Institute of Japan, 1995; **473**: 75-84 (in Japanese).

[20] Kusunoki K, Nakano Y, and Okada T. Substructure online hybrid test of reinforce concrete column. *Journal of Structural Engineering*, Architectural Institute of Japan, 1998; **44B**: 141-148 (in Japanese).

[21] Ohi K, Lin X, Takanashi K. Sub-structure pseudo-dynamic test scheme suitable for bending-shear type flexible steel frames. *Journal of Structural and Construction Engineering*, Architectural Institute of Japan, 2001; **540**: 49-55 (in Japanese).

[22] Maeda M, Kang D, Tanaka K, Inoue N. Evaluation of post-earthquake seismic capacity of reinforced concrete buildings by sub-structural pseudo-dynamic testing, Part 1 and 2. *Technical Summary of Annual Convention*, Architectural Institute of Japan, 2002; Structure

**IV**: 213-216 (in Japanese).

[23] Wu B, Xu G, Wang Q, Williams SM. Operator-splitting method for real-time substructure testing. *Earthquake Engineering and Structural Dynamics,* 2006; **35**:293-314.

[24] Magonette G. Development and application of large-scale continuous pseudo-dynamic testing techniques. *Philosophical Transactions of The Royal Society of London* 2001; **A**(359):1771–1799.

# LIST OF PUBLICATIONS

## *Journal papers (full paper reviewed by multiple reviewers and published in archival journals):*

[1] **A. Jacobsen**, T. Hitaka, M. Nakashima, "Online Test of Building Frame with Slit-Wall Dampers Capable of Condition Assessment", *Journal of Constructional Steel Research* **66**, 2010, pp.1320 – 1329.

[2] T. Hitaka, **A. Jacobsen**, "Cyclic tests on RC-steel shear plate composite wall system applicable in beam spans with large openings", *Composite Construction in Steel and Concrete VI,* Colorado, USA, 2010 (in print).

[3] T. Wang, G. Mosqueda, **A. Jacobsen**, M. Cortes-Delgado, "Performance evaluation of a distributed hybrid test framework to reproduce the collapse behavior of a structure", *Earthquake Engineering and Structural Dynamics* (under review).

## *Conference paper (abstract reviewed by multiple reviewers and presented in international conferences):*

[4] **A. Jacobsen**, T. Hitaka, Y. Murata, J. McCormick, T. Wang, and M. Nakashima, "Condition assessment application of steel shear walls with slits," *Proceedings of the 14th World Conference on Earthquake Engineering*, Beijing, China: International Association for Earthquake Engineering, 2008.

[5] **A. Jacobsen**, M. Cortes-Delgado, T. Wang, G. Mosqueda, M. Nakashima. "Distributed online hybrid test of a four-story steel moment frame using a flexible test scheme". *Proceedings of the 3rd International Conference on Advances in Experimental Structural Engineering*, San Francisco, California, USA, 2009.

[6] **A. Jacobsen**, M. Nakashima, "Development of slitted steel shear walls for structural condition assessment", *Proceedings of the 5th World Conference on Structural Control and Monitoring*, Tokyo, Japan, 2010.

[7] Wang, T., **Jacobsen, A.**, Cortes-Delgado, M., and Mosqueda, G., "Distributed online hybrid test of a four-story steel moment frame using flexible test scheme", *Proceedings of the 9th US National and 10th Canadian Conference on Earthquake Engineering*, Toronto, Canada, 2010

## *Technical papers presented at domestic conferences:*

[8] **A. Jacobsen**, T. Hitaka, and M. Nakashima, "Cyclic test on new coupled wall for a damage control system". *Proceedings of Technical Papers of Kinki Branch*, 2008; No.**48**: pp. 213-216.

[9] **A. Jacobsen**, T. Hitaka, and M. Nakashima, "Cyclic test on new coupled wall for a damage control system". *Summaries of Technical Papers of Annual Meeting AIJ*, Chugoku, Japan. 2008; **C1**: pp. 959-960.

[10] **A. Jacobsen**, S. Furukawa, T. Hitaka, and M. Nakashima, "Online test of a three-story steel frame with slit walls". *Proceedings of Technical Papers of Kinki Branch*, 2009; No.**49**: pp.

329-332.

[11] **A. Jacobsen**, S. Furukawa, T. Hitaka, and M. Nakashima, "Online test of a three-story steel frame with slit walls". *Summaries of Technical Papers of Annual Meeting AIJ*, Tohoku, Japan. 2009; **C1**: pp. 847-848.

[12] **A. Jacobsen**, T. Okamura, and M. Nakashima, "Hysteretic Behavior of Slit Walls. Part 1: Strain Distribution for Condition Assessment". *Proceedings of Technical Papers of Kinki Branch*, 2010, No. **50**; pp. 277-280.

[13] T. Okamura, **A. Jacobsen**, and M. Nakashima, "Hysteretic behavior of slit walls. Part 2: Link Buckling for Condition Assessment". *Proceedings of Technical Papers of Kinki Branch*, 2010. No. **50**; pp. 281-284

[14] **A. Jacobsen**, T. Okamura, and M. Nakashima, "Performance of Unequally Slitted Steel Wall Under Large Lateral Drift Demands. Part 1: Condition Assessment through Strain Pattern Identification". *Summaries of Technical Papers of Annual Meeting AIJ*, Hokuriku, Japan. 2010; **C1**: pp. 1017 - 1018.

[15] T. Okamura, **A. Jacobsen**, and M. Nakashima, , "Performance of Unequally Slitted Steel Wall Under Large Lateral Drift Demands. Part 2: Condition Assessment through Link Buckling". *Summaries of Technical Papers of Annual Meeting AIJ*, Hokuriku, Japan. 2010; **C1**: pp. 1019 - 1020.

# CHAPTER 2

# Summary of Previous Research

## 2.1 Introduction

Steel plate shear walls (SPSW hereafter) are lateral force resisting elements that can resist both wind and earthquake induced forces. A SPSW consists of a steel plate, which is connected to boundary beams and columns of a structure. The walls can be stiffened or unstiffened with respect to the out-of-plane deformations. The main advantages of using SPSWs are their high ductility, high initial stiffness, and high energy dissipation capacity. In comparison to reinforced concrete shear walls, SPSWs are much lighter, which reduces the gravity loads to be transferred to the foundation. Furthermore, the use of SPSWs allows for faster construction as it allows for pre-fabricated assemblies and foregoes the curing time needed for proper concrete. These considerations can significantly reduce construction costs.

The design philosophy for SPSWs varies. In North America prior to the 1980s, the philosophy was to prevent shear buckling of the steel plate by using either thick plates or by adding stiffeners. Heavily stiffened steel plates are used in Japan to ensure that the wall panel achieves its full plastic strength prior to out-of-plane buckling. After the work of Thorburn et al. [1], the design philosophy in North America moved towards the use of thin unstiffened plates. In this type of walls, the shear is resisted primarily by a diagonal tension field that develops in the plates after they have buckled and the overturning moment is resisted by axial coupling of column loads. This design philosophy is adopted in the current American [2] steel design standards.

### 2.1.1 Organization

This chapter is divided into two sections. First, the research background on SPSW is presented. A summary of the most significant experimental and numerical research conducted in Japan and the United States since SPSWs were introduced.

In the second section of this chapter, a summary of the research on SPSW with perforations is presented. Perforations in the steel plates can significantly reduce the design forces on boundary elements by weakening the shear walls. Several alternatives that have been considered to reduce the strength of the infill plates are presented, comprising the introduction of circular openings and vertical slits.

## 2.2 Steel shear walls research background

During the past three decades, the research on SPSWs has been divided into two distinct categories: those in which the steel plates are prevented from buckling and those that rely on the post-buckling strength of the steel panels. Studies in Japan [3] and the United States have been conducted on SPSWs that were designed not to buckle under extreme lateral loading. In the 1980s, however, the idea of employing the post-buckling strength of the infill steel plates gained wide attention from researchers in North America [1], [4]-[6] and England [7]-[9]. A number of quasi-static cyclic tests have been reported since 1983 to address the issue of the post-buckling behavior of SPSWs. These studies have examined the behavior of steel plates throughout the entire range of loading, from elastic to plastic and from pre-buckling to post-buckling stages. A brief review of studies conducted on SPSWs is presented in the following.

### 2.2.1 Takahashi *et al.* (1973)

Takahashi, *et al.* [3] conducted a series of experimental and analytical studies on stiffened thin SPSWs. The objective of the tests was to investigate the behavior of thin stiffened SPSW systems as an alternative to concrete shear walls.

In the first series of tests, twelve one-story specimens with overall dimensions of 2100 mm width by 900 mm height were tested. The parameters considered for the study were:

(1) The spacing and width of stiffeners on both sides or one side of the steel panels, where three arrangements were considered.

(2) The steel plate thickness, where thicknesses of 2.3, 3.2 and 4.5 mm were considered.

Each shear panel was attached with high-strength bolts to a very stiff rectangular pin jointed frame. A compressive force was applied in one diagonal direction of the frame producing a state of pure shear stresses on the specimens.

The test results showed that all the specimens underwent large deformations and exhibited a very stable and ductile behavior. Some of the specimens with small transverse stiffeners showed elastic buckling. Plastic buckling occurred in other specimens. After buckling the stiffness of the panels gradually decreased as the tension field developed in the plate. In general, the hysteresis curves were S-shaped for most of the specimens, except in those specimens that were heavily reinforced with wide stiffeners. Shear deformations larger than 0.1 rad were reported for the heavily stiffened specimens. Figure 2.1 shows the hysteretic curves of the two specimens made out of 2.3 mm thick steel plate, one with no stiffeners (Figure 2.1 (a)) and the other heavily reinforced with horizontal and vertical stiffeners (Figure 2.1 (b)).

In the second series of tests, two full-scale one-bay two-story SPSW specimens, were tested under cyclic horizontal load. The test specimens differed from one another in that one covered the full beam span and the other considered a door size opening in each story. To provide similar shear stiffness and strength, the specimen with openings was made of 6 mm thick steel plate while the specimen without opening was made of 4.5 mm thick plate. The design of the test specimens was based on the design principles obtained through the first series of tests. The design criteria ensured

that the web plates yielded before the plate buckled out-of-plane. However, once the elastic limit of the steel plates was exceeded, only local buckling of the web was observed between the stiffeners.

Both full-scale specimens showed robust and stable hysteresis loops and large energy dissipation capacity. A monotonic finite element analysis of the specimens was carried out under the assumptions of no out-of-plane buckling for the steel plates and bi-linear stress-strain relationship for the steel material. Despite the simplicity of the finite element analysis, the results were in good agreement with the experimental load-deflection curves.

The authors concluded that the equations presented for the design of stiffeners for thin steel shear walls are satisfactory provided that plate buckling would not occur until the plates develop their shear yield strength.

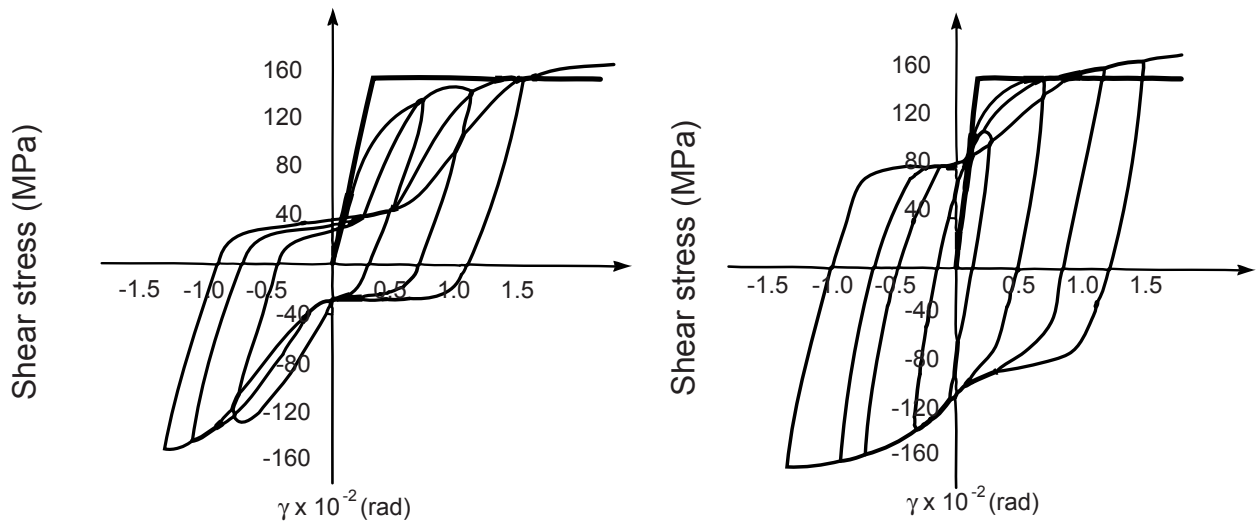


(a) Unstiffened plate (b) Heavily stiffened plate

Figure 2.1. Hysteresis behavior of SPSW (after [3])

### 2.2.2 Mimura and Akiyama (1977)

Mimura and Akiyama [10] followed the work of Takahashi *et al.* by developing general expressions for predicting the monotonic and cyclic behavior of unstiffened SPSWs. The main objective of this research was to study the behavior of a frame wherein SPSWs were installed. The shear walls were characterized by a buckling load that was considerably lower than the yield strength.

The elastic buckling theory of plates assuming simply supported boundary conditions was used to calculate the buckling load of the plate. After the elastic buckling load was achieved, they assumed that the steel panels would develop a tension field to resist the applied loads. The angle of inclination of the tension field was calculated with the derivation provided by Wagner [11], which neglected the shear capacity after the out-of-plane buckling of the plate had developed. The envelope of load-deflection curves was established by the sum of the contributions from the panel and surrounding frame.

The authors developed the hysteresis model shown in Figure 2.2. The model is characterized by a bilinear behavior while the load remained monotonic. If the load is removed at an arbitrary point

(B) in the post-yield region, the unloading path is parallel to the elastic stiffness up to the point where the elastic shear buckling capacity of the wall is achieved (D). Beyond this point is the transition phase between shear and tension-field action. The authors adopted a residual deformation with zero stiffness equivalent to one half of the permanent plastic deformation during the previous loading cycle (DE = 0.5 x AB). As the tension field develops the load-deformation curve follows a linear path to a point of equal load and deformation as the elastic yield displacement, but in the negative direction (A'). Loading after this point follows with the same post-yield stiffness as developed in the positive direction. Unloading at an arbitrary point in the negative direction (B') follows the initial elastic stiffness until the shear buckling capacity is reached (D'). The length transition zone (D'E') is calculated as the average of the residual deformations experienced in the positive (OC) and negative directions (OC') minus one half the permanent plastic deformation developed in the negative direction (DE/2). When the tension field develops, the loading follows a linear path to the point of the last maximum load (B). Further hysteretic curves would follow in a similar manner.

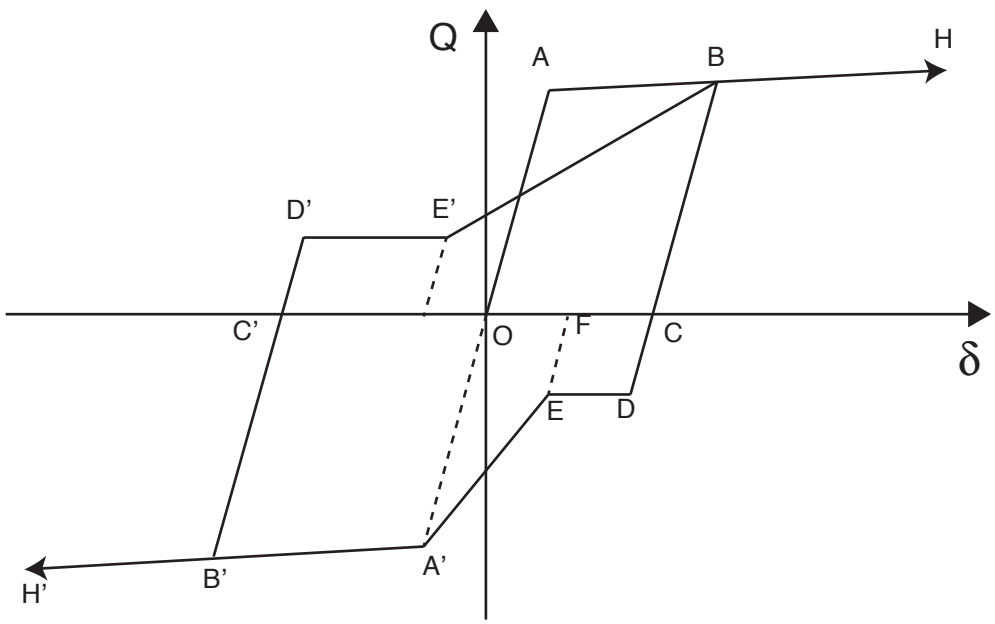


Figure 2.2. Hysteretic model proposed by Mimura and Akiyama

### 2.2.3 Thorburn et al. (1983)

The first research on unstiffened thin SPSWs in North America was conducted by Thorburn et al. [1] who developed an analytical method to study their shear resistance. As in the model developed by Mimura and Akiyama, Thorburn et al. based their model in the theory of pure diagonal tension by Wagner (1931). The model represented the shear panels as a series of inclined strip members (Figure 2.3), with pins at the ends, and oriented in the same direction as the principal tensile stresses in the panel. Each strip was assigned for an area equal to the strip width multiplied by the plate thickness. The angle of inclination was calculated based on the principle of the least work. The expressions for the inclination of the tensile stresses were obtained for two cases: (1) infinitely stiff columns (Eq. (2.1)) and, (2) completely flexible columns (Eq. (2.2)). The researchers

concluded, based on analytical studies, that 10 strips would be sufficient to represent a SPSW.

$$\tan^4 \alpha = \frac{1 + \dfrac{Lw}{2A_c}}{1 + \dfrac{hw}{A_b}} \quad \text{for infinitely stiff columns} \tag{2.1}$$

$$\tan 2\alpha = \frac{L}{h} \quad \text{for completely flexible columns} \tag{2.2}$$

where,

$\alpha$ = Angle between columns and tension strips

$w$ = Thickness of infill plate

$L$ = Width of panel

$h$ = Height of panel

$A_c$ = Cross-sectional area of column

$A_b$ = Cross-sectional area of beam

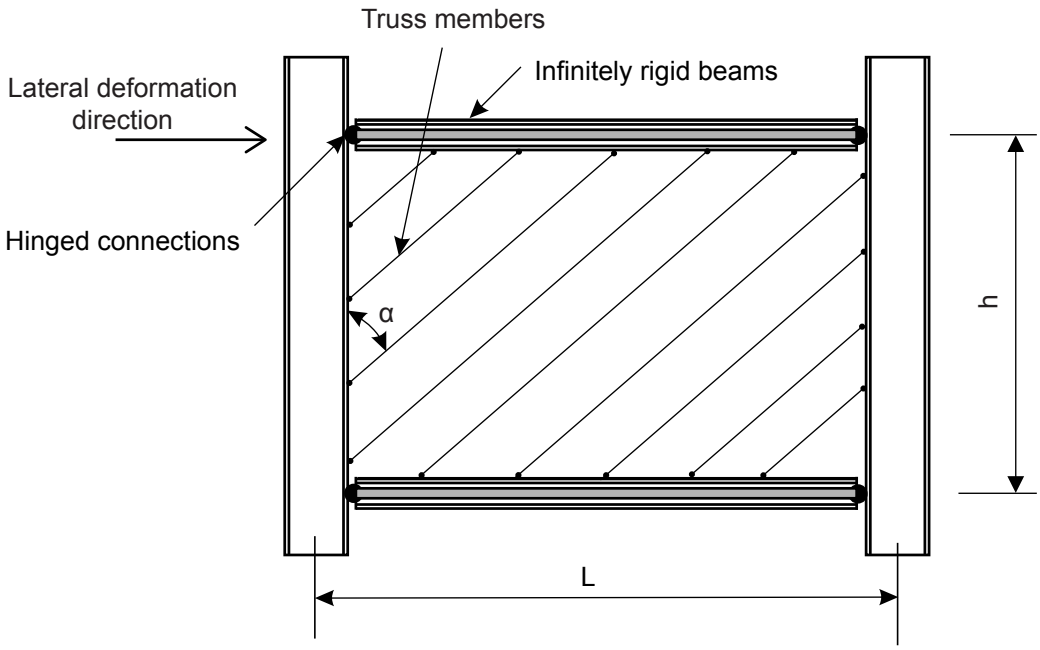


Figure 2.3. Strip model by Thorburn *et al.*

### 2.2.4 Timler and Kulak (1983)

Timler and Kulak [4] performed a test on single-story SPSW specimen to investigate the adequacy of the strip model proposed by Thorburn *et al.* in 1983. The specimen was subjected to cyclic loading to the serviceability limit, and later a pushover to failure. The test specimen consisted of two panels, with dimensions of 3750 mm in width and 2500 mm in height. The thickness of the steel plate was 5 mm.). At the service load stage, the angle of the principal stresses varied between 44° and 56° along the centerline of the plate. At the yield load, the overall magnitude and

distribution of the principal stresses were uniform and in good agreement with analytical results. The specimen ultimately failed by tearing of the weldings between the steel plate and the fish plates.

Timler and Kulak revised the equations proposed by Thorburn et al. (Eq. (2.1) and Eq. (2.2)) to include the bending stiffness of the columns in the calculation of the angle of the tension field (Eq. (2.3)).

$$\tan^4 \alpha = \frac{1 + \dfrac{Lw}{2A_c}}{1 + \dfrac{hw}{A_b} + \dfrac{h^4 w}{360 I_c L}} \tag{2.3}$$

where,

$I_c$ = Column moment of inertia

### 2.2.5 Elgaaly, Caccese, Chen and Du (1993)

Elgaaly *et al.* [5] conducted a series of tests where five quarter scale three story SPSW specimens with different plate thicknesses and beam-to-column connections were tested under cyclic and monotonic loading. No axial load was applied to the columns. The thicknesses of steel plates were 0.076 mm, 1.90 mm and 2.66 mm. Three specimens were built with moment resisting beam-to-column connections. The other two specimens were constructed with shear beam-to-column connections.

The moment-resisting frame was tested as the baseline for the SPSW tests. The cyclic behavior was characterized by an stable hysteretic behavior as shown in Figure 2.4 (a). The response of the frame was essentially linear-elastic up to 0.5% drift levels. The cyclic behavior of the SPSW specimens exhibited significant pinching (Figure 2.4 (b) through (f)). The predominant contribution to the nonlinear behavior was attributed to the initial tension-field and yielding of the plate, which started at a displacement of about 7.6 mm (0.3 in.). This yielding caused a permanent stretching and subsequent bulging of the plate and a pinching of the hysteresis loops was the result.

The type of beam-to-column connections selected was found to have a minor effect on the overall load-displacement curve of the specimens. The authors reasoned that the continuous welding of the plates to surrounding beams and columns would induce the connections to act as moment resisting even without welding the flanges of the beams to the columns.

The analytical model proposed by Thorburn *et al.* was used to predict the load-deformation curves of the shear wall specimens. The authors found that the model was unable to replicate the experimental results when an elastic-perfectly plastic stress-strain relationship curve for the plate material was assumed. To overcome this difficulty a trilinear relationship was developed. In this new relationship the secondary stiffness was selected in such a way to obtain a good agreement between the analytical and experimental results.

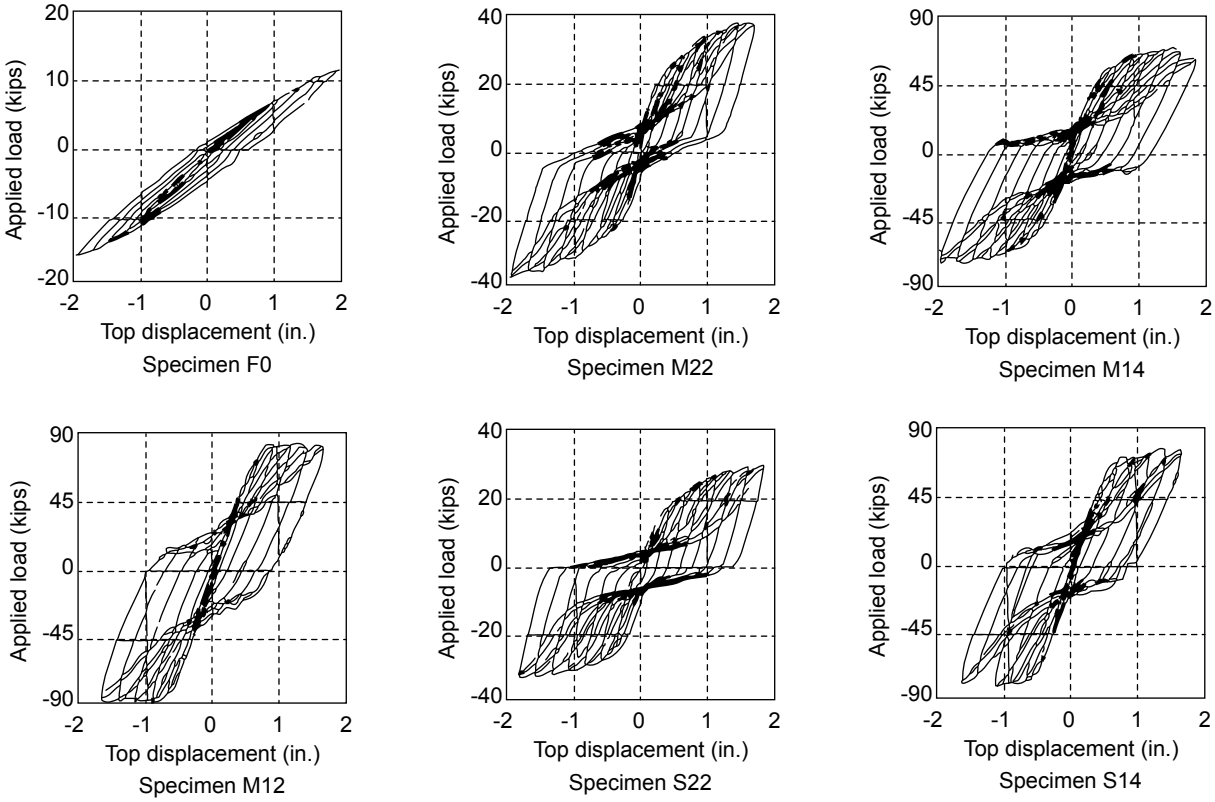


Figure 2.4. Hysteretic results by Elgaaly *et al. (1993)*

### 2.2.6 Driver (1997; 1998)

Driver et al. [6] conducted quasi-static cyclic testing on a large-scale, four-story, single bay specimen equipped with SPSWs. In the test specimen, steel plate thicknesses were 4.8 mm for the first and second story walls, and 3.4 mm for the third and fourth story walls. The prototype structure was 7.5 m high and 3.4 m wide with a story height of approximately 1.9 m. The test considered gravity loads applied at the tops of the columns. The lateral load was applied at each floor level. The specimen was found to have large initial stiffness and energy dissipation capacity. However, after the ultimate strength was achieved, the load-carrying capacity gradually deteriorated. The maximum drift angle achieved by the first story before the specimen failed was nine times the yield drift angle, evidence of a the high ductilities that were achieved during these test.

Driver *et al.* developed a finite element model to study their test specimen. Beams and columns were modeled with beam elements and the steel plates were modeled with shell elements. An initial imperfection based on the first buckling mode of the steel plate was included in the finite element model. Both monotonic and cyclic analyses were performed, but due to convergence problems, geometric nonlinearity was not included throughout the analysis. The pushover analysis provided prediction very good estimation of the ultimate strength, but it overestimated the initial stiffness. The cyclic analysis replicated the load vs. displacement curves with good agreement to the test data, however they failed replicate the pinching of the hysteresis loops observed in the test results.

### 2.2.7 Berman and Bruneau (2003; 2005)

Using the concept of plastic analysis and the strip model, Berman and Bruneau [12], [13]

derived equations to calculate the ultimate strength of single and multi-story SPSWs with simple or rigid beam-to-column connections. To calculate ultimate strengths of multi-story SPSWs, two types of failure mechanism, were assumed: (1) soft story mechanism, and (2) yielding of all infill plates and plastic hinging at the ends of all beams (except for the top and bottom storey where plastic hinging is also allowed at the columns) formed simultaneously.

The authors later conducted quasi-static testing of three specimens using light gauge cold-formed steel for the infill plate material (since the minimum infill plate thickness available is often greater than that required to resist design lateral forces). One specimen consisted of corrugated steel plates and the remaining two consisted of flat infill plates. The connection of the infill plates to the boundary elements in the first two specimens was achieved through bolts in combination with industrial strength epoxy; the second specimen (flat infill plate) was welded. The bay width and story height of the specimens were designed to be 3660 mm and 1830 mm, respectively (i.e., approximately 0.5 scale from the prototypes).

The corrugated specimen reached a ductility of 3 prior to losing substantial strength. The tension field action developed only in the direction parallel to the corrugations, resulting in unsymmetrical hysteresis loops (Figure 2.5 (a)) . The additional strength that was provided by the corrugations was not observed after buckling occurred. The epoxy connection of the infill plate to the boundary frame of the specimen cracked in some locations; however, the cracking did not prevent the full yielding of the plate.

The specimen utilizing a welded connection to the boundary frame reached a ductility ratio of 12 and a maximum drift angle of 3.7% and showed a reasonable agreement in initial stiffness and base shear strength with the monotonic pushover of a strip model (Figure 2.5 (b)). Also, the welded specimen was significantly more ductile than the bolted specimen and failure was the result of fractures in the infill adjacent to the fillet weld.

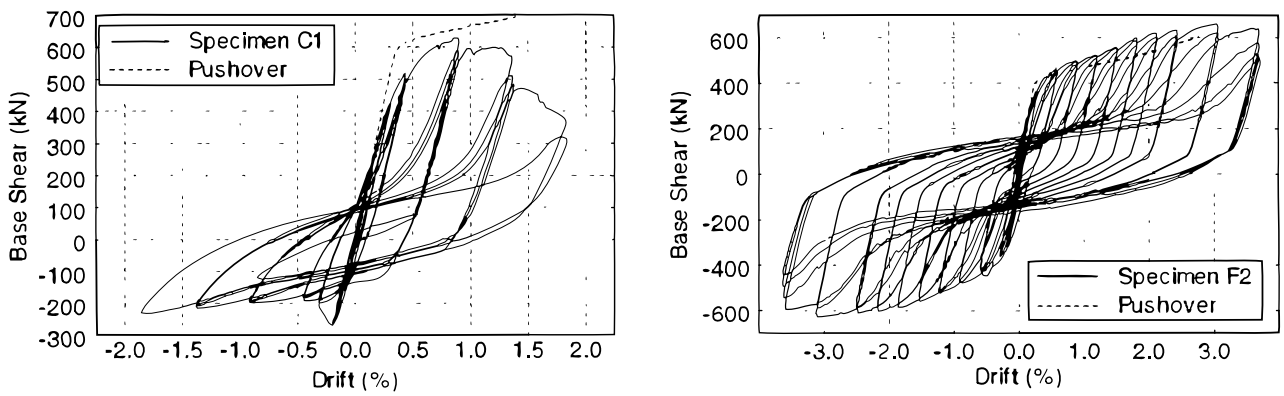


(a) Corrugated specimen with bolted and epoxy connection

(b) Flat specimen with welded connections

Figure 2.5. Multi-storey SPSW specimen hysteresis and pushover curve (Berman and Bruneau 2003)

## 2.3 Shear Walls with perforations

The research on shear walls with openings has gained attention from researchers. Since very often the shear walls used are stronger than the design requirements, which introduce excessive forces to the surrounding frame members. Perforations in the steel plates can significantly reduce the design forces on boundary elements by weakening the shear walls. Several alternatives have been considered to reduce the strength of the infill plates. Some of the alternatives that have been considered include the use of low yield steel (LYS) instead of conventional steel for the steel plates [13]-[16]. Another alternative that has been studied considers the introduction of circular openings in the steel plate [7], [16]-[18]. The last alternative considered is the introduction of vertical slits [19], [20].

### 2.3.1 Omori et al. (1966)

Omori et al. [19] motivated by the possibility of brittle failure of reinforced concrete (RC hereafter) walls in lower stories, conducted a series of tests on reinforced concrete walls to investigate the effect of introducing slits (Figure 2.6 (a)) with the aim of preventing brittle failure and providing a persistent resistance after yielding (ductility). Eight tests were conducted where the parameters studied were the slit location, the slit height and the numbers of slits introduced in the walls. One of the specimens was designed without slits and was used as a control for the results of the other specimens.

The specimens were laid horizontally in a hinged frame (Figure 2.6 (b)) and were loaded diagonally to provide pure shear forces. Four specimens were loaded monotonically and the other four were loaded cyclically. The authors found that the specimens with slits show both bending and shear deformations, as opposed to pure shear in the base-line specimen. They concluded that by the introduction of slits the RC walls can provide a relatively small initial stiffness and a more ductile behavior can be achieved.

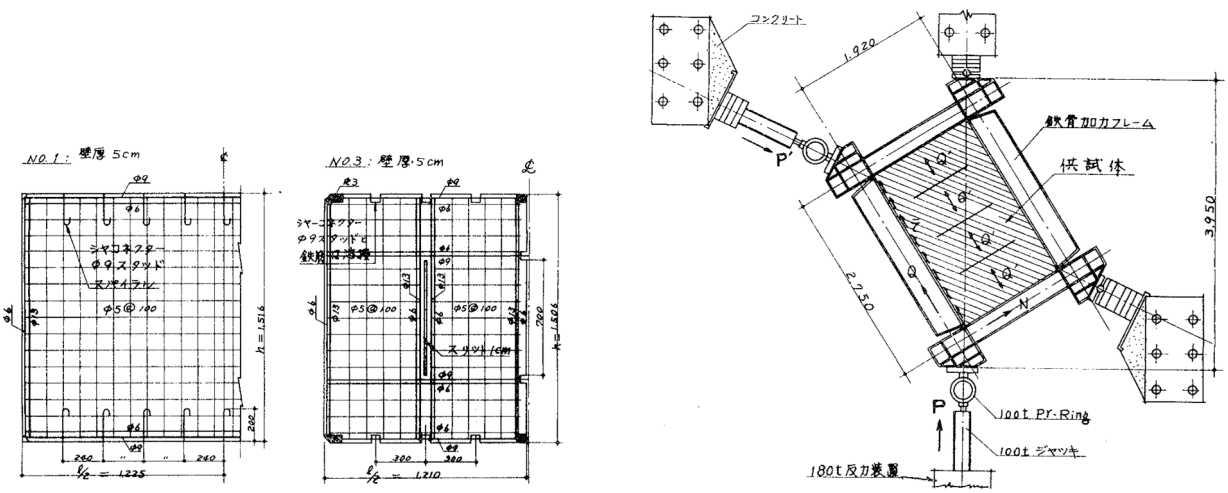


(a) Specimens (b) Load setup

Figure 2.6. Tests by Omori et al (1966)

### 2.3.2 Mutoh et al. (1968)

Mutoh et al. [21] followed on the concerns expressed by Omori et al. regarding the brittle failure of RC shear walls attempted to demonstrate the elastic characteristics of slitted RC walls. One of the specimens was later used in the construction of one building in downtown Tokyo.

The authors conducted a series of elastic finite element analyses on the specimen shown in Figure 2.7 (a). For the analyses, the wall was considered as a perfectly elastic body with infinitely rigid boundary conditions, the width of the slit was considered to be zero. The average shear force of the wall was calculated from the reaction forces at the top and bottom boundaries.

The authors conjectured that slitted RC walls subjected to lateral force could be assumed as two symmetrical cantilever beams fixed along the ends of the wall where the unslitted section along the height of the wall could be considered as rigid (Figure 2.7 (b)). The cantilever beam is subjected to concentrated force along the centerline of the wall. The resultant stresses obtained based on this conjecture were compared to the results of the finite element analysis (Figure 2.7 (c)) and were found to agree on most locations with the exemption of the stresses nearest to the slit ends were the stresses from the finite element model were much larger. The authors concluded that the slit ends present a high concentration of stresses that cause the behavior of slitted walls to differ from that of a cantilever beam. Nonetheless if the rigid zone is considered to extend to the slit end, the error in the calculation of the wall stiffness incurred by this assumption is less than 2%.

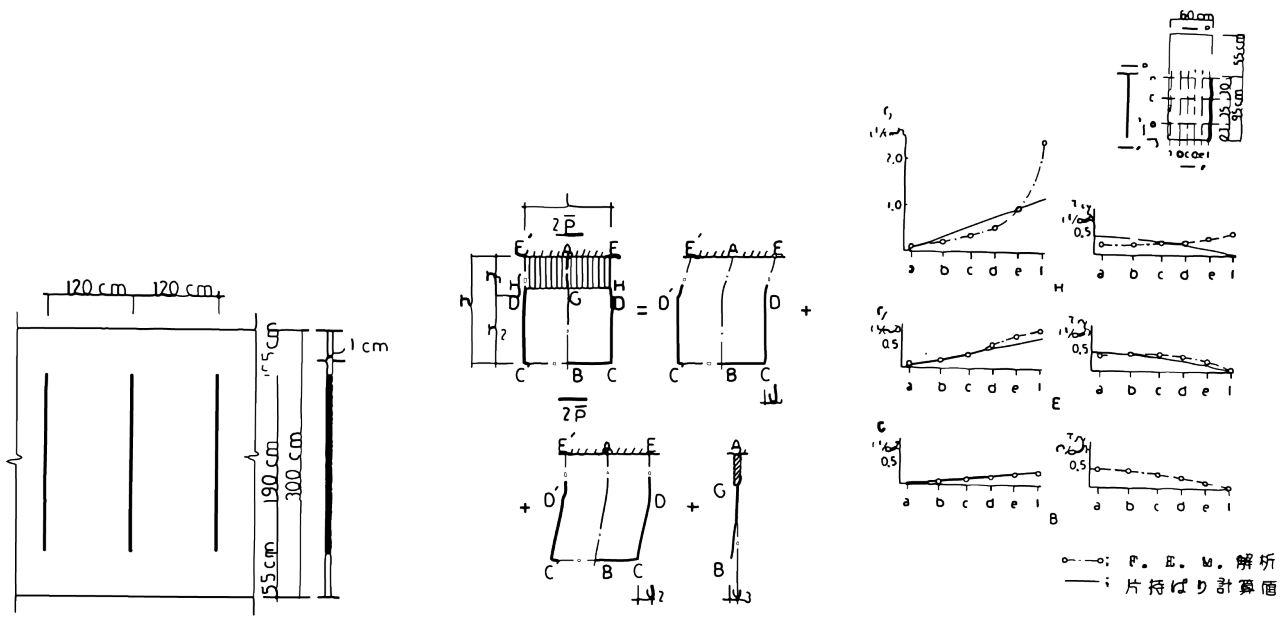


(a) Model (b) Simplified model (c) Strain comparison

Figure 2.7. Finite element analysis by Mutoh et al. (1968)

### 2.3.3 Roberts and Sabouri-Ghomi (1992)

Roberts and Sabouri-Ghomi [7] conducted a series of tests on small-scale unstiffened steel plate shear panels with a single circular opening at the center. The specimens had a constant depth of 300 mm and widths of either 300 mm or 450 mm. Four diameters of the circular opening were considered: 0, 60, 105, and 150 mm. The specimens were subjected to quasi-static cyclic loading.

Based on the results, the authors recommended that the strength and stiffness of the perforated panel could be approximated by a applying a linear reduction (based on the ratio between the diameter of the perforation and the height of the plate) to the strength and stiffness of a solid panel.

### 2.3.4 Hitaka and Matsui (2003)

Hitaka and Matsui [20] proposed a modified SPSW in which vertical slits are introduced to the infill plate, the authors called this device "Slit Walls" (Figure 2.8). In this system, the steel plate segments between the slits behave as a series of flexural links, which undergo large flexural deformations relative to their shear deformation (see the insert in Figure 2.8), providing a ductile response without significant out-of-plane stiffening of the wall. The authors proposed a design procedure based on separating the behavior of the wall between the shear deformation of whole plate and deformations of flexural links. To validate the design procedures a series of tests were conducted on 42 reduced-scale Slit Wall specimens and conducted non-linear FEM analyses. Pilot tests revealed that the slenderness ratio of the flexural link (width divided by plate thickness) was predominant in the determination of the behavior of the wall. The test focused on the behavior of the shear walls with varied slit patterns in terms of the slit design parameters slenderness ratio and aspect ratio of the flexural links. Another series studied the transverse behavior of the Slit Walls, where three types of transverse stiffening techniques were considered: no stiffening, steel stiffeners, and mortar panel stiffening. The final series of tests examined the shear wall behavior under different loading protocols.

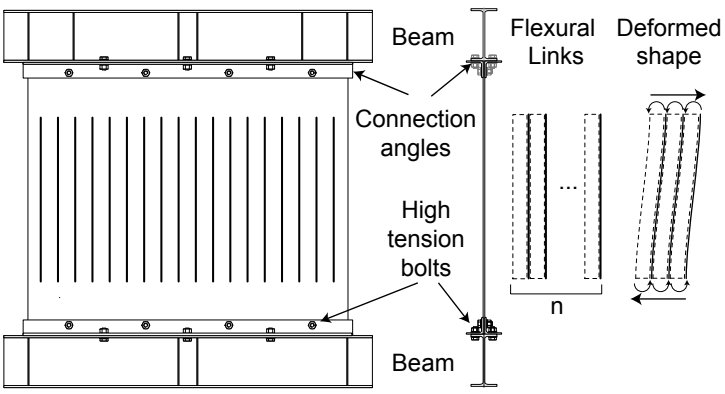


Figure 2.8. Slitted Steel Shear Wall (Hitaka and Matsui (2003))

All specimens were constructed with steel plates with dimensions of 800 x 800 x 4.5 mm, which is approximately one-third of the full scale applications. Slits were cut using a laser, initiating the cut at midheight and rounding each end in a circular arc, so as to minimize stress concentrations. stiffeners. The specimens considered edge stiffeners (50 mm wide and 4.5 mm thick) connected to the plate along its vertical edges by fillet welds. The stiffener width of 50 mm was determined to avoid yielding due to overturning moment.

With a few exceptions, all specimens underwent story drift angle of more than 3% without initiation of cracks or abrupt strength degradation under monotonic or incremental cyclic loading.

The response was elastic until yielding at one-third of the maximum strength. Strength degradation was observed after the initiation of out-of-plane deformations, which occurred in all specimens after achieving story drift angles of about 5%. The test results showed that the transverse buckling of the plate is the main cause of strength degradation, and that the ductile fractures that were observed later in the loading were of lesser concern.

Shear plates in all specimens with slenderness ratios of 10 remained in-plane up until drift angles of more than 2.5%, whereas in most other specimens, transverse deformation took place when the drift angle was less than 2%.. The authors noted, however, that the strain in the plate exceeded yield before the horizontal force reached the calculated yield strength. Results from finite element models indicated that there were stress concentrations at the edge of the slits, which triggered yielding of the steel plate at a story drift smaller than previously expected.

### 2.3.5 Vian (2005)

Vian [16] conducted quasi-static cyclic tests on three single-story SPSW specimens. The first specimen had rigid beam-to-column connection with reduced beam sections (RBS) on the beams, and a solid plate of low yield steel. The remaining specimens had the same surrounding frame as the first specimen, and either multiple regularly spaced circular perforations in the plate or reinforced quarter-circle cut-outs in the upper corners of the plate. The two specimens, are shown in Figure 2.9 (a) and (b), respectively.

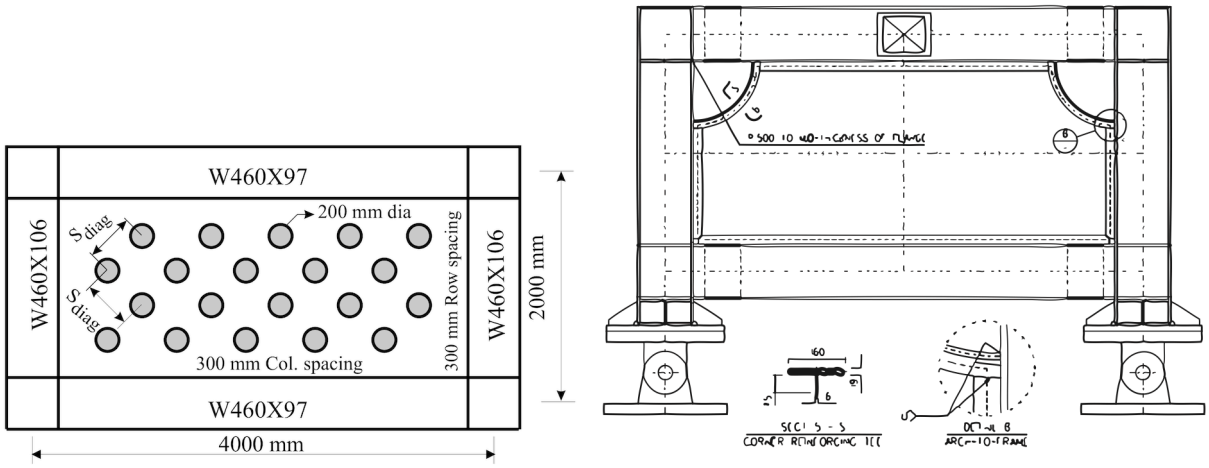


(a) Perforated specimen (b) Cut-out specimen

Figure 2.9. Specimens by Vian (2005)

The SPSW specimens had a width of 4000 mm, and a height of 2000 mm. The plate used had a thickness of 2.6 mm. The perforated specimen had staggered holes, with a diameter of 200 mm, arranged at a 45° angle, and spaced at 300 mm. The cut-out corner specimen had 500 mm radius quarter-circle cut-outs at the upper corners. The cut-out edges were reinforced with arch sections 160 mm wide by 19 mm thick. The specimens were tested under quasi-static cyclic load. The perforated specimens were tested to a maximum drift of 3%, while the SPSW specimen was tested to a maximum drift of 4%.

The results of the cyclic test for the perforated specimen and the cut-out specimen are presented in Figure 2.10 (a) and (b), respectively. The perforated specimen began with three cycles each at

drift amplitudes of 0.1 and 0.2%. Elastic buckling of the panel and linear force-displacement behavior was observed for these cycles. Panel yielding was first observed after the amplitude reached 0.3% drift angle when the whitewash flaked between perforations at two locations on the panel. As the loading amplitudes increased, yielding progressed throughout the panel and the RBS connections. At a drift amplitude of 2.5% a slight decrease in base shear was observed. Testing was concluded after an audible bang was heard and a drop occurred in the strength of the specimen during the second positive displacement excursion to 3% drift angle. Subsequent inspection revealed a fracture of the continuity plate on the far column at the wall flange. Flange local buckling was observed in the bottom flange of the far bottom beam RBS connection. By the end of the loading, the steel plate wall had not yet fractured.

The cut-out specimen behaved elastically for drift angles of 0.1%, with no visible signs of yielding. At 0.2% drifts, flaking of the whitewash indicated the initiation of yielding in the flanges of the RBS connection. A large reduction of the maximum strength was observed on the second cycle to 3% drift angle, when the flange of the RBS beam fractured at two points. After this the loading continued up to 4% drift angles, where reductions of the maximum strength equivalent to 24 and 25% were observed in the positive and negative directions, respectively.

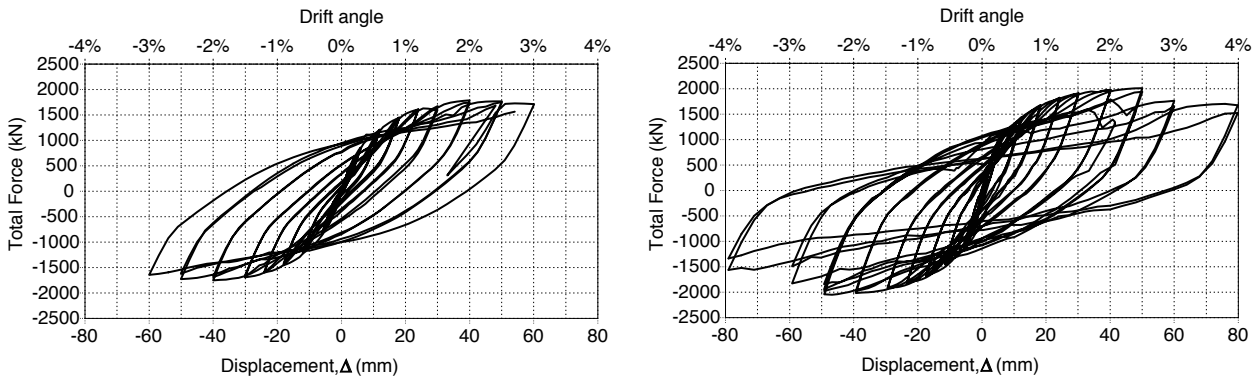


(a) Perforated specimen (b) Cut-out specimen

Figure 2.10. Hysteretic results (After Vian (2005))

### 2.3.6 Purba (2006)

Purba [17] conducted a series of finite element analyses to investigate the behavior of unstiffened thin SPSWs with openings in the plate. The two designs, namely the perforated infill plate and the cut-out corner SPSW proposed by Vian (2005), were investigated. Similar to Vian (2005), individual perforated strips (see Figure 2.11) were first analyzed to develop a fundamental understanding of the behavior of complete perforated SPSW.

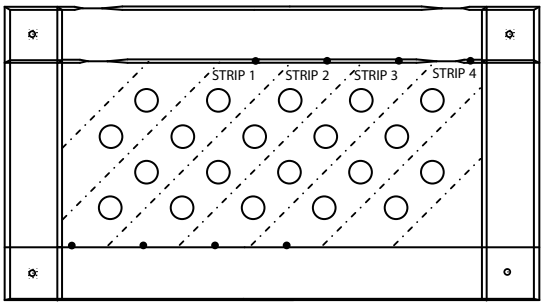


Figure 2.11. Definition of strip

With the behavior of individual perforated strips known, a series of 4000 mm by 2000 mm single-story perforated SPSWs having multiple perforations were modeled. Shell elements were used to model both the infill plates and the boundary frame members. Nonlinear pushover analyses were conducted for the single-story perforated SPSWs. Variations in perforation diameter and infill plate thickness were considered in the analyses. The author found that the results from the individual perforated strip analysis could accurately predict the behavior of complete perforated SPSW provided the holes diameter is less than 60% of the strip width $\left(D/\mathrm{S}_{\mathrm{diag}} \leq 0.6\right)$. It was found that no interaction exists between adjacent strips that could affect the stress distribution within an individual strip.

Purba (2006) also examined the applicability of using the reduction method proposed by Roberts and Sabouri-Ghomi (1992) to approximate the strength of a perforated infill plate with multiple perforations. Based on analysis results, the author concluded that shear strength of an infill plate of a SPSW with multiple regularly spaced circular perforations could be calculated by multiplying the shear strength of a solid infill plate by a factor of $\left(1\text{-}0.7\mathrm{D}/\mathrm{S}_{\mathrm{diag}}\right)$.

### 2.3.7 Bhowmick et al (2009)

Bhowmick [18] performed a series of finite element analyses of unstiffened SPSWs with different perforation patterns, shown in Figure 2.12. The analyses showed that the shear strength of an infill plate with circular perforations could be calculated by reducing the shear strength of the solid infill plate by the factor given by Eq. (2.4).

$$\frac{V_{op}}{V_p} = \left(1 - \beta N_r \frac{D}{L_p \cos\alpha}\right) \tag{2.4}$$

where,

β = reduction factor to discount the effect of the perforation in the diagonal strip.

$N_r$ = maximum number of diagonal strips (at any section, cut parallel to length $L_p$, over the height of the panel) with circular perforations to be discounted.

$L_p$ = the width of perforated infill plate

D = diameter of the perforation

α = angle of inclination of the diagonal strips, usually 45°

From the analyses the author concluded that a value of 0.7 for beta gave the most accurate predictions. The proposed equation was found to give good predictions of the reduced shear strengths of SPSWs with different patterns of perforations, different perforation diameters, and different infill plate aspect ratios.

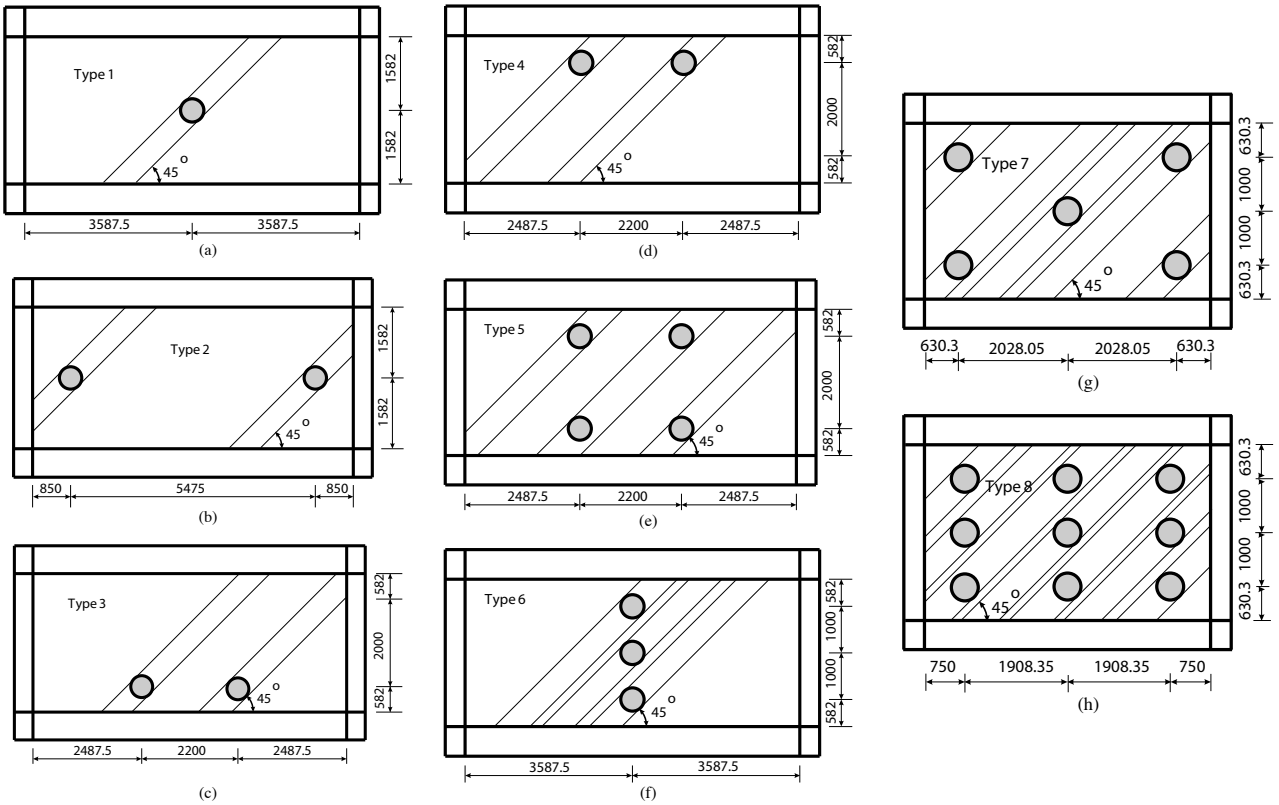


Figure 2.12. Models after Bhomwick

## 2.4 Summary and Conclusions

Experimental and analytical research on thin unstiffened SPSWs has shown that the SPSW system possesses high initial stiffness, ultimate strength, and ductility, as well as stable hysteresis curves and a large energy dissipation capacity. It has been recently demonstrated that the use of perforations or the cutting of slits in the plates reduces the strength and stiffness of the walls, and thus the demand for the boundary framing members.

Two different approaches have been considered to estimate the strength and stiffness of SPSWs: one approach approximates the behavior of the tension field in the steel plate with strips that work in tension and model the inelastic behavior in the material properties. This approach has been used to design unstiffened SPSWs, either with or without perforations. In the second approach, intended for the design of steel plates with slits, the slits prevent the formation of the tension field, and allow the links formed between the slits to behave as beam-columns in bending.

Unfortunately, the research conducted on SPSWs has not yet addressed several issues. The first such issue relates to the need of SPSWs to be attached to the boundary frame to develop the tension field. The tension field generates large forces in the boundary members and special provisions have to be taken in the design to avoid damage from taking place in these members. Also, as the SPSW

has to occupy the full beam span, no space is left for window or door openings, reducing the possible locations where SPSWs can be installed. Recently some studies have considered the inclusion of openings for utilities but these applications still require the SPSW to be attached to the frame members. A second issue refers to the extension of the research on SPSWs. The research has been focused on element tests, whether simple SPSW specimen or frame assemblies, and FEM analyses. There is yet no record of research of the application of these walls in actual frame buildings subjected to seismic demands.

# REFERENCES


[1] Thorburn, L.J., Kulak, G.L., and Montgomery, C.J., 1983, "Analysis of Steel Plate Shear Walls", Structural Engineering Report No. 107, Department of Civil Engineering, University of Alberta, Edmonton, A B .

[2] AISC. 2005. Seismic provisions for structural steel buildings. American Institute of Steel Construction, Chicago, IL.

[3] Takahashi, Y , Takemoto, Y , Takeda, T. and Takagi, M., 1973, "Experimental Study on Thin Steel Shear Walls and Particular Bracings Under Alternative Horizontal Load", Preliminary Report, IABSE Symposium on Resistance and Ultimate Deformability of Structures Acted on by Well-defined Repeated Loads, Lisbon, Portugal, pp. 185-191.

[4] Timler, PA. and Kulak, G.L., 1983, "Experimental Study of Steel Plate Shear Walls", Structural Engineering Report No. 114, Department of Civil Engineering, University of Alberta, Edmonton, A B .

[5] Elgaaly, M., Caccese, V. and Du, C , 1993, "Postbuckling Behaviour of Steel-Plate Shear Walls under Cyclic Loads", Journal of Structural Engineering, ASCE, Vol. 119, No. 2, pp. 588-605, February.

[6] Driver, R.G., 1997, "Seismic Behaviour of Steel Plate Shear Walls", Ph.D. Dissertation, Department of Civil and Environmental Engineering, University of Alberta, Edmonton, AB.

[7] Roberts, T.M. and Sabouri-Ghomi, S., 1991a "Hysteretic Characteristics of Unstiffened Plate Shear Panels", Thin-Walled Structures, Vol. 12, No. 2, pp. 145-162.

[8] Sabouri-Ghomi, S. and Roberts, T.M, 1991b, "Nonlinear Dynamic Analysis of Steel Plate Shear Walls", Computers & Structures, Vol. 39, No. 1/2, pp. 121-127.

[9] Sabouri-Ghomi, S. and Roberts, T . M , 1992, "Nonlinear Dynamic Analysis of Steel Plate Shear Walls Including Shear and Bending Deformations", Engineering Structures, Vol. 14, No. 5, pp. 309-317.

[10] Mimura, H. and Akiyama, FL, 1977, "Load-Deflection Relationship of Earthquake- Resistant Steel Shear Walls with a Developed Diagonal Tension Field", Transactions of the Architectural Institute of Japan, 260, October, pp. 109-114 (in Japanese).

[11] Wagner, H. (1931). Flat Sheet Metal Girders with Very Thin Webs, Part I - General Theories and Assumptions. Technical memo No. 604, National Advisory Committee for Aeronautics, Washington, D C .

[12] Berman, J. W. and Bruneau, M. 2003. Plastic analysis and design of steel plate shear walls. Journal of Structural Engineering, ASCE, 129(11): 1148-1156.

[13] Berman, J. W. and Bruneau, M., 2005. Experimental investigation of light-gauge steel plate shear walls. Journal of Structural Engineering, ASCE, 131( 2): 259- 267.

[14] Nakashima, M., Iwai, S., Iwata, M., Takeuchi, T., Konomi, S., Akazawa, T. and Saburi, K. (1994). Energy dissipation behavior of shear panels made of low-yield stress steel, Earthquake Engineering and Structural Dynamics, 23(12), 1299–1313.

[15] Nakashima, M. (1995). "Strain-hardening behavior of shear panel made of low-yield steel. I: Test." *J. Struct. Eng.*, 121(12), 1742–1749.

[16] Vian, D. 2005. Steel plate shear walls for seismic design and retrofit of building structures. PhD dissertation, State Univ. of New York at Buffalo, Buffalo, N.Y.

[17] Purba, R., and Bruneau, M. (2007). "Design recommendations for perforated steel plate shear walls." *Technical Rep. No. MCEER-07-0011*, Multidisciplinary Center for Earthquake Engineering Research, State Univ. of New York at Buffalo, Buffalo, N.Y.

[18] Bhowmick, A., Driver, R., Grondin, G., (2009). "Seismic analysis of steel plate shear walls considering strain rate and P–delta effects"., *Journal of Constructional Steel Research*, 65(5), pp. 1149-1159

[19] Omori, S., Toyama, K., Cho, T., and Takahashi, T. (1966). ''Test on RC shear wall with slits.'' *Summaries of Technical Papers of Annual Meeting AIJ*, Kanto, Japan, 204–205 (in Japanese).

[20] T. Hitaka and C. Matsui, "Experimental study on steel shear wall with slits," *J. Struct. Eng.-ASCE*, vol. 129, 2003, pp. 586 - 595.

[21] Mutoh, K., Miyashita, O., Osada, M., and Kanayama, H. (1968). ''Stress and deformation of slit wall, using FEM.'' *Summaries of Technical Papers of Annual Meeting AIJ*, Chugoku, Japan, 543–544 (in Japanese).

# CHAPTER 3

# Slit Walls with Unequal Slitting

## 3.1 Introduction

### 3.1.1 Overview

In this chapter the development of a new kind of damper device, known as slit walls (SW hereafter) is presented. Slit walls are special kind of steel shear walls in which slits are cut on the plate with the aim of reducing the strength and stiffness of the wall [1], [2]. The number and length of the slits control the stiffness of the wall. Modifications to the distribution of the slits in the steel plate are introduced to add condition assessment capabilities.

### 3.1.2 Addition of condition assessment capabilities to slit walls

Structural condition assessment [3] focuses on techniques for evaluating the integrity of a structure after an earthquake event to ascertain the danger that it represents for re-occupation of the building. This evaluation can be performed through health-monitoring (for example [4], [5]), or through performance-evaluation analyses that rely on detailed computer models of the structure. Unfortunately, the required technologies remains untested against actual large earthquakes, and the cost of implementing it restricts its use to important structures, such as large spatial structures, bridges, dams and high-rise buildings. The small number of sensors used in these structures is only sufficient to identify the existence of damage by observing global changes in the vibration modes and frequencies. These restrictions encourage the development of a method of estimating the damage sustained by a structure that is more straightforward and easier to implement.

Adding condition assessment capabilities to SWs has the benefit of extending their application to monitoring purposes, whilst retaining their original function as damper devices [6], [7]. In this chapter, a modified slit design for SW is proposed to include condition assessment capabilities. Unlike the conventional SWs in which the distance between slits is constant, the proposed SW features slitting with unequal distances. This enables strain patterns that vary significantly over the plate and an eventual gradual spread of yielding with the increase of interstory drift. This gradual spread is the key for the condition assessment, in which the correlation between the yield region and the maximum interstory drift is employed. For the identification of the yield region, brittle paint is considered in this study, since the flaking of brittle paint provides a permanent recording of the maximum strains experienced within the SW [8].

### 3.1.3 Organization

This chapter is divided into two sections. First, the conceptual work for achieving the introduction of condition assessment capabilities is presented. Several modified slit designs are evaluated and compared to obtain the most suitable for condition assessment purposes. Afterwards, the condition assessment performance of the walls is studied, and design equations to establish the basic properties (strength and stiffness) of the slit wall. The obtained characteristics are later used in the design stage of buildings.

In the second section of this chapter, a parametric study is conducted on individual slits to determine their individual performance, characteristics such as energy dissipation, out-of-plane buckling initiation are established. Empirical equations based on geometric characteristics are developed to predict the behavior of flexural links.

## 3.2 Unequal slitting

This study is based on the assumption that it is possible to estimate the experienced maximum interstory drift from the yield regions identified in the SWs. Several issues have to be considered when selecting a slit design for condition assessment purposes. First is the necessity of preserving the hysteretic (damping) characteristics of the slit wall. The second condition, directly related to the condition assessment capability, is to highlight certain behaviors in the SW as much as possible to differentiate between different interstory drifts. The alternative examined in this chapter relates to the spreading of the higher strains generated at the end of slits over a larger area of the steel plate. The spreading of the strains can be traced, and the patterns developed herein can be associated to corresponding drift angles. Chapter 6 will discuss a method to record the spreading of the strain patterns by means of brittle coatings. An added advantage of spreading the strains through a large area is the reduction of the strain concentrations at the slit ends. These strain concentrations can lead to fractures if the SW is subjected to heavy drift demands. Also a larger strain area increases the area where brittle coating flakes, which facilitates the identification of the interstory drifts by the flake patterns.

### 3.2.1 Finite element models of slit walls

Finite element models are used throughout the development of this thesis. This analysis method is used to determine the hysteretic characteristics, the propagation of strains through the SWs and to study the out-of-plane buckling of the flexural links. To this end, a general-purpose finite element program ABAQUS version 6.7 [9] was used to perform said analyses.

**Geometry and initial conditions**

As a general rule, the dimensions of the slit wall models correspond to those of the specimens that will be tested in the laboratory, according to the maximum size allowed by the existing facilities. In a real application, all steel plate walls tested would have had some initial plate imperfections resulting from various sources such as slightly rotated connection between the plate and the beams or due to residual strains introduced by the laser cutting. Any initial out-of-plane deformations can significantly affect the initial behavior as compared to a perfectly flat plate

(specially the yield strength). Therefore, two types of initial imperfections of the plates were considered in the finite element model. For the first type of initial imperfection, the infill plate was taken to have an initial imperfection pattern corresponding to half of a sinusoidal wave. The magnitude of initial imperfections was selected to be $0.01B$ at its maximum, where $B$ is the plate width. This type of imperfection will be used for the models in Chapter 4. For the second type of initial imperfection, a pressure load equivalent to a 0.5% of the theoretical maximum force of the shear wall was applied on the surface of the plate. This second type of imperfection was selected because in Chapter 5, the out-of-plane rotations of the flexural links will be used to estimate the maximum drift angle of the wall. The models with a sinusoidal initial imperfection did not develop out-of-plane deformations in the way that was observed in the experiment, whereas the pressure imperfection managed to replicate these results.

**Element selection and meshing**

The plates were modeled using a general-purpose four-node doubly-curved shell element with reduced integration (ABAQUS element S4R). The element S4R accounts for finite membrane strains and large rotations. This element has six degrees of freedom per node: three translations ($u_x$, $u_y$, $u_z$) and three rotations ($\theta_x$, $\theta_y$, $\theta_z$) defined in a global coordinate system.

The S4R element is based on an isoparametric formulation. This element uses one integration point on its mid-surface to form the element internal force vector. Reduced integration elements are used as they give accurate results and significantly reduce running time if the elements are not distorted locally. The element size was selected from a mesh refinement study.

A structured meshing pattern was selected for most of the wall with the exception of the vicinity of the slit ends where a free meshing pattern was used. Where the structured mesh was used, the elements were arranged in a grid pattern, with this the number of elements was minimized, and the stability of the model was improved by maintaining the square angles and small aspect ratio of the elements. In the vicinity of the slit ends, the size of the elements was reduced to capture the local strain behavior that rapidly changes in these locations.

Simplified stress versus strain responses obtained from tension coupon tests were used to identify the Young's modulus and yield strength of the steel used for the models. The von Mises yield criterion was adopted for the analyses presented in this study. The associated flow rule was used to obtain the plastic strain increment.

A displacement control solution strategy is used in this study for all analyses. The displacement at the top of the plate is used as the control parameter and the analysis is stopped when the displacement reaches a specified limit.

### 3.2.2 Alternative slit designs

As a starting point in the search for a suitable slit design that would emphasize the strain patterns a conceptual study was carried out on simplified slit wall models. The models considered for the conceptual study were built in ABAQUS where only the in-plane behavior of the walls is using for the tracing of the strain patterns. For this purpose, a conventional slit wall (Figure 3.1 on the left) was selected as a starting point for the search of a suitable modified slit pattern. This pattern defines a slit wall with a stiffness of 136 kN/mm and maximum strength of 252 kN when

using a one third scale for the model. Details about the model are summarized in Table 3.1. Figure 3.1 shows the progression of the strain distribution of the slit wall for different drift angles. In black are shown the strains that exceed the yield strain of steel (0.15%). Strain concentrations are observed at the end of the slits; these concentrations are associated to the disruption of the strain field produced by the slit ends. It is apparent that there is scarce differentiation among the strain patterns for drift angles above 1%, which reduces the possibilities of associating these patterns to drift angles. It is for this reason that a variation of the slit design might provide a strain pattern that is more suitable to condition assessment purposes by displaying strain patterns that gradually change or grow as the drift angle increases.

Table 3.1. Slit wall model details

| | | |
|---|---|---|
| Plate size | 600 x 800 mm | |
| Plate thickness | 4.5 mm | |
| Slit height | 200 mm | |
| Number of slits | 8 | |
| Slit width | 2 mm | |
| Meshing | Quad and Triangular elements | |
| Material Properties | $\sigma_y$ | 297 N/mm$^2$ |
| | $\sigma_u$ | 392 N/mm$^2$ |
| | $\varepsilon_y$ | 0.2% |
| | $\varepsilon_u$ | 12.4% |
| Boundary conditions | Bottom | Fixed |
| | Top | Body constraint |
| | | in plane rotation and displacements allowed |
| | Out of plane | Restrained |

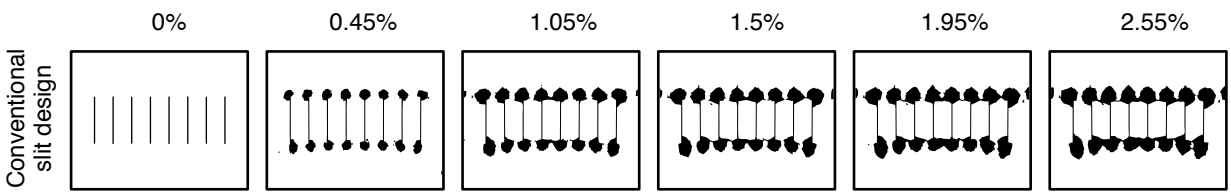


Figure 3.1. Strain distribution of a conventional slit design for different drift angles

In the search for better strain patterns, four modified slit designs were studied using ABAQUS. Models A and B are constructed with slits that have a variable length: Model A has shorter slits concentrated in the center of the wall, and Model B has longer slits in the center. Models C and D are constructed with a variable width of the flexural links: Model C considers wider links at the center, and Model D considers thinner links at the center. These four slit designs are illustrated in Figure 3.2 and their respective hysteretic characteristics, obtained from pushover analyses, are summarized in Table 3.2. As it can be observed in the table there is an increase of the initial stiffness (up to 25% for Model A) and maximum strength (18% for Model C) for most of the

models with respect to the conventional slit pattern.

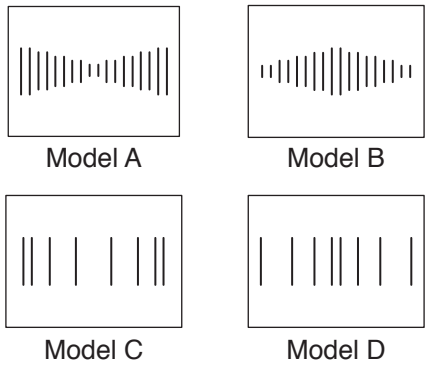

Figure 3.2. Modified Slit Walls

Table 3.2. Summary of hysteretic characteristics

| | | Model | | | | |
|---|---|---|---|---|---|---|
| | | **0** | **A** | **B** | **C** | **D** |
| Stiffness (kN/mm) | Initial | 136 | 169 | 159 | 170 | 149 |
| | Post yield | 2.7 | 3.6 | 3.4 | 2.2 | 2.1 |
| Strength (kN) | | 252 | 239.3 | 298.2 | 299.1 | 294.1 |

Several issues have to be considered when selecting a slit design that is suitable for condition assessment purposes. First is the need of retaining the hysteretic properties of the slit wall according to its the structural purpose. The results in Table 3.2 give evidence that this goal has already been achieved to an acceptable degree with the four designs proposed above. It is also important to reduce strain concentrations at the end of the slits. In the case of a large earthquake event, the zones where strains are concentrated are more prone to fracture and therefore induce strength deterioration of the structural element. It is therefore undesirable to obtain strain patterns where strains are concentrated in a reduced zone at the end of the slits. The third condition, that is directly related to the condition assessment capability of the structural element, is to provide the highest differentiation possible between the strain patterns obtained for different drift angles. Figure 3.3 shows the strain patterns (for a strain of 0.15%) developed by the four models studied under incremental cyclic loading. In the figure it is observed that Models A and B, due to their thin flexural links, show widely distributed strain concentrations at the ends of the slits but there is little difference between the strains developed after 1.0% drift angle has been achieved. On the other hand, Models C and D present larger strain patterns in the vicinity of the wider flexural links and these patterns seem to grow even after 1.5% drift angle has been achieved. It appears that Model C is more appropriate than Model D as the yield zone gradually spreads in the center of the slit wall when the drift angle increases as opposed to the edges of the plate as is the case of Model D.

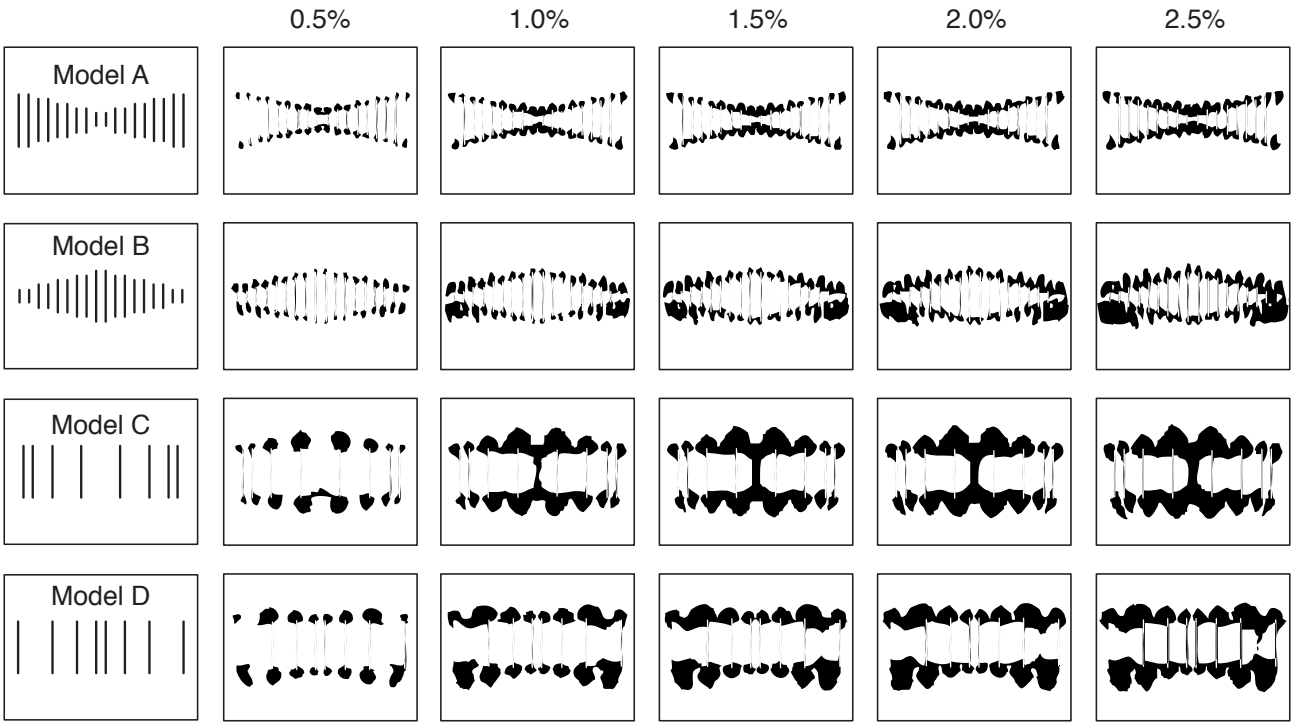

Figure 3.3. Stress pattern comparison for each slit design

### 3.2.3 Stability evaluation of unequal slitting design

As the strain patterns evaluated in the previous section are related to cyclic loading, it is desirable to evaluate the characteristics of the strain patterns developed under random input. In this manner, the effects of non-incremental loading can be evaluated to validate the assumption that strain patterns are related to the maximum drift angle experienced and are not influenced by the subsequent loading with smaller amplitudes. For this purpose five random inputs were generated with the maximum at three same drift levels as in the incremental cyclic load case. Thus, fifteen random inputs of 20 steps were generated using Matlab [10], and then used as input displacement for the model. The inputs and the corresponding strain patterns developed for this set of analyses are shown in Figure 3.4. The results indicate that the strain patterns obtained for each of these drift levels resemble each other regardless of the lateral input used. The results can be better visualized in Figure 3.5 where the strain patterns for each drift level are gathered in a single image. In this images different levels of gray denote the higher likelihood for yield strains to be reached for a given drift angle i.e., black color represents a location where yield strain was achieved for all five lateral inputs and white represents the zones where yield strain was not achieved for any lateral input. A good result is, therefore, one that shows the least amount of gray. Figure 3.5 (a) shows the resultant strain patterns obtained for 0.5% drift angle, it is clear that most of the areas are either black or white, the gray areas are concentrated in the zones at the ends of the flexural links where plastic hinges developed. Figure 3.5 (b) shows the resultant strain patterns obtained for 1.0% drift angle, in this figure, the gray areas are much smaller than those in Figure 3.5 (a) since for 1.0% drift angles the plastic hinges at the end of the flexural links have fully developed. The gray areas are almost undetectable for the loading to 1.5% drift angle.

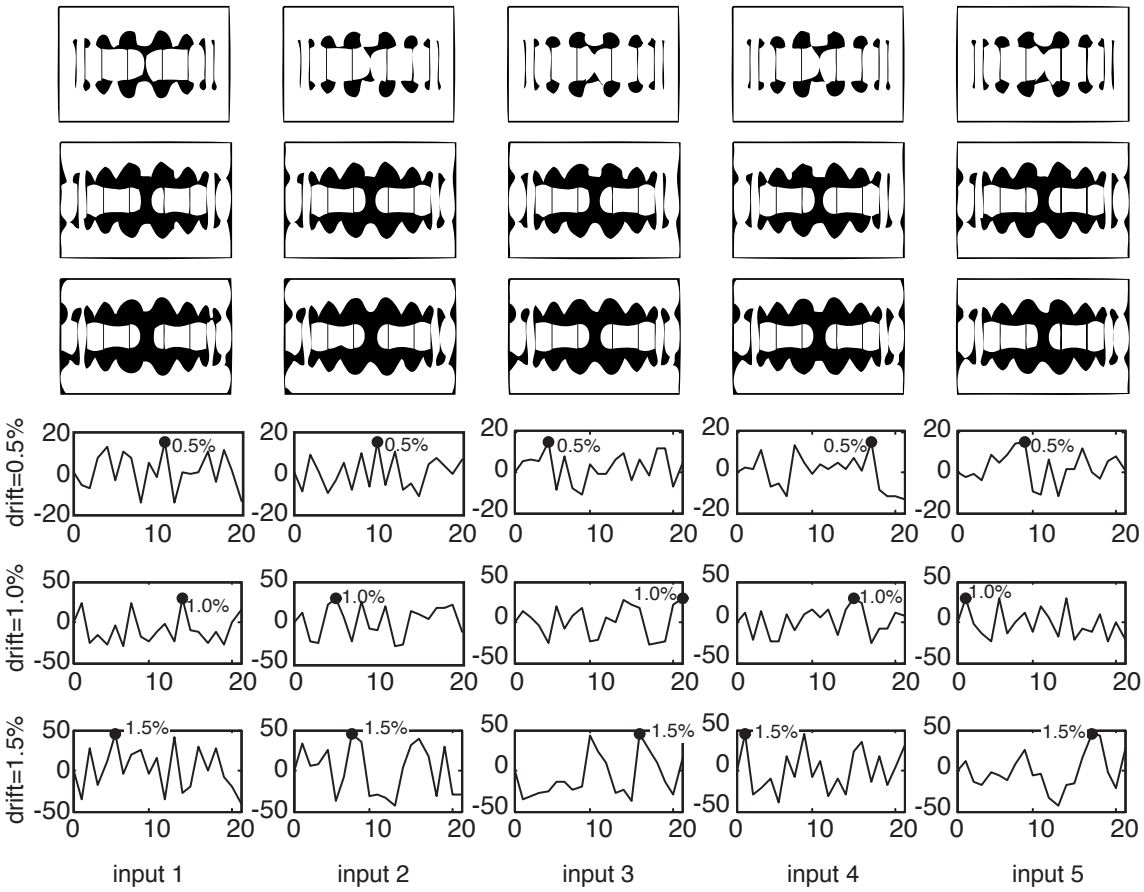

Figure 3.4. Strain patterns developed for random inputs

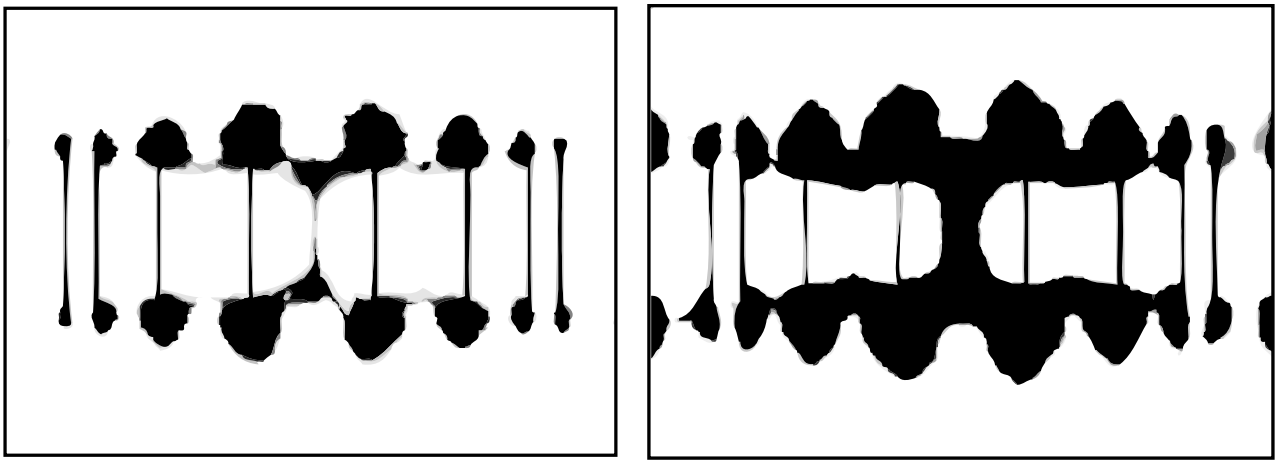

(a) Maximum drift angle of 0.5% (b) Maximum drift angle of 1.0%

Figure 3.5. Summary of strain patterns developed for random inputs

The slit walls were subjected to a third loading protocol to addresses the behavior of strain patterns under short inputs. Short inputs replicate similar displacement conditions as shown by near-fault ground motions. In this analysis the short input is represented by three different loadings, each consisting of a single cycle to the drift levels studied in this section, i.e., 0.5%, 1.0%, and 1.5%. The resulting strain patterns developed by yield strain are shown in Figure 3.6. From the analysis of

the strain patterns shown in Figure 3.4 – Figure 3.6 it can be observed that the strain patterns developed at each drift angle are similar, independently of the input motion used.

It was noticed that the patterns developed for random inputs to a drift angle of 1.0% (Figure 3.5 (b)) are similar to those obtained for cyclic loading and single cycle inputs (Figure 3.6 (c)) for drift angles of 1.5%. This similarity might induce to misidentification of the drift angle. The difference in the strain patterns developed is probably caused by the larger number of cycles used for the random inputs, i.e. up to 10 cycles, compared to only one for the single input loading, and 3 for the incremental cyclic loading.

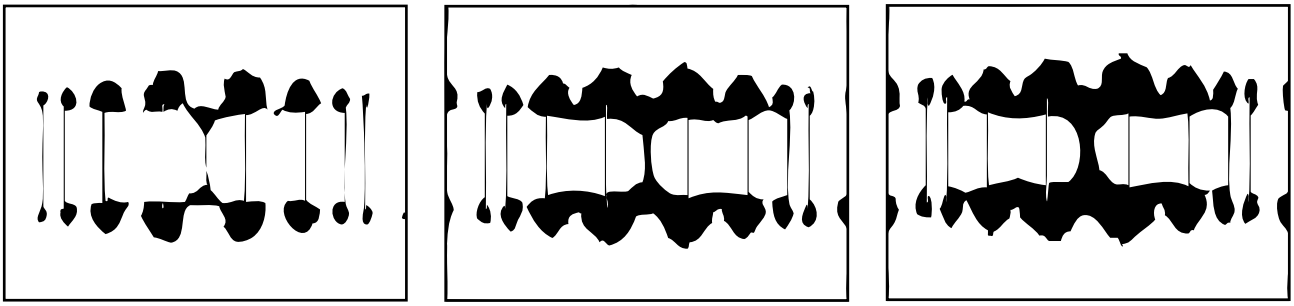

(a) 0.5% drift angle (b) 1.0% drift angle (c) 1.5% drift angle

Figure 3.6. Strain patterns for single cycle input

### 3.2.4 Real application example

In this section a real application of a slit design is presented, where out of plane deformations are included in the analysis. The inclusion of out-of-plane deformations generates pinching in the hysteresis; therefore, it stands to reason to evaluate the performance of the slit walls under cyclic loading. The target slit design is to display strain patterns that gradually change or grow as the drift angle increases while retaining the characteristics of the conventional slit design. Figure 3.7 (a) (top) shows the selected conventional slit wall. The slit wall has dimensions that are plausible for a real application (3900 mm in width, 3000 mm in height and a plate thickness of 18 mm). This conventional SW was selected as a starting point for the search for a suitable modified slit design. The design consists of two unslitted sections at the top and bottom of the steel plate and a central section with slits of a uniform distance of 200 mm and a height of 2000 mm. A finite element model was constructed to estimate the hysteretic characteristics of the SWs. The model was constructed according to the guidelines given in 3.2.1.

The model indicates that the uniform slit design defines a SW with an initial stiffness and yield strength of 48 kN/mm and 576 kN, respectively. Figure 3.7 (b) (top) shows in different shades of gray the spread of the yield strain on the SW for interstory drifts of 0.5%, 0.75%, 1.0% and 2.0%. Higher strain concentrations are observed at the ends of the slits, associated with the discontinuity in the strain field produced by the slits. As stated earlier, there is scant differentiation among the yield strain regions for each drift angle. To achieve a higher differentiation of the strain pattern for different drift levels, two modified slit designs were studied. In the studied designs, the width and height of the flexural links were altered along the length of the wall in a similar fashion as described

in 3.2.2 for Models C and D. In the previous section, Model C was selected as the better design for their increased size of the strain areas developed, but in this example a Model D type wall is also employed to present a contrasting example. By carefully adjusting the geometry of each flexural link, the properties of the SWs were fine-tuned to attain a hysteretic performance that is similar to conventional SWs while providing more freedom to the slit design.

The two variable slit designs are shown in Figure 3.7 (a), and their respective yield patterns are shown in Figure 3.7 (b). The slitting used for "Type A" design (Figure 3.7 (a) (center)) presents a uniform width of the flexural links (180 mm) and slits whose length diminishes from 1800 mm at the edge of the plate to 600 mm at the center of the plate. It is apparent from comparing the yield region of this SW and the conventional slit design in Figure 3.7 (b) that larger yield regions can be achieved by this design. The slitting used in "Type B" design (Figure 3.2 (a) (bottom)) presents slits of a uniform length of 1800 mm, but the width of the flexural links varies from 125 mm at the edge of the plate to 375 mm at the center of the plate. In this case the wider flexural link generates higher stresses at the ends of the slits and therefore larger yield regions than the conventional design. In the "Type B" design, the behavior was separated into two zones: one with uniform slitting at the edges of the plate, and the other with variable width at the center. By doing this, the strength and stiffness of the wall was adjusted to match that of the conventional design. Figure 3.7 (c) shows a comparison in the hysteretic response between the conventional and the modified slit walls. The two walls were made of steel plates of an identical width (3900 mm), height (3000 mm) and plate thickness (18 mm), and they were subjected to a cyclic load of a single cycle at amplitudes of 0.5, 1, 2 and 3% drift angle. It can be observed that the responses closely match for "Type A" design whereas "Type B" design presents a similar initial stiffness but a maximum strength 10% higher than that of the "Conventional" design. The increased hardening experienced by "Type B" design is attributed to the larger yield region that effectively increases the area of steel that undergoes hardening. Independent of the slit design adopted, the hysteretic curves show a stable behavior, and with strength deterioration only apparent after drift angles reach 3%. In the same manner as in section 3.2.2, "Type B" design is chosen for this study, since "Type B" design shows larger yield regions than that of the "Conventional" or "Type A" design.

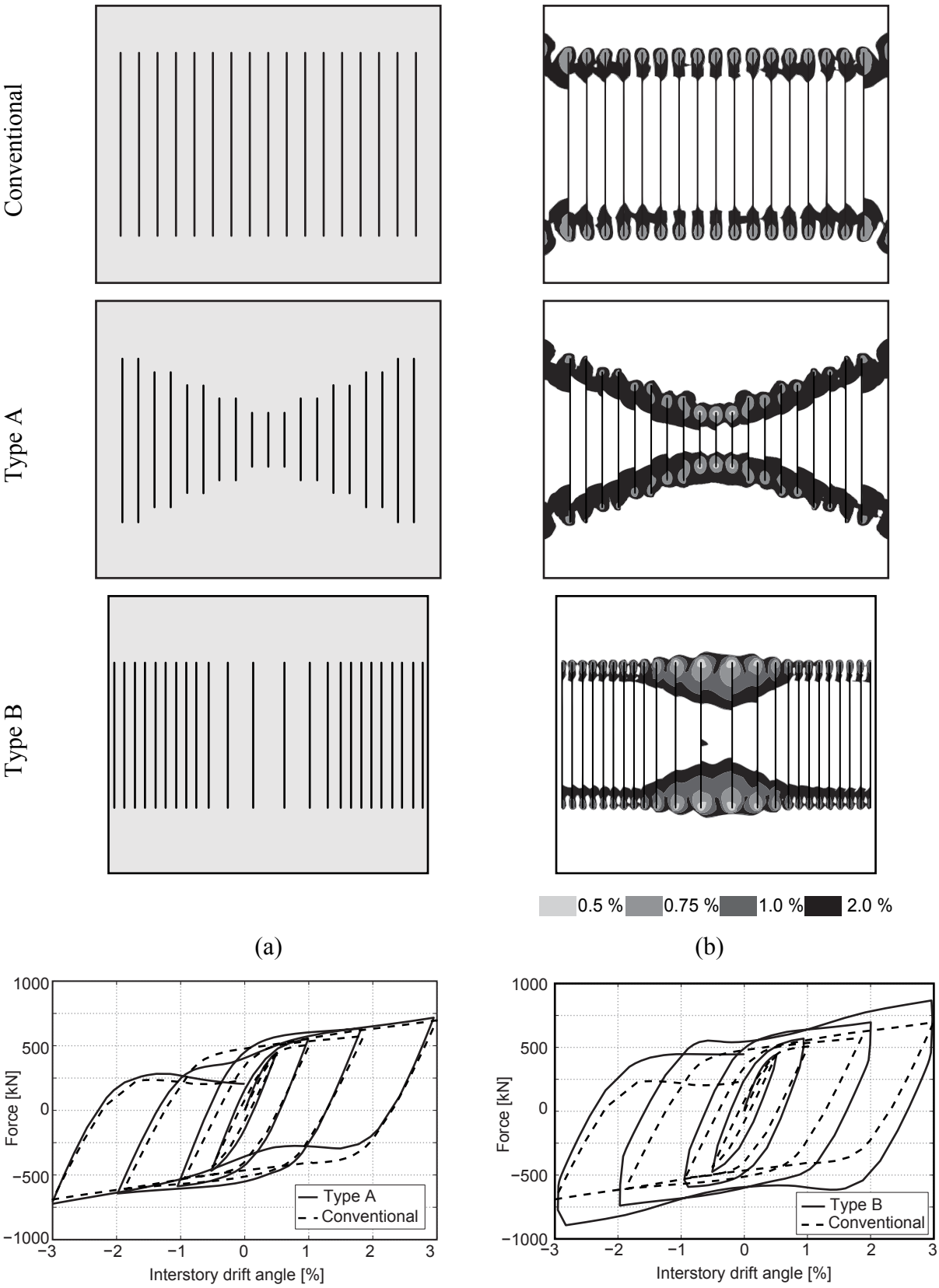


Figure 3.7. Modified slit designs: (a) Slit patterns;
(b) Strain distribution; (c) Hysteretic response.

## 3.3 Design Equations

### 3.3.1 Initial Stiffness

To estimate the initial stiffness of a slit wall, the behavior is separated into the behavior of the unslitted section of the plate and that of the slit row, and their corresponding stiffnesses are added in series. The unslitted section provides lateral stiffness through shear deformations. A single flexural links provides lateral stiffness through both shear and flexural deformations. Equations (3.1) and (3.2) provide the formulas for calculating each of the corresponding stiffnesses.

$$K_{unslitted} = \frac{GBt}{\kappa(h-l)} \tag{3.1}$$

$$K_{link} = \frac{1}{\frac{\kappa l}{Gbt} + \frac{l^3}{Etb^3}} \tag{3.2}$$

Where

κ is the shear deformation shape factor (equals to 1.2 for rectangular sections),

*G*: the shear modulus,

*B*: the total plate width,

*b*: the flexural link width

*h*: the full height of the plate

E: the Young's modulus of steel

*t*: the plate thickness and,

*l*: the length of the slits

The notation for both the conventional and alternative designs is summarized in Figure 3.8. The flexural links in the shear wall are connected in parallel, thus the stiffness participation can be expressed as the summation of the all the stiffnesses of the links.

$$K_{link\,row} = \sum_{i=1}^{n} K_{link_i} = \sum_{i=1}^{n} \left( \frac{1}{\frac{\kappa l}{Gb_i t} + \frac{l^3}{Etb_i^3}} \right) \tag{3.3}$$

Where *n* is the number of slits in the wall.

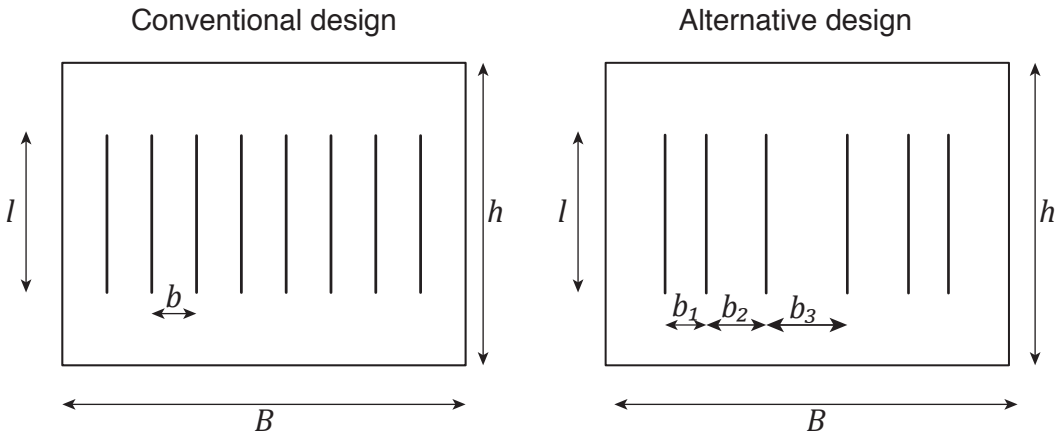

Figure 3.8. Slit Wall notation

Finally the total stiffness of the slit wall can be calculated as the summation of the stiffnesses (in series) of the unslitted and slitted sections of the plate.

$$K = \frac{1}{\frac{\kappa(h-l)}{GBt} + \frac{1}{\sum_{i=1}^{n}\left(\frac{1}{\frac{\kappa l}{Gb_i t} + \frac{l^3}{Etb_i^3}}\right)}} \tag{3.4}$$

In the conventional slit walls, all the flexural links have the same width; therefore the summation in Eq. (3.4) can be collapsed into:

$$K_{conventional} = \frac{1}{\frac{\kappa(h-l)}{GBt} + \frac{1}{n}\left(\frac{\kappa l}{Gbt} + \frac{l^3}{Etb^3}\right)} \tag{3.5}$$

Equation (3.4) is calculated assuming that the ends of the flexural links are perfectly rigid. This is not the case for slit walls, and the effect of the flexibility at the boundary should be considered in the estimation of the stiffness. Therefore the term $k(l,b)$ is introduced in equation (3.2) to reflect the development of local deformations in the unslitted section of the plate (past the ends of the slits) [1]. In other words, the term $k(l,b)$ has the effect of extending the flexural link beyond the area delimited by the slits by the width of the flexural link.

$$K_{link} = \frac{1}{\frac{\kappa h}{GBt} + k(l,b)\cdot\frac{l^3}{Etb^3}} \tag{3.6}$$

Where,

$$k(l,b) = \left(1 + \left(\frac{l}{b}\right)^{-1}\right)^3 \tag{3.7}$$

The results from FEM analyses indicate that the coefficient $k(l,b)$ calculated with Equation (3.7) consistently underestimated the stiffness of the flexural link. Furthermore, it does not take into consideration the effect that the neighboring flexural links have on the restraining of the

deformation of the unslitted section of the plate, i.e, if a narrow link is next to a wide one, the wide link will deform more because the boundary forces on the narrow link are much smaller. Equation (3.8) is an alternative to Equation (3.7) that provides a more accurate approximation, but does not consider the effect of neighboring links.

$$k(l,b) = \left(1 + \left(\frac{2l}{b}\right)^{-1}\right)^{3} \tag{3.8}$$

The introduction of the coefficient $k(l,b)$ in (3.2) is reflected on equation (3.4) as

$$K = \frac{1}{\frac{\kappa(h-l)}{GBt} + \frac{1}{\sum_{i=1}^{n_{sl}}\left(\frac{1}{\frac{\kappa l}{Gb_i t} + k(l,b_i)\cdot\frac{l^3}{Etb_i^3}}\right)}} \tag{3.9}$$

$$K_{conventional} = \frac{1}{\frac{\kappa(h-l)}{GBt} + \frac{1}{n}\left(\frac{\kappa l}{Gbt} + k(l,b)\cdot\frac{l^3}{Etb^3}\right)}$$

### 3.3.2 Maximum Strength

The strength of the slit wall is calculated in a similar fashion by assuming the formation of plastic hinges at the ends of each flexural link. Since the slitted section of the shear wall is the weakest, the maximum strength of the slit wall will be determined by the strength of the slitted section. A single flexural link can be analyzed as a prismatic beam. For prismatic beams, the full plastic moment $M_p$ is given by,

$$M_p = \frac{tb^2}{4}\sigma_y \tag{3.10}$$

The shear force associated with the plastic moment is,

$$V_p = \frac{2M_p}{l} = \frac{tb^2}{2l}\sigma_y \tag{3.11}$$

Finally, the maximum strength of the full slit wall will be the summation in parallel of the strength of the individual flexural links:

$$V_{SW} = \sum_{i=1}^{n_{sl}} \frac{tb_i^2}{2l}\sigma_y \tag{3.12}$$

In the case of the conventional slit design Eq. (3.12) is simplified to:

$$V_{SW_{conventional}} = \frac{ntb^2}{2l}\sigma_y \tag{3.13}$$

The yield shear force is used for design. In the case of slit walls, the yield shear force is calculated with the yield moment that can be approximated by $2/3M_p$. Thus,

$$V_{y_{SW}} = \sum_{i=1}^{n_{sl}} \frac{tb_i^2}{3l}\sigma_y$$
$$V_{y_{SW_{conventional}}} = \frac{ntb^2}{3l}\sigma_y \tag{3.14}$$

### 3.3.3 Application to the developed example

A comparison can be established between the results obtained in Section 3.2.4 for the design of Type B (slits of equal length and variable spacing) with the results obtained with the equations developed in Sections 3.3.1 and 3.3.2.

The FEM analysis of the conventional slit design indicated that the lateral elastic stiffness of this design was 48 kN/mm and the yield strength 576 kN. These values are calculated using the variants for conventional design stipulated by Equations (3.9) and (3.14), obtaining a stiffness of 52.1 kN/mm and a yield strength of 535 kN. In this case the equations reproduce FEM results with an error of approximately 7% in both values.

In the case of the Type B slit design, the results from the FEM analysis indicate that the lateral stiffness was 53.2 kN/mm and the yield strength was 580 kN. For this slit design the expanded variant of Equations (3.9) and (3.14) was used. The design equations indicate that the lateral stiffness is 59.4 kN/mm and the yield strength of the wall is 572.3 kN and the, with a 1.3% and 11%. The results obtained in this example are summarized in Table 3.3.

It is apparent that the estimations of the strength and stiffness are accurate in both examples. The results also highlight the improved accuracy in the calculation of the lateral stiffness that is provided by the modified coefficient $k(l,b)$ presented in equation (3.8). To provide some contrast, if the stiffness had been calculated using the $k(l,b)$ coefficient presented in equation (3.7), equation (3.9) would have predicted a stiffness of 68.11 kN/mm, with an error of approximately 28%.

Table 3.3. Comparison between FEM and analytical parameters of slit walls

| | Stiffness (kN/mm) | | | Strength (kN) | | |
|---|---|---|---|---|---|---|
| | FEM | Eq. (3.9) | Error (%) | FEM | Eq. (3.13) | Error (%) |
| Conventional Design | 48 | 52.1 | 7 | 576 | 535 | 7 |
| Type B design | 53 | 59.4 | 11 | 580 | 572.3 | 1.3 |

## 3.4 Study on individual flexural links

In the previous section, with the exception of the example in Section 3.2.4, the models considered only the in-plane behavior of slit walls. When out of plane deformations are introduced, the analytical formulation become more complicated as out-of-plane deformations introduce pinching in the hysteretic curves. Out-of-plane deformations are inherent to the behavior of slit walls. The importance of introducing slits resides on the prevention of global plate buckling by driving the buckling to the flexural links. Also, if the buckling behavior of flexural links can be accurately

predicted it would provide an alternative to the strains pattern method for condition assessment applications (described in Section 3.2).

This section presents an analytical formulation to predict the drift angle that induces buckling in the flexural links. A parametric study is conducted on individual flexural links to verify the analytical results and provide insight into the accuracy of the equations developed in Sections 3.3.1 and 3.3.2 as well as an estimation on the effect that pinching has on the energy dissipation capacity of the slit walls.

### 3.4.1 Lateral-torsional buckling equations

The original premises established in section 3.3 dictate that the behavior of each flexural link can be considered as independent, and the design of the slit walls is done based on this assumption. Unfortunately, the equations developed in the previous section also assume that the flexural links do not buckle before developing the plastic hinges. This assumption was validated experimentally [1] when the aspect ratio of the flexural links (height/width) is larger than 10. The validity of the assumption should be checked for flexural links with aspect ratios smaller than 10.

In slit walls, the boundary conditions of the flexural links are not strictly fixed or free. To simplify the problem, the buckling behavior will be studied assuming that the flexural link is equivalent to a simply supported beam; the loading is assumed to be double-curvature bending.

**<u>Simply supported beam under moment gradient</u>**

The energy equation for flexural-torsional buckling of an elastic beam [11] is given by

$$\frac{1}{2}\int_0^L \{EI_y(u'')^2 + EI_w(\phi'')^2 + GJ(\phi')^2\}dz + \frac{1}{2}\int_0^L M_x\{2\phi u'' + \beta_x(\phi')^2\}dz + \frac{1}{2}\int_0^L q_y(y_q - y_0)\phi^2 dz + \frac{1}{2}\sum Q_y(y_Q - y_0)\phi^2 = 0 \tag{3.15}$$

Where,

$L$: the length of the beam

$I_y$: the second moment of area of the beam

$u$: the deflection at the shear center in the longest direction

$I_w$: the warping section constant

$\phi$: the twist rotation

$G$: the shear modulus

$J$: the torsion section constant

$M_x$: the applied moment

$\beta_x$: the monosymmetric section constant

$q_y$: the distributed load applied on the beam

$y_q$: the distance of the distributed force from the centroid

$Q_y$: the concentrated force on the beam

$y_Q$: the distance of the concentrated force from the centroid

$y_0$: the coordinates of the shear center

$z$: the longitudinal axis through the centroid

As the flexural link is doubly symmetric, $\beta_x = y_0 = 0$. Furthermore, as a narrow rectangular section $I_w = 0$. Also, no loads are applied along the span of the link, $q_y = Q_y = 0$. Thus, equation (3.15) is reduced to:

$$\frac{1}{2}\int_0^L \{EI_y(u'')^2 + GJ(\phi')^2\}dz + \frac{1}{2}\int_0^L 2M_x\phi u''dz = 0 \tag{3.16}$$

In this case, we assume that flexural link is simply supported at the boundaries. Thus, the kinematic boundary conditions are

$$\begin{matrix} u_0 = 0 & u_L = 0 \\ \phi_0 = 0 & \phi_L = 0 \end{matrix} \tag{3.17}$$

Where $u_z$ and $\phi_z$ are the deflection and the twist rotation at point $z$ along the length of the flexural link. The moment gradient applied on the flexural link follows the equation $M_x = M(1 - 2z/L)$. As the flexural links bends in double curvature, the deflected shape $u$ is antisymmetrical, whereas the twist shape $\phi$ is symmetrical with respect to $z = L/2$. Therefore the buckled shaped may be approximated by,

$$\left.\begin{aligned} \phi &= \theta \sin\frac{\pi z}{L} \\ u &= \delta \sin\frac{2\pi z}{L} \end{aligned}\right\} \tag{3.18}$$

Replacing the buckled shaped defined in equation (3.18) in (3.16), leads to

$$\begin{aligned} \frac{1}{2}\int_0^L EI_y(u'')^2 dz &= \frac{1}{2}\left(\frac{\pi^4 EI_y}{L^4}\right)\int_0^L \left(4\delta \sin\frac{2\pi z}{L}\right)^2 dz \\ &= \frac{1}{2}\left(\frac{\pi^2}{L^2}\right)\left(\frac{\pi^2 EI_y}{L^2}\right)(16\delta^2)\frac{L}{2} \\ \frac{1}{2}\int_0^L GJ(\phi')^2 dz &= \frac{1}{2}\left(\frac{\pi^2}{L^2}\right)(GJ)\theta^2\frac{L}{2} \\ \frac{1}{2}\int_0^L M_x 2\phi u'' dz &= -\frac{1}{2}2M\theta\left(\frac{\pi^2}{L^2}\right)\int_0^L \left(1 - \frac{2z}{L}\right)\left(4\delta \sin\frac{\pi z}{L}\sin\frac{2\pi z}{L}\right)dz \\ &= -\frac{1}{2}\left(\frac{\pi^2}{L^2}\right)2M\theta\left(\frac{64\delta L}{9\pi^2}\right) \end{aligned} \tag{3.19}$$

When applying the boundary conditions established in equation (3.17) on equation (3.19), the energy equation becomes

$$\frac{1}{2}\frac{\pi^2}{L^2}\frac{L}{2}\begin{Bmatrix}\delta \\ \theta\end{Bmatrix}^T \begin{bmatrix} 16\pi^2\frac{EI_y}{L^2} & -\frac{128M}{9\pi^2} \\ -\frac{128M}{9\pi^2} & GJ \end{bmatrix}\begin{Bmatrix}\delta \\ \theta\end{Bmatrix} = 0 \tag{3.20}$$

Equation (3.20) is satisfied when

$$GJ = \left(\frac{64}{9\pi^2}\right)^2 \frac{4M^2}{16\pi^2 EI_y/L^2} \tag{3.21}$$

Therefore, the elastic buckling moment for a flexural link when modeled as a simply supported beam is,

$$M = \frac{9\pi^2}{32}\sqrt{\frac{\pi^2 EI_y}{L^2}GJ}$$
$$M = \frac{9\pi^2}{32}\sqrt{P_y GJ} \tag{3.22}$$

Where $P_y = \pi^2 EI_y / L^2$ is the Euler buckling load of the flexural link.

A similar deduction can be made for the case when the flexural link is modeled as fixed, but in this case the kinematic boundary conditions of Equation (3.17) are replaced by those in equation (3.23).

$$u_0 = 0 \quad u_L = 0$$
$$u'_0 = 0 \quad u'_L = 0 \tag{3.23}$$

Thus, in this case Equation (3.22) becomes

$$M = \frac{9\pi^2}{16}\sqrt{\frac{\pi^2 EI_y}{L^2}GJ}$$
$$M = \frac{9\pi^2}{16}\sqrt{P_y GJ} \tag{3.24}$$

Figure 3.9 shows the comparison between the aspect ratio of the flexural links and the critical moments calculated with Equations (3.22) and (3.24), normalized by the plastic moment of the flexural link calculated in Equation (3.10). On the left hand side the values are plotted against the link aspect ratio $l/b$, on the right hand side the values are plotted against the inverse aspect ratio $(l/b)^{-1}$ to provide a more common representation of the results. Both plots show the critical moment in thick line. This moment is defined by the minimum value between the plastic moment and the moments calculated with the energy equations. It is apparent from the left plot that the plastic moment controls the behavior of the flexural links for aspect ratios larger than 3.5.

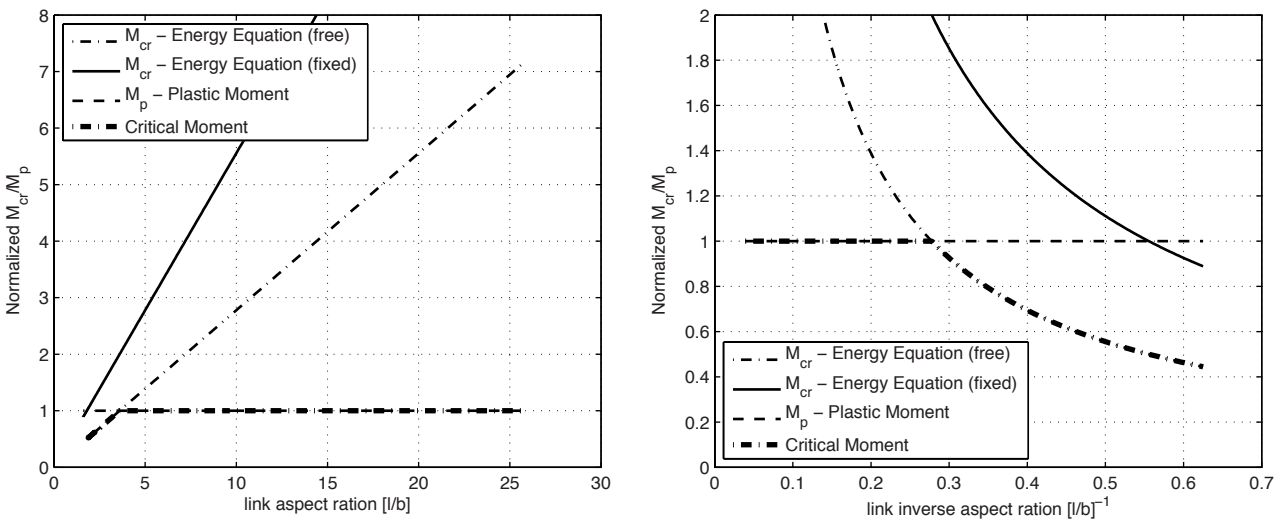


Figure 3.9. Comparison between link aspect ratio and normalized critical moments

### 3.4.2 Finite element model of individual flexural links

To provide an analytical frame of reference for the equations developed in the Sections 3.3.1, 3.3.2, and 3.4.1, a finite element model of a single flexural link was developed in ABAQUS. For the analysis, the flexural link is located between two sections of steel plate that represent the unslitted section of the wall (Figure 3.10). These plate extensions allowed the propagation of the strains in the direction opposite to the flexural link. Obtaining a more accurate approximation to the real boundary condition of the flexural link. The flexural links modeled have 640 mm in height (this height was chosen to be equal to that of a scaled specimen that was tested later and the results are reported in Chapter 5) and their width varies between 25 mm and 200 mm. A 6 mm plate is considered for the models. In this analysis the assembly is fixed at the top and bottom, out-of-plane deformations are restrained at the height where the flexural link connects to the plate, in order to concentrate the buckling in the flexural link without involving the plate extensions. A constant pressure equivalent to 1% of the maximum lateral resistance of the flexural link is applied on the surface of the flexural link to induce out-of-plane deformations. The model is analyzed under monotonic load to estimate the stiffness and maximum strength of the flexural links.

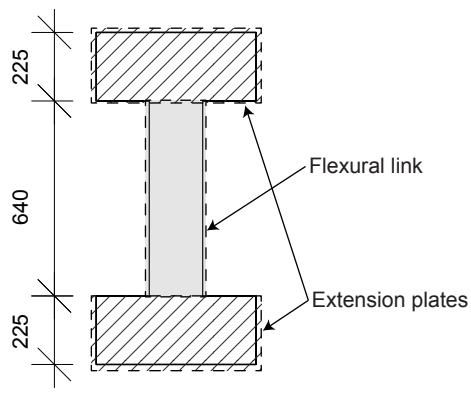


Figure 3.10. Diagram of analytical model of single flexural link

The results from the numerical analysis are shown in Figure 3.11. A good correlation between the numerical and analytical results from Equations (3.2), (3.6), (3.7), (3.8), and (3.11) was observed across the full range of aspect ratios.

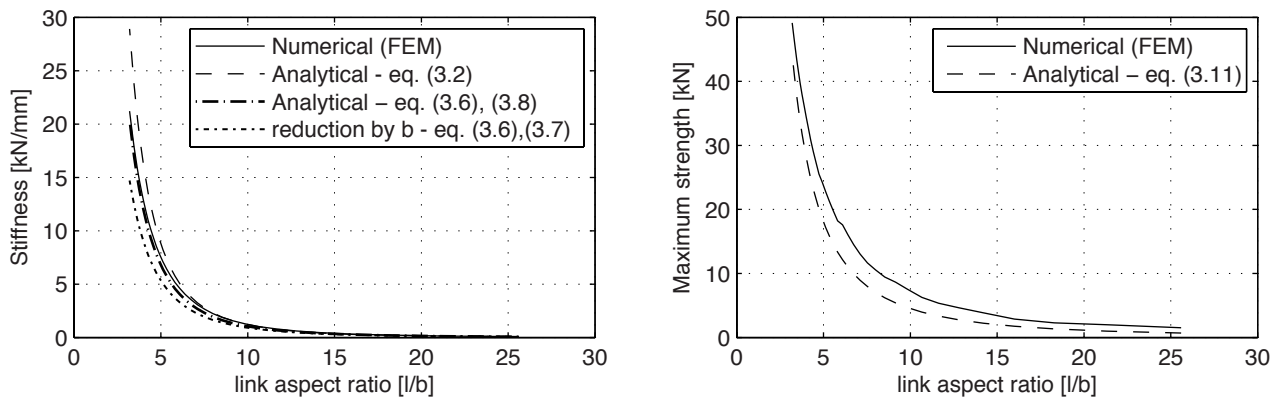


(a) Stiffness (b) Maximum strength

Figure 3.11. Comparison between the analytical and numerical results

### 3.4.3 Cyclic loading of FEM models

Later a new set of analyses were conducted. In this set the links were subjected to two cyclic load protocols: single and double cycles at each amplitude. The displacements imposed for the loading were equivalent to drift angles of 0.5, 1, 2 and 3% of a slit wall that has 1050 mm in height.The flexural links were studied in terms of their buckling displacement to establish the drift angles that initiate buckling. Figure 3.12 presents the loading protocols used for this study. Black circles marke the instance at which buckling initiated in the flexural links during the loading.

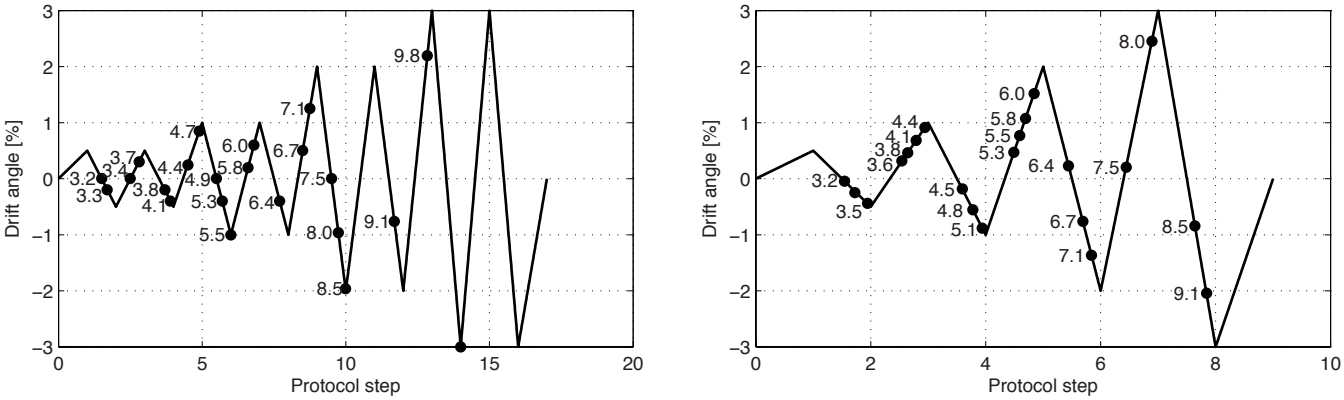


(a) Double cycle per amplitude (b) Single cycle per amplitude

Figure 3.12. Buckling instance at loading: the markers indicate the buckling instance for each aspect ratio

Careful inspection of Figure 3.12 reveals that flexural links of certain aspect ratios buckle at different drift angles. For example the flexural link with an aspect ratio of 6.0: in the double cycle per amplitude protocol (Figure 3.12 (a)), the link buckles in the cycle to 1%, whereas in the single cycle per amplitude loading (Figure 3.12 (b)), the link buckles in the cycle to 2%.

A better visualization of the results is presented in Figure 3.13. Figure 3.13 (a) shows the recorded instance of buckling initiation versus the drift angles for both loading protocols. In dashed lines are presented the buckling predictions made with equations (3.22), and (3.24). It is clear from this figure that all the buckling instances observed coincide with points that lay in between the two limit conditions established by the lateral-torsional buckling equations calculated in section 3.4.1, i.e., free to rotate (Equation (3.22)) and totally fixed (Equation (3.24)). The results obtained from the FEM analyses reflect an elastic boundary condition with certain stiffness due to the steel plate extensions, and it stands to reason that the points obtained in the analyses would be lay in between these two limit conditions.

Figure 3.13 (b) presents the residual deformations after buckling obtained from the same FEM analyses. Each flexural link develops buckling for a specific lateral drift angle, but if lateral torsional buckling were to be applicable for condition assessment applications, only the residual buckling would be observed during an inspection. Therefore this figure records the drift angles achieved before residual buckling was observed when the load returned to zero. For example, a flexural link with an aspect ratio of 6.5 buckles at 1% when loaded with a protocol that considers two cycles per amplitude, but buckles at 1.5% when loaded with a protocol that considers only a

single cycle per amplitude (the results presented in Figure 3.13 (a)). The corresponding residual buckling for this flexural link would be observed after the maximum drift angle has reached 1% for the double cycle-per-amplitude protocol, and 2% for the single cycle-per-amplitude protocol. These results are shown in Figure 3.13 (b). The important observation that can be drawn from this figure is that there are certain aspect ratios that develop buckling for both loading protocols, these aspect ratios are shown as dots enclosed by circles in Figure 3.13 (b), and they are located in the darker gray area of the plot. Therefore, these are the aspect ratios to be used to achieve condition assessment application by means of the residual out-of-plane buckling.

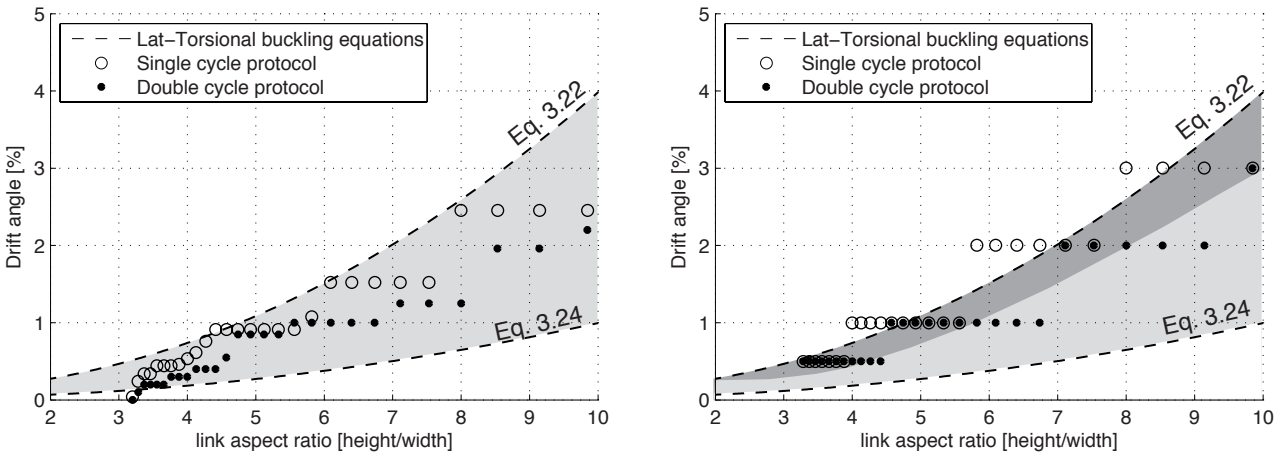


(a) Instance of buckling initiation (b) Recorded cycle for residual buckling

Figure 3.13. Buckling drift angle for flexural links of different aspect ratios

### 3.4.4 Energy dissipation performance

The inclusion of out-of-plane deformations in the analysis introduces degradation in the hysteretic curve. To estimate the effects of this degradation, the dissipated energy of each flexural link was compared to that of an equivalent elastoplastic damper with the same initial stiffness and yield strength. The dissipated energy was calculated as the enclosed area of the full cyclic loading (includes cycles to 0.5%, 1%, 2% and 3%). The performance ratio is defined as the quotient between the area enclosed by the flexural link and the area enclosed by the elastoplastic damper. The results are presented in Figure 3.14.

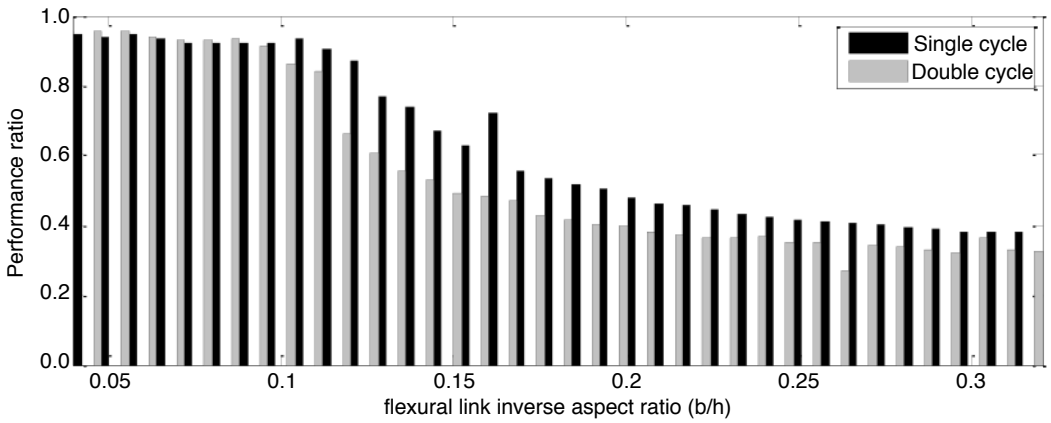


Figure 3.14. Performance ratio of flexural links for different aspect ratios.

In the figure we notice that the performance of the flexural links is constant and very close to 1.0 for links with aspect ratios below 1/10. For those links with aspect ratios larger than 1/10, the performance is reduced following an exponential trend that stabilized around 0.4 for aspect ratios beyond 3/10. The performance curve can be approximated by equation (3.25).

$$P = \begin{cases} 1.0 & if \quad \frac{b}{h} < \frac{1}{10} \\ 0.01 * \left(\frac{b}{h}\right)^{-2} + 0.3 & if \quad \frac{b}{h} > \frac{1}{10} \end{cases} \tag{3.25}$$

## 3.5 Conclusions

This chapter presented the conceptual work and analytical formulation of unequally slitted steel shear walls. The slit walls featured an innovative slitting pattern to add condition assessment capabilities without reducing the energy dissipation characteristics of the walls. A parametric study was conducted on individual flexural links to determine their performance. The major findings are summarized as follows:

(1) Unequally slitted steel shear walls retain the damping characteristics of conventional slit walls. Altering the slit configuration generates strain patterns that are unique to specific drift angles.

(2) The strength and stiffness of slit walls can be accurately predicted using a traditional formulation. The behavior of the slit walls can be separated into the behavior of the unslitted and slitted sections and the total behavior of the wall can be computed as the aggregation of the behavior of these sections. The predictions obtained from the equations developed show good agreement with finite element models.

(3) The out-of-plane deformations that take place in the flexural links can be predicted using the flexural-torsional equations of elastic beams. Furthermore, the drift angle at which buckling develops for specific aspect ratios can be predicted by these equations. Results from finite element models confirm the validity of the aforementioned equations.

## REFERENCES


[1] T. Hitaka and C. Matsui, "Experimental study on steel shear wall with slits," *J. Struct. Eng.-ASCE*, vol. 129, 2003, pp. 586 - 595.

[2] T. Hitaka, C. Matsui, and J. Sakai, "Cyclic tests on steel and concrete-filled tube frames with Slit Walls," *Earthq. Eng. Struct. D.*, vol. 36, 2007, pp. 707 - 727.

[3] A.E. Aktan, D.N. Farhey, A.J. Helmicki, D.L. Brown, V.J. Hunt, K.L. Lee, and A. Levi, "Structural identification for condition assessment: experimental arts," *J. Struct. Eng. - ASCE*, vol. 123, 1997, pp. 1674 - 1684.

[4] S.W. Doebling, C.R. Farrar, and M.B. Prime, "A summary review of vibration-based damage identification methods," *Shock Vib. Dig.*, vol. 30, 1998, pp. 91-105.

[5] H. Sohn, C.R. Farrar, F.M. Hemez, D.D. Shunk, D.W. Stinemates, B.R. Nadler, and J.J. Czarnecki, *A review of structural health monitoring literature: 1996–2001.*, Cambridge: Los

Alamos National Laboratory, 2003.

[6] T.T. Soong and G.F. Dargush, *Passive energy dissipation systems in structural engineering*, New York: Wiley & Sons, 1997.

[7] C. Christopoulos, A. Filiatrault, and V.V. Bertero, *Principles of passive supplemental damping and seismic isolation*, IUSS Press University of Pavia, Italy, 2006.

[8] A. Jacobsen, T. Hitaka, Y. Murata, J. McCormick, T. Wang, and M. Nakashima, "Condition Assessment Application of Steel Shear Walls with Slits," *Proceedings of the 14th World Conference on Earthquake Engineering*, Beijing, China: International Association for Earthquake Engineering, 2008.

[9] Abaqus Inc., "ABAQUS Version 6.7 User's Manual," *http://www.abaqus.com*, 2007.

[10] Matlab. The Language Of Technical Computing. *http://www.mathworks.com/products/matlab/*

[11] Timoshenko, S., and Gere, J. M. (1961). *Theory of elastic stability*, 2nd Ed., McGraw-Hill, New York, 239–250.

# CHAPTER 4

# Online test of a three-story building with slit walls

## 4.1 Introduction

In the previous chapter, two alternatives to achieve condition assessment applications were presented and demonstrated with FEM analyses. In this chapter an online hybrid test is conducted on a three story steel frame building installed with slit walls with unequal slitting pattern. The online test method has the potential to test large-scale structures since it does not require to physically simulate the inertial effect and a takes advantage from the extensibility associated with the substructure technique. In particular, the experimental substructures can be strategically selected and tested to capture the behavior of structural elements with complex hysteretic behavior while other, better-understood parts of the structure, can be modeled analytically.

### 4.1.1 Organization

This chapter is divided in three sections. In the first section, the design of the prototype structure, and the slit walls is examined. A brief description of the online test scheme and substructuring techniques is given. The second section presents the results from the online test: first on the overall behavior of the structure, followed by the local behavior of the slit walls. Finally the results from cyclic tests that followed the online test are discussed.

## 4.2 Design Stage

### 4.2.1 Prototype building design

A three-story, six-bay, one-span steel frame building (Fig. 4.1(a)) was selected as the prototype structure. The structure is a residential building in Japan. The backup frame is composed of five bays; the sixth bay sustains the seismic shear forces (Fig. 4.1(b)). In this bay, SWs are used as shear-resistant elements as well as damper devices. The section details for the frame are summarized in Table 4.1. The story height is 3.0 m, and the span length is 5.7 m. The total weight supported by each resisting frame is 7,100 MN. This structure was designed using current Japanese seismic design provisions [1] and satisfies the Building Standard Law of Japan [2] and all related design and construction codes [3], [4]. The structure was studied in the longitudinal direction because of the inclusion of SWs. The design intended that the SWs sustain approximately 40% of the base shear while the structure operates within the elastic domain.

The basic properties of the prototype structure were examined by pushover analyses in OpenSees [5], in which each column and beam was modeled as a line element with fiber sections to simulate the hinging mechanism, and the moment-rotation relationship of the plastic hinge was treated as linearly elastic and perfectly plastic. The interaction between the axial force and moment on the moment capacity was considered. The effect of the floor slab was ignored in this model. The gravity load was evenly distributed at the top of each column for each floor level, and the P-Δ effect was considered. The horizontal seismic force pattern followed an inverted triangular distribution. The SWs in the frame model were treated as equivalent elasto-plastic bracing systems. The equivalent braces retained the stiffness and maximum strength of the corresponding SWs. The analysis results (Figure 4.2) indicate that the structure behaves as intended in the design, i.e., remaining within elastic range for drift angles up to 0.005 rad, and sustaining a story shear coefficient of approximately 0.4 in the ultimate state. The natural period of the frame is 0.56 s. In the ultimate state, the SWs sustain 39%, 38%, and 46% of the story shear force for the first, second, and third stories, respectively.

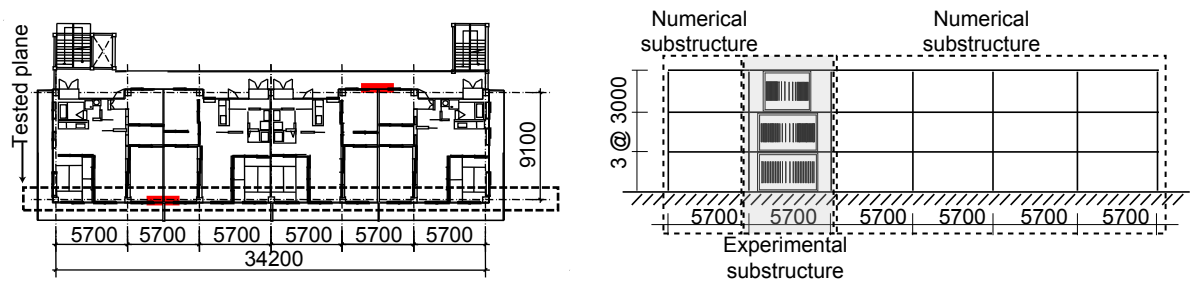


(a) Plan (b) Elevation

Figure 4.1. Prototype Building (unit: mm)

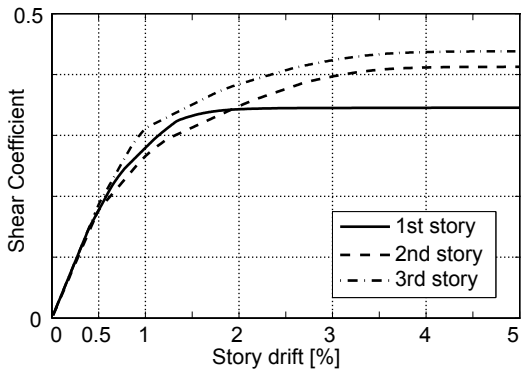


Figure 4.2. Prototype pushover results

Table 4.1: Frame section details

| Element Type | Story | Prototype dimensions | Specimen dimension |
|---|---|---|---|
| Beam | All | H 336 x 249 x 8 x 12 | |
| Column | All | H 350 x 350 x 12 x 19 | |
| Beam (SW) | 1st – 2nd | H 480 x 240 x 13.2 x 19.2 | H 200 x 100 x 5.5 x 8 |
| | 3rd | H 360 x 240 x 14.4 x 21.6 | H 150 x 100 x 6 x 9 |
| Column (SW) | All | H 428 x 422 x 35 x 35 | H 200 x 200 x 8 x 12 |

### 4.2.2 SW design

**Slit configuration**

The SWs were designed using the equations developed in Chapter 2. Namely, the slits were separated into two portions (Figure 4.3). The first, in the center of the plate, encompasses the flexural links intended for condition assessment purposes. A wider link is located at the center of the plate, and the subsequent links reduce in width as they draw farther from the center. The second portion, located at the borders of the plate, is constructed with a conventional slit design of uniform link width to adjust the strength and stiffness of the SW to the requirements of the corresponding story. This zone, which consists of flexural links with a much larger aspect ratio than those placed in the center, also provides restraining against Euler's buckling of the plate, as the thin flexural links tend to develop hinges at the ends rather than buckling out-of-plane as wider flexural links do. The designed SWs were 4.08 m in width for the first and second story and 3.12 m for the third story SW, and in all cases 15 mm thick steel plates were used.

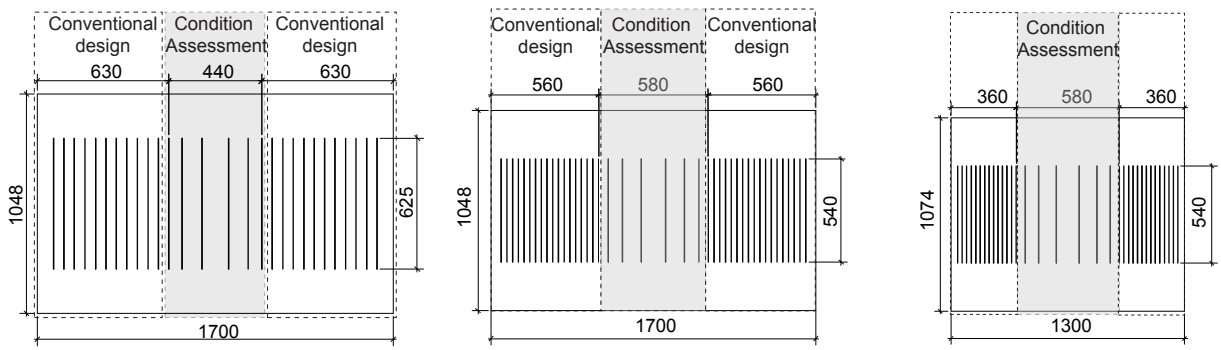


(a) 1F Shear Wall (b) 2F Shear Wall (c) 3F Shear Wall

Figure 4.3. Shear wall specimens (unit: mm)

### 4.2.3 Test setup

The structure is studied using an online hybrid test with a substructuring scheme [6]-[10]. When considering the relative difference in complexity of the hysteretic behavior of the elements within the structure, the span featuring the SWs presented the most challenging behavior. Therefore, the span featuring SWs was tested physically, while the backup frame was treated numerically (Figure 4.1 (b)) using OpenSees. The details of the analytical substructure were identical to those of the model used for the pushover analysis in the design stage, except for the absence of the span

featuring the SWs, which was removed in order to be tested physically.

The lateral displacements at each story level were taken as the boundary displacements between the physical and analytical domains (Figure 4.4). To achieve compatibility of the remaining DOF in the interface, the vertical displacements at the end of the beams in the analytical substructure were restrained, and the beam-ends were allowed to rotate freely. In the experimental substructure the rotations at the end of the beams were set to be free. These boundary relaxations introduced only minor variations in the response of the structure, as the smaller sections of the beams in the backup frame provide little force in comparison with the relatively heavy SW beams.

The experimental substructure was designed on a 1:2.4 scale to the prototype considering the capacity of the testing facilities. The section details for the experimental substructure are summarized in Table 4.1. Exactly scaled column sections were not available; therefore a section with a similar moment of inertia and plastic moment was selected. The steel used for the specimens was SS400 (JIS), the mild steel commonly used in Japan with a specified minimum ultimate strength of 400 MPa. The associated coupon tests indicate that the Young's modulus of the steel used is 1.9 x $10^5$ [N/mm$^2$], the post-yield stiffness is 1.3% and the yield strain is 240 [N/mm$^2$]. . The specimen's beam-column connections were shop welded. As illustrated in Figure 4.3, for the first and second story SWs, the steel panels had the dimensions of 1700 mm x 1050 mm x 6 mm. The third-story SW had the dimensions 1300 mm x 1075 mm x 6 mm. As shown in Fig. 5(b), the SWs were connected to each story beam flange using steel angles and high strength bolts. These bolts were designed such their the maximum shear capacity would exceed the anticipated horizontal strength of the SW. To prevent yielding in the panel zone of the beam-to-column connection, two 4.5 mm thick double steel plates were fillet-welded at each side of the column web. Dog-bone indentations (15% of the flange width) were included at the beam end and at the base of the first-story column to adjust the strength characteristics of the elements.

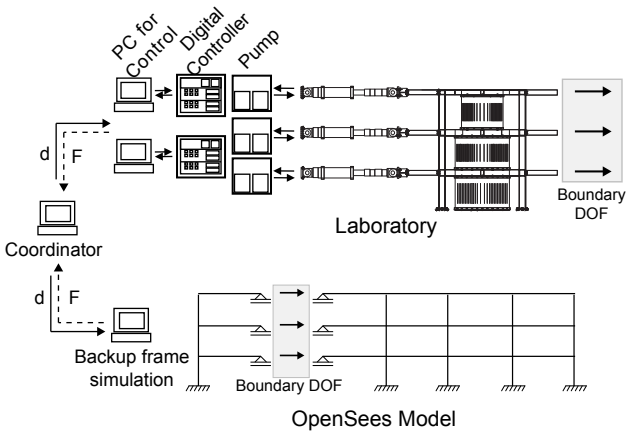


Figure 4.4. Online test scheme

Figure 4.5 (a) and (b) shows the loading setup. Out-of-plane deformations were prevented by attaching a restraining frame to the beam extensions at each story level through rollers, while the restraining frame allowed for free horizontal and vertical movement of the beam extensions in the

plane of the frame. The horizontal load was applied to the specimen by three 1.5 MN hydraulic jacks at floor levels connected to the specimen by the beam extensions

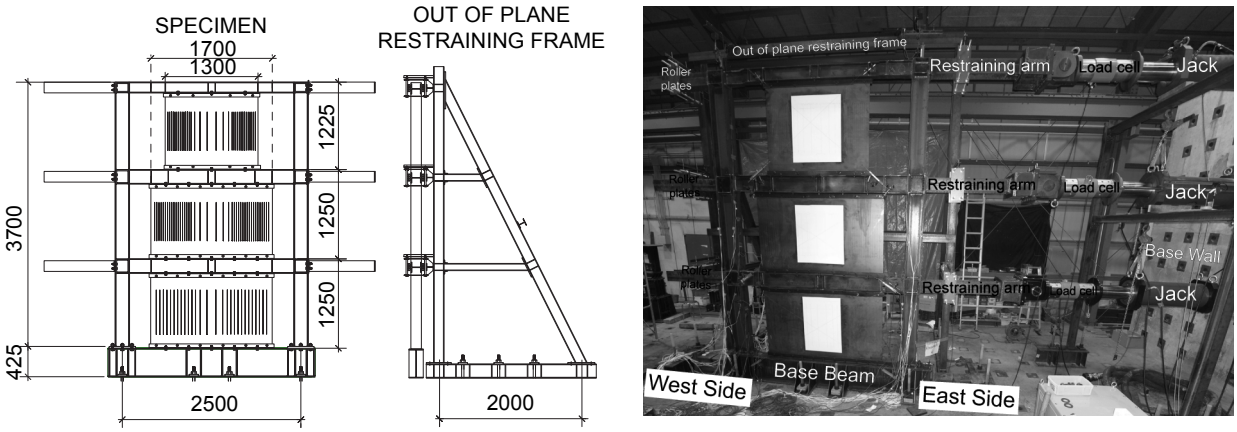


(a) Schematics (b) Picture

Figure 4.5. Experimental substructure

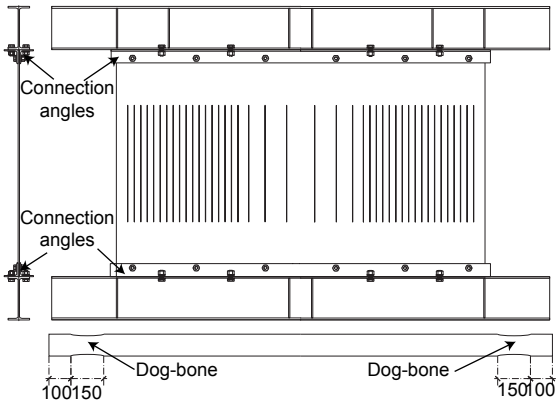


Figure 4.6. SW connection angles and dogbone indentations

### 4.2.4 Basic online scheme

The online framework used for this study consisted of a "coordinator" program and two "stations" [11], [12] that managed the numerical and physical substructures (Figure 4.4). The "coordinator" solved the equations of motion for the complete structure using a lumped mass, three-DOF model, and provided an interface to all the substructures. The "stations" calculated the restoring forces of the substructures, whether simulated numerically or tested physically. Within the "coordinator", an operator splitting method [13] was employed to determine the compatible boundary displacements by systematically minimizing any unbalanced forces. For this test, the initial stiffness matrix of the experimental substructure was established by loading the specimen with small displacements. Global predicted displacements were calculated in the coordinator by solving the equation of motion using a linear approximation. The corresponding incremental displacement vectors assigned for the substructures were sent to all stations after the displacements had been scaled accordingly. Testing started in the stations, i.e., the numerical substructure and the test specimen were loaded to the respective target displacements. Upon completion of loading, the

reaction forces were measured and sent to the coordinator, and the response was corrected according to the forces obtained after loading. The procedure was repeated up to the end of the online test.

### 4.2.5 Measurement

A load cell attached to the head of each jack measured the horizontal load applied by the jack. Digital displacement transducers that had a resolution of 0.01 mm were used to measure the displacements of the jacks. In addition to those transducers, three displacement transducers were attached to the other end of the specimen to measure the lateral displacement achieved in the frame. Four strain gauges were glued to each column flange at each story level and at two cross-sections, each located at a distance equal to one third of the story height. It was assumed that the steel at the middle third of the column would remain elastic even to large deformation levels. Using the strain data from these portions, the curvatures of the sections were calculated. The corresponding bending moment and the shear responses of the columns were calculated using the curvatures, moment of inertia, and Young's modulus of the column steel. The shear force carried by the SW was obtained by subtracting the column shear force from the total shear force applied by the jacks. Displacement transducers having a variety of gauge lengths measured displacements of various locations, including shear deformations of the SW, column shrinkage and any possible slip at the column bases. Furthermore, fifty-six strain gauges were glued to the condition assessment zone of the SW to study the local strain behavior at the end of the slits that would sustain plastification. A total of 95 data channels were connected to the measuring system. A brittle lacquer compound [14] was applied to one side the condition assessment zone of the SW of each story to record the spreading of strain throughout the testing.

### 4.2.6 Test procedure

A time interval of 0.01 s was adopted for the online hybrid simulation of the structure. The fault-normal ground motion recorded at the JR Takatori station during the 1995 Hyogo-ken Nanbu earthquake was used (Figure 4.7). The ground motion was the largest recorded in the earthquake, with the maximum ground acceleration and velocity as 6.66 m/s$^2$ and 1.69 m/s, respectively. The ground motion was scaled in two levels to make it commensurate with but somewhat larger than the design earthquake force stipulated in the Japanese seismic design [1], [4]. Note that in the Japanese seismic design, the PGV of 0.5 m/s is adopted for the large earthquake force, and half the force is used for serviceability check. In this study, the motion was reduced by a factor of 0.2 and 0.4, respectively, and the corresponding PGVs were 0.34 m/s and 0.68 m/s for the first and second levels. The first ten seconds of the ground motion records, containing the largest components of the acceleration, were considered. After each application of the ground motion, the load applied to the experimental substructure was released. The residual deformations were taken as the initial state for the subsequent application of the ground motion.

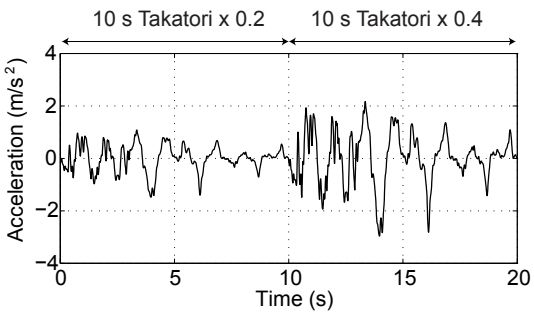


Figure 4.7. Input ground motion

## 4.3 Online test results

### 4.3.1 Individual SW performance

All SWs yielded at a drift angle of about 0.55% and exhibited stable hysteretic behavior with gradual transition between the elastic and inelastic regions. In the first online test in which the JR Takatori ground motion was scaled at a 20% in the amplitude, the SWs presented mild yielding with a ductility ratio of 1.32 in the second story SW, and ductility ratios of 1.09 and 1.27 in the first and third stories. The surrounding frame remained elastic during the first online test. In the second online test in which the JR Takatori ground motion was scaled at a 40%, the SWs in all stories experienced substantial yielding. The highest ductility ratio was obtained for the second-story SW (3.51), and ratios of 3.34 and 3.04 were obtained for the first- and third-story SWs, respectively. The shear force in the SW versus interstory drift relationships for the second online test are illustrated in Figure 4.8. The shear force on the SW was obtained as the story shear force minus the shear force estimated on the columns. Slipping in the connection between the SW connection angles and the beam caused sudden drops in the resisting force by an average of 20%. The slipping was caused due to the yielding of the outermost bolts of the wall-to-beam connection, as a result of additional vertical forces induced by the overall bending of the SW over the pre-tension of the bolts.

Shown in thick line in Figure 4.8 are the pushover curves of each SW obtained from a nonlinear finite element analysis. Good agreement is observed between the prediction obtained from the finite element analysis and the behavior observed in the test. For the analysis, the SWs were modeled as shell elements, and the mechanical properties obtained from the associated standard coupon tests were adopted. The SWs were assumed to be fixed in the base, and the lateral displacement was imposed at the top of the SWs. The top boundary was allowed to move in the vertical direction (through shrinking of the SW), but it was not allowed to rotate. Out of plane deformations were restrained only at the boundaries. An initial imperfection was given as one half of a sinusoidal wave with amplitude equal to 1/100 of the length of the wall.

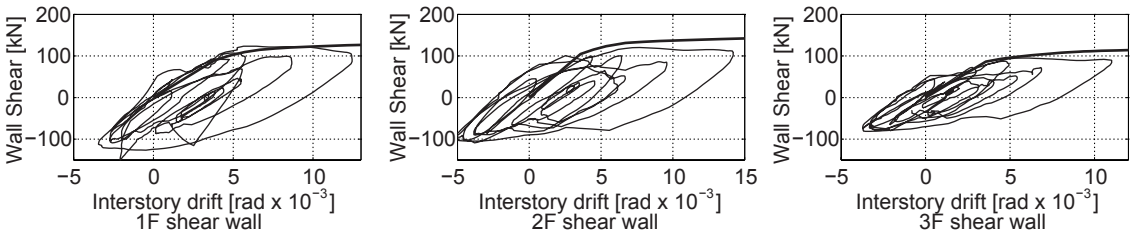


(a) 1st story SW (b) 2nd story SW (c) 3rd story SW

Figure 4.8. Wall shear versus shear drift relationships in the experimental substructure for JR Takatori 40%

As observed in Figure 4.8 and Table 4.2, the stiffnesses of the SWs were predicted with an accuracy of 83% for the first-story SW and 70% for the second- and third-story SWs. In a similar fashion, the strength of the SWs were predicted with an accuracy of 87% for the second- and third-story SWs, and the strength of the first-story SW was underestimated by 4%. The disparities between the tests and analyses are most likely associated with the difference in the boundary conditions between the FEM model and the experimental setup. The results of the SW installed in the first story show better correlation than those of the other stories, and this is associated with the stricter boundary conditions of this story, i.e., the base of the story was fixed whereas the top was attached to a beam. In the second and third stories, the beams define the boundaries of the SWs. The bending of the beams allows for small rotations at the boundaries of the SWs, and this rotation reduces the efficiency of these SWs.

Table 4.2. Comparison in stiffness and strength between the prototype and test

| | Story | | | | | | Shear Wall | | | | | |
|---|---|---|---|---|---|---|---|---|---|---|---|---|
| | Stiffness (kN/mm) | | | Strength (kN) | | | Stiffness (kN/mm) | | | Strength (kN) | | |
| Story | P | E | R | P | E | R | P | E | R | P | E | R |
| 1 | 211.6 | 107.85 | 51% | 2458 | 2372 | 97% | 53.4 | 44.4 | 83% | 711.4 | 745.3 | 104% |
| 2 | 78.5 | 77.96 | 99% | 2048 | 1893 | 92% | 61.4 | 42.6 | 70% | 808.7 | 709.5 | 87% |
| 3 | 83.6 | 63.74 | 76% | 1229 | 1207 | 98% | 55.2 | 33.9 | 72% | 646.8 | 555.9 | 86% |

P: Prototype values; E: Experimental values; R: Ratio, prototype/experimental

Out-of-plane buckling in the same manner as lateral-torsional bucking of beams (Figure 4.9 (a)) was observed in the inner flexural links (unequally slitted) as soon as the SW started yielding (story drift angle of 0.47%). The buckling extended to all the flexural links within the condition assessment zone but did not propagate to the equally slitted zone for the drifts angles achieved during the test. Out-of-plane buckling was also observed on the flexural links at the edges of the SW (Figure 4.9 (b)). This buckling was associated with tension-compression forces induced in the edge links as a result of the frame effect shown by SW with a small aspect ratio, i.e., their width is larger than their height. In the first- and second-story SWs, the aspect ratio, height divided by width, is 0.61.

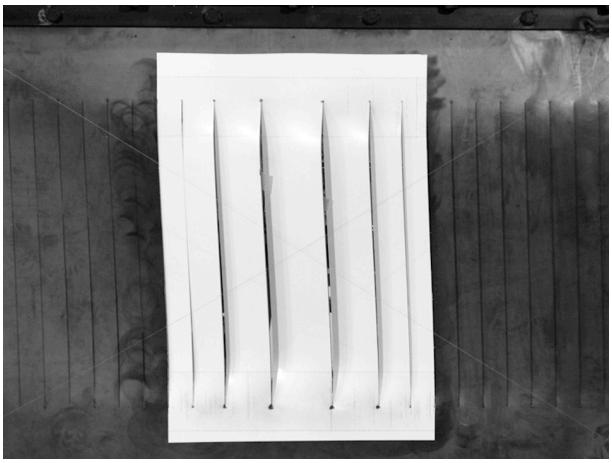

(a) Condition assessment flexural links

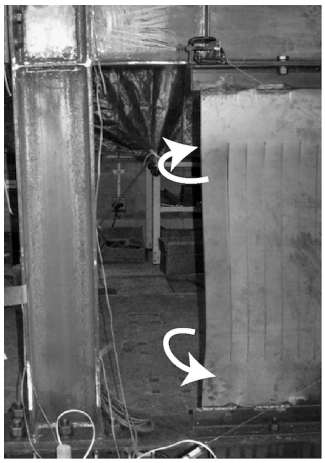

(b) Exterior flexural links

Figure 4.9. Out-of-plane bucking of the first story SW

Data obtained from strain gauges placed near the slit ends indicate that flexural links began to plastify at 0.2% drift angles. This plastification is due to the stress concentration generated at the slit ends, and represents a local strain concentration rather than the formation of a plastic hinge at the ends of the flexural links.

### 4.3.2 Structure performance

Both online tests were performed satisfactorily without any malfunction of the test control and operating system. The error between the target displacement signal sent to the jack and the achieved displacement is not greater than 0.1 mm for most of the steps. The error shows isolated peaks, at 11 steps for the second-story SW, and 4 steps for the third-story SW, that reach 0.2 mm for target displacements that correspond to zero lateral force, as the oil pressure in the jacks is very low in that region.

The specimen frame behaved in a stable manner during the online tests. The roof displacement responses obtained during the online test are plotted in Figure 4.10 (a) and (b), and are compared with the results when the entire structure is analyzed numerically in OpenSees. The model used for the pushover analysis was used for the numerical analysis of the entire structure. The responses are similar to each other in amplitude, with differences of 10.5 and 5.9 mm in the maximum roof displacement for the 20% and 40% scales of the JR Takatori ground motion, respectively. A slight shift in the response period was observed in the Level 1 response. According to an associated frequency analysis, the shift was about 0.06 s in the dominant frequency, and it was likely caused by the flexibility of the beam extensions attached to the jacks. Figure 4.11 shows the maximum interstory drifts obtained for the two levels of ground motions studied in the test. A uniform story drift distribution was observed for both intensities of the ground motion, while the second story sustained 12% larger drift relative to the other stories. The results indicate that the structure complied with the maximum drift limits of the Building Standard Law of Japan [2] for Level 1 earthquakes. The peak velocity of the ground motion was 0.34 m/s, whilst the peak velocity established for Level 1 was 0.25 m/s. If the ratio, i.e., 0.74 was applied, the maximum story drift would be 0.45%, which is smaller than the limit of 0.5%.

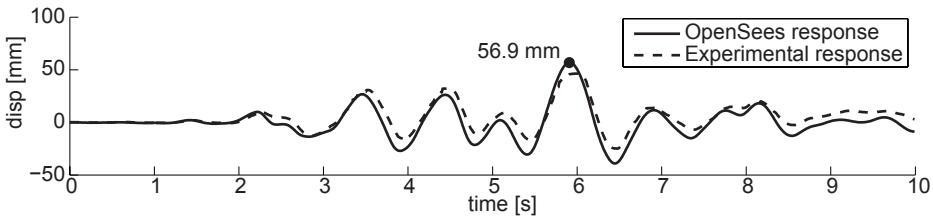


(a) JR Takatori 20% scale

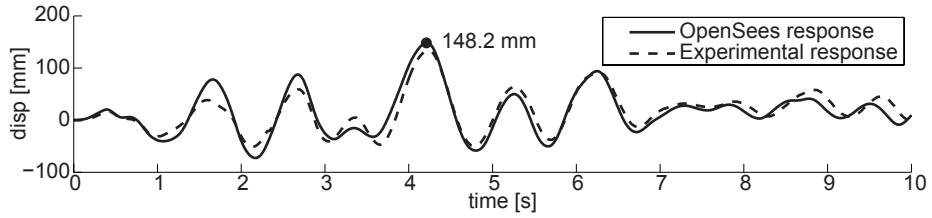


(b) JR Takatori 40% scale

Figure 4.10. Comparison of roof displacement time history between online test and numerical analysis

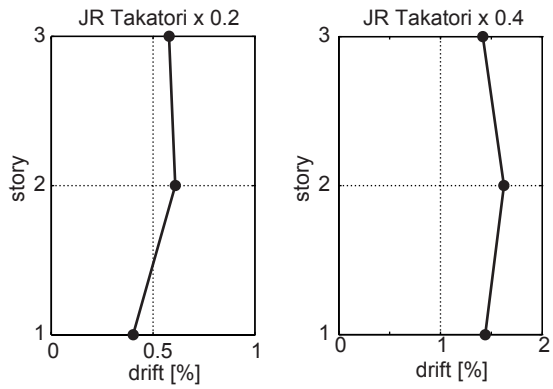


(a) JR Takatori 20% (b) JR Takatori 40%

Figure 4.11. Story maximum drift angles.

Strain gauge data indicates that neither beams nor columns went into the inelastic range for the Level 1 ground motion. Despite this, the hysteretic curves obtained for the columns suggest that very mild inelasticity was experienced in the beams for the largest cycle in this ground motion. The SWs experienced minor yielding for the largest cycles of the response in accordance with what was expected in the design. For the Level 2 ground motion, the yielding started at 1.6 s in the east end of the second-story beam; both ends of the third-story beam yield at 2.1 s. At 4.0 s the west end of the first-story beam and column base yielded, followed by the east column base at 4.1 s. Finally, at 5.2 s, the east end of the first story beam yielded. The plastic redistribution follows the pattern expected in the design stage, where the hinges develop in the beam-ends before the bases of the columns yield.

According to the data obtained from the strain gauges attached at the column flanges, yielding in the beams initiated at drift angles of 1.02%, 0.7% and 0.63% in the first, second, and third story, respectively. The larger yield drift angle in the first-story beams can be explained by the

dissymmetry of the first story's boundary conditions. This dissymmetry shifted the inflexion point toward the top of the story and resulted in the decrease in the moment at the beam-to-column connection. There was no visual evidence of yielding in the panel zone of the beam-to-column connection. There was no evidence of local buckling in the beams or column bases, either.

Figure 4.12((a), (d) and (g)) shows the hysteretic response of each story for the JR Takatori 40% ground motion; Figure 4.12((b), (e) and (h)) shows the hysteretic response of the columns of each story calculated based on the data obtained from the strain gauges located on the column flanges. The data indicate that the column inelastic behavior initiates at interstory drift displacements of approximately 10 mm (0.8%) in all stories, whereas the SW yields at about 5 mm (0.47%) drift. This behavior is concordant with the design objectives, as the SWs yield earlier than the columns. There was no visual evidence of yielding in the panel zone of the beam-to-column connection. There was no evidence of local buckling in the beams or column bases, either.

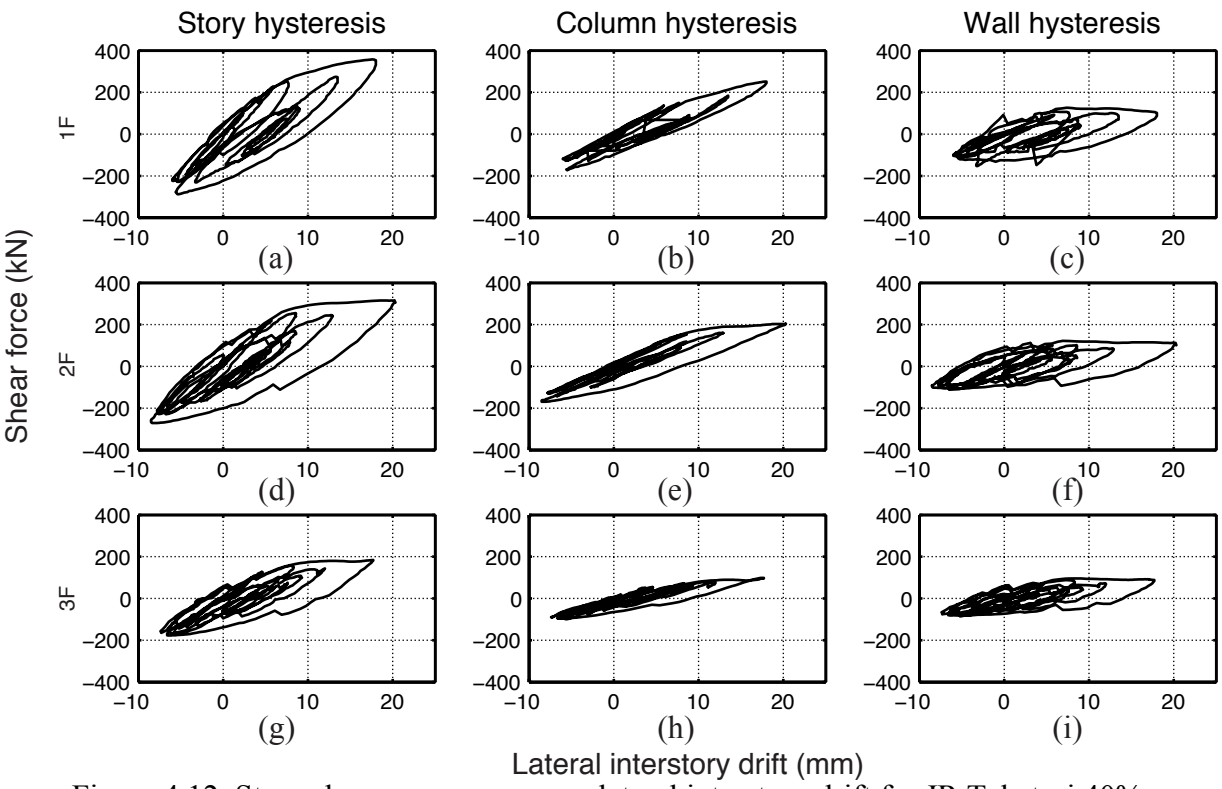


Figure 4.12. Story shear response versus lateral interstory drift for JR Takatori 40%.

Energy dissipation was estimated using the data provided by the displacement transducers and strain gauges placed in the columns. For the Level 1 ground motion a total of 71.7 x $10^6$ J were dissipated; 71% by SWs, 22% by columns and beams of the specimen, and 7% by the backup frame simulated numerically. For the Level 2 ground motion, a total of 509.8 x $10^6$ J were dissipated, where SWs dissipated 75%, the columns and beams of the specimen 14%, and the backup frame 11%. Figure 4.13 illustrates the accumulated energy dissipation for the Level 1 and Level 2 ground motions, (a) and (b) respectively. The contribution of SWs to the total dissipation is apparent after 1 s and predominates throughout the response. The accumulated energy results clearly indicate that the SWs represent a functional damper device, dissipating more than 70% of the input energy, even

for small excitations such as the JR Takatori ground motion scaled to 20%.

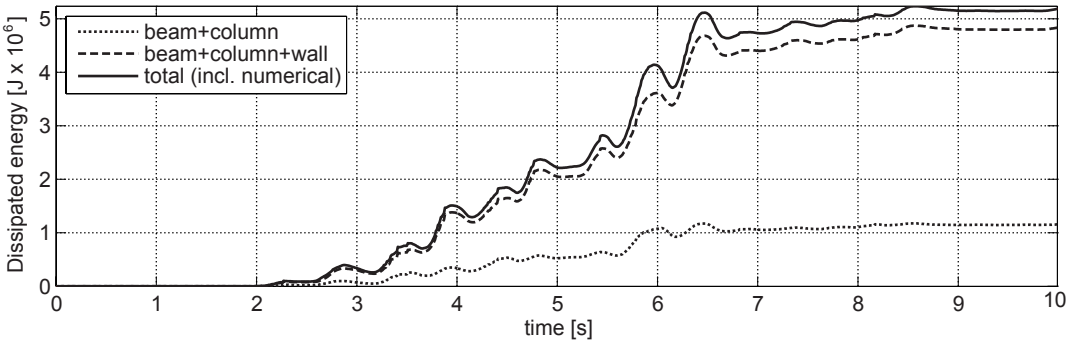


(a) JR Takatori 20% scale

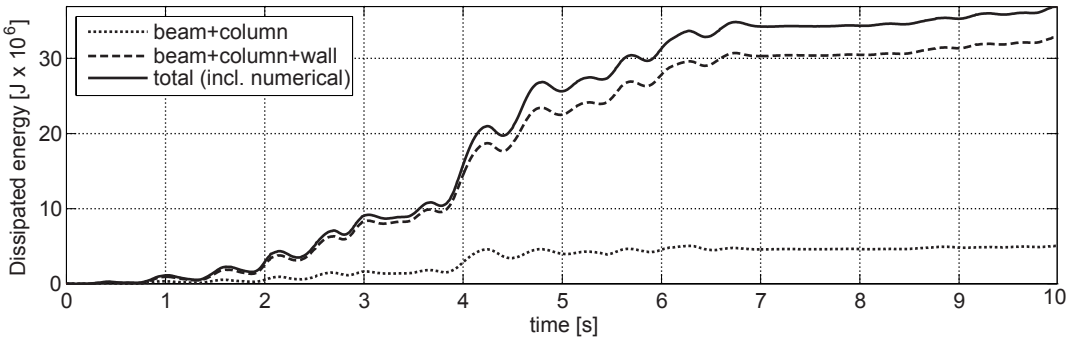


(b) JR Takatori 40% scale

Figure 4.13. Accumulated energy history.

Energy dissipated for the Level 1 ground motion was evenly distributed along the height among the columns. Among SWs, the second-story SW dissipated the most energy (44%), consonant with a higher drift experienced by this story (0.6% story drift) and the early yielding of the SW. Each of the first- and third-story SWs dissipate 28% of energy. For the Level 2 ground motion, the SW dissipation was 31%, 41% and 28% for the first, second and third stories, respectively. The cumulative plastic deformation for the SWs was calculated for the both instances of the application of the JR Takatori ground motion. Table 4.3 summarizes the cumulative plastic rotations after each of the tests. In general, plastic rotations of approximately 18% were experienced by the SW specimens without exhibiting any damage of strength degradation.

Table 4.3. Cumulative plastic rotation for online test.

| | | 1st story SW | 2nd story SW | 3rd story SW |
|---|---|---|---|---|
| JRTakatori motion | 20% scale | 0.012 | 0.0332 | 0.028 |
| | 40% scale | 0.163 | 0.226 | 0.190 |

## 4.4 Cyclic testing

After the online testing of the frame specimen, only small damage was observed in the SWs, thus, to retrieve as much information as possible the SWs specimens were salvaged for further testing under cyclic loading.

In order to test in the new loading frame, the specimens had to be removed from the steel frame where they were mounted. New perforations had to be drilled to accommodate for the residual deformations, and the height had to be adapted to that of the new loading frame.

### 4.4.1 Test setup, loading history, and measurement

**Test setup**

Based on the existing facilities, the test setup shown in Figure 4.14 was developed. The test specimens were installed between two wide flange sections, securely fastened by eleven M16 bolts (snug tight) on each side. Forced displacement was applied quasi-statically to the specimen by a 1 MN capacity, computer-controlled, hydraulic jack via the top beam. To ensure the horizontality of the applied load, two pinned columns were attached to the loading frame. To prevent the loading frame from deflecting out-of-plane, lateral supports (with rollers) were provided (not shown in the figure). The complete test setup rested on a reaction frame that was significantly stiffer. The centerline of the actuator implied an eccentricity to the specimen, measured 1538 mm to the centerline of the specimen. A free-run of the setup (i.e. without the specimen installed) was performed, and the result showed that friction effects were considerably negligible. The test setup was robust and repeatable, and no visible damage to the testing frame occurred after all tests were carried out.

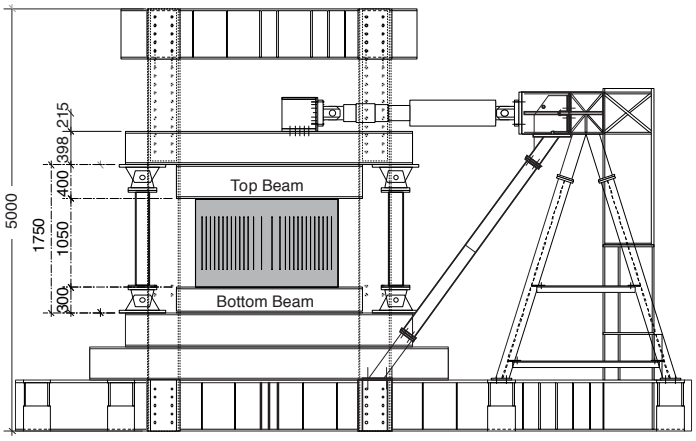


Figure 4.14: Experimental setup for cyclic test

**Loading history**

Considering that during the online test, several small cycles of the shear wall were experienced. The focus of this stage of testing was to study the behavior of slit walls under heavy demands. Therefore, two cycles at amplitudes corresponding to drift angles of 1, 2, 3, 4, 6 and 8% were applied to the three slit wall specimens.

**Measurement**

Displacements of the specimens were measured independently by an LVDTs, attached to the top of the loading frame and two additional LVDTs placed diagonally across the specimen connecting the top and bottom beam. A load cell attached to the head of each jack measured the horizontal load applied by the jack. Digital displacement transducers that had a resolution of 0.01 mm were used to measure the displacements of the jacks. In addition to those transducers, three displacement transducers were attached to the other end of the specimen to measure the lateral displacement achieved in the frame. Four strain gauges were glued on each column flange at each story level and at two cross-sections, each located at a distance equal to one third of the story height. It was assumed that the steel at the middle third of the column would remain elastic even to large deformation levels.

### 4.4.2 Hysteretic characteristics

For the first series of tests, stable load deformation envelopes were achieved for each test specimen for drift angles below 0.03 rad. For loadings above this drift angle, the hysteresis loops were spindle shaped, and stable. A narrow elastic region is observed in the test results, in accordance to the original deterioration that the specimens suffered during the online test. OA in Figure 4.15 denotes the initial elastic stiffness obtained during the test (9.9 kN/mm in the case of the first specimen). The initial elastic stiffness degrades to approximately a 30% (3.24 kN/mm for the same specimen) when the drift angle reaches 0.005, and this later stiffness is maintained throughout the loading (AB in Figure 4.15). As the load reversed after the end of each cycle, the unloading stiffness started as parallel to the initial elastic stiffness (CD), but smoothly transitioned to the reduced stiffness as the specimen started taking force in the negative direction (DE). Figure 4.15 shows the results from the online test in the dotted line. In this test the calculated initial stiffness was 21 kN/mm and the yield strength was 100 kN when the drift angle reached 0.0047 rad, compared to these results the specimen tested under cyclic load shows approximately a 50% reduction in both elastic stiffness and yield strength. In the post-yield region (Figure 4.16), several well-defined segments of the load deformation curves represented the various stages of loading, unloading, and the segment with zero stiffness, i.e., where the flexural links did not carry lateral load since they were buckled. Increased energy dissipation was achieved with each drift angle increment in the post-yield region. A 20% decrease in energy dissipation between subsequent cycles at the same load level was noted for drift angles on excess of 0.03 rad, due to buckling in the flexural links.

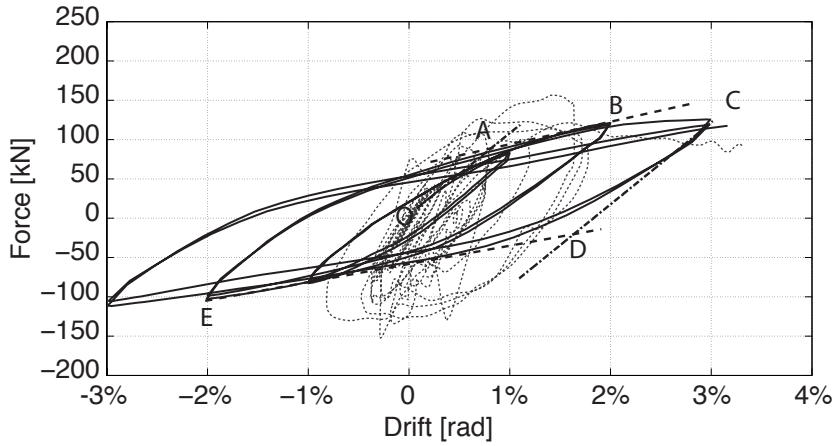


Figure 4.15. Response to small cycles

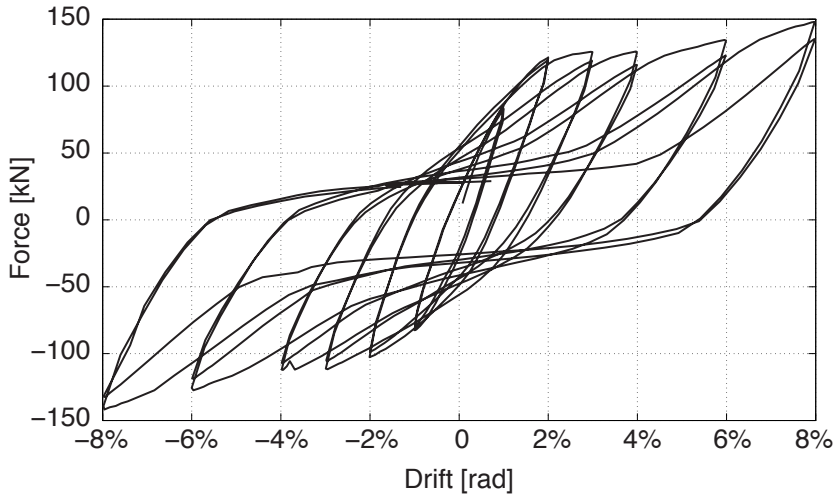


Figure 4.16. Response to large cycles

The equivalent viscous damping (Figure 4.17) remained unchanged for cycles of less than 2% drift angle. The first noticeable reduction in the equivalent damping appears on the first cycle to 3% drift angle. The losses is approximately 20% between consecutive cycles at the same amplitude. When these results are compared against the online test, both results show similar values for drift angles at the same amplitude (1% or 2%), although the online test results show higher values of damping. These values are associated to the undamaged state of the specimen.

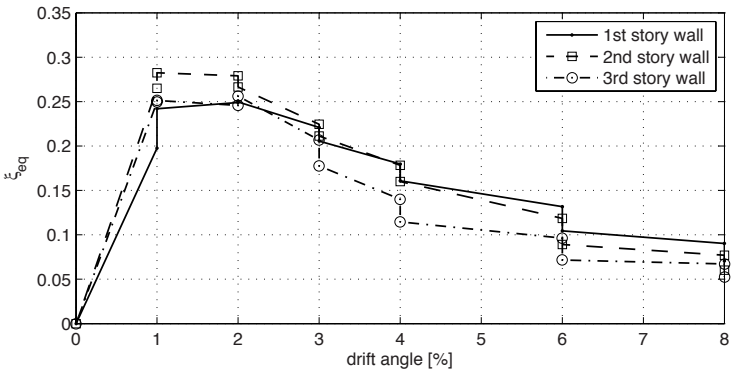


Figure 4.17: Equivalent viscous damping

### 4.4.3 Out-of-plane deformations

During the cyclic tests, all flexural links presented out-of-plane deformations, although the initiation took place at different drift angles. For the smaller cycles up to 3.0% drift angles, only the condition assessment zone (painted in white) sustained out-of-plane deformations (Figure 4.18 (a)). At 4.0% drift angle, pinching appeared in the restoring force, which matched the beginning of the buckling of the flexural links located outside the condition assessment zone (Figure 4.18 (b) shows the slit wall at 6% drift angle to make the buckling of the flexural links more evident). As the loading progressed through larger drift angles, the buckling extended to the exterior flexural links.

Chapter 5 will introduce the means that allow condition assessment capabilities to slit wall by means of the prediction of the buckling behavior of flexural links.

(a) Buckling at 3% drift angle (b) Buckling at 6% drift angle

Figure 4.18. Out-of-plane deformations

### 4.4.4 Damage observation

No damage was observed in the slit walls after the online test described in the previous section. During the cyclic tests, fractures were observed at the end of the slits only after the two largest amplitudes were imposed on the specimens, i.e., 6% and 8%, shown in Figure 4.19 (a) and (b), respectively. The fractures were caused by the tension-compression force pairs that take place at the ends of the slits as shown in Figure 4.19 (c). Although the fractures contribute to the strength deterioration, their overall effect is minimal when compared to the effect of the buckling of the flexural links.

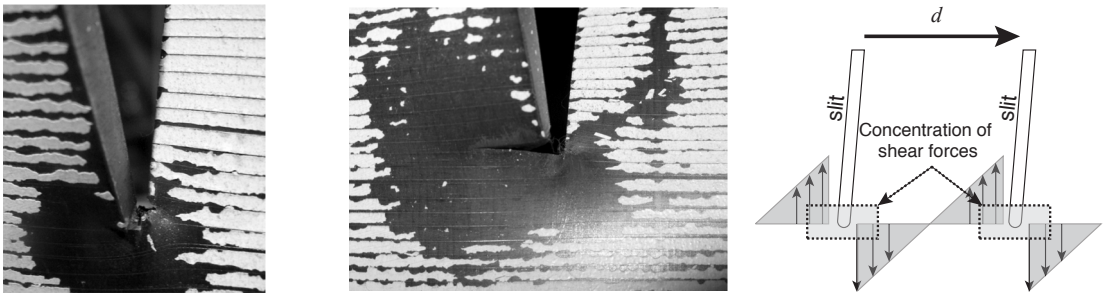


(a) Damage at 6% drift angle (b) Damage at 8% drift angle (c) Fracture mechanism

Figure 4.19. Fractures at the end of the slits

## 4.5 Summary and conclusions

In this chapter, the seismic simulation of a three-story steel frame with slit walls (SWs) was conducted using an online hybrid test system. The SWs feature an innovative slitting pattern to add condition assessment capabilities without reducing the energy dissipation characteristics of the SWs. The structure is divided into two substructures. The backup frame is treated numerically using OpenSees, while the span featuring the SW is an experimental substructure that is physically tested. Ground motion was imposed on the structure at two different magnitudes. After the online hybrid test was completed, the slit wall specimens were salvaged and further tested under cyclic load.

The major findings are summarized as follows:

(1) During the online test, all unequally slitted SW specimens sustained large ductility (ductility ratios above 3 for the Level 2 ground motions). The shear walls provided the structure with large stiffness and energy dissipation at small (0.47%) drift levels. Fat hysteresis loops without strength deterioration were obtained. Thus, unequally slitted shear walls retained the hysteretic characteristics of conventional slit designs.

(2) A nonlinear finite element analysis gave reasonable predictions of the elastic (within 70% of the experimental value) and post-yield behavior (within 85% of the experimental value) of the SW. The equivalent brace models used in the early prediction model, with properly adjusted strain-hardening properties, were able to accurately duplicate the response of the test structure in the online test (4% error in amplitude for the Level 2 ground motion).

(3) During the cyclic test, the slit walls showed a reduction of approximately 50% in stiffness and maximum strength when compared to the results from the online test. However, fat hysteresis loops were obtained for drift angles up to 3% with pinching only apparent after the second cycle to this amplitude. No deterioration of the maximum strength was observed, even drift angles of 8%

(4) Out-of-plane deformations of the flexural links were evident in both the online test, where the links intended for condition assessment buckled for drift angles of approximately 2%. The buckling of the flexural links in the online test did not translate into pinching for this test. In the cyclic test, the flexural links outside the condition assessment zone buckled for drift angles of 4%.

# REFERENCES


[1] M. Midorikawa, I. Okawa, M. Iiba, and M. Teshigawara, "Performance-based seismic design code for buildings in Japan," *Earthquake Engineering and Engineering Seismology*, vol. 4, 2003, pp. 15-25.

[2] Building Center of Japan, *The Building Standard Law of Japan*, Tokyo, Japan: Building Center of Japan, 2004.

[3] Architectural Institute of Japan, *Recommendation for Limit State Design of Steel Structures*, Tokyo, Japan: Architectural Institute of Japan, 1998.

[4] Architectural Institute of Japan, *Recommendation for Design of Connections in Steel Structures*, Tokyo, Japan: Architectural Institute of Japan, 2001.

[5] S. Mazzoni, F. McKenna, and G.L. Fenves, *OpenSees command language manual*, Berkeley, USA: Pacific Earthquake Engineering Research (PEER) Center, University of California, 2005.

[6] Nakashima M, *et al*. Feasibility of pseudo dynamic test using substructuring techniques. *Proceedings of 9th World Conference on Earthquake Engineering*, Tokyo, 1988, **4**: 47-52.

[7] Nakashima M, Kaminosono T, Ishida M, Ando K. Integration techniques for substructure pseudodynamic test. *Proceedings of 4th U.S. National Conference on Earthquake Engineering*, Palm Springs, CA, 1990; **2**: 515-524.

[8] S.N. Dermitzakis and S.A. Mahin, "Development of substructuring techniques for on-line computer controlled seismic performance testing," *Report No. UCB/EERC-85/04, EERC, UC Berkeley, CA*, 1985.

[9] Tsutsumi H, Sato K, Ando K. Substructure pseudo dynamic test with rotation control. *Proceedings of 4th U.S. National Conference on Earthquake Engineering*, Palm Springs, CA, 1990; **2**: 525-534.

[10] Ohi K, Lin X, Takanashi K. Sub-structure pseudo-dynamic test scheme suitable for bending-shear type flexible steel frames. *Journal of Structural and Construction Engineering*, Architectural Institute of Japan, 2001; **540**: 49-55 (in Japanese).

[11] P. Pan, M. Tada, and M. Nakashima, "Online hybrid test by internet linkage of distributed test-analysis domains," *Earthquake Engineering & Structural Dynamics*, vol. 34, 2005, pp. 1407 - 1425.

[12] T. Wang, J. McCormick, N. Yoshitake, P. Pan, Y. Murata, and M. Nakashima, "Collapse simulation of a four-story steel moment frame by a distributed online hybrid test," *Earthquake Engineering & Structural Dynamics*, vol. 37, 2008, pp. 955 – 974.

[13] M. Tada and P. Pan, "A modified operator splitting (OS) method for collaborative structural analysis (CSA)," *International Journal for Numerical Methods in Engineering*, vol. 72, 2007, pp. 376-396.

[14] A. Jacobsen, T. Hitaka, Y. Murata, J. McCormick, T. Wang, and M. Nakashima, "Condition Assessment Application of Steel Shear Walls with Slits," *Proceedings of the 14th World Conference on Earthquake Engineering*, Beijing, China: International Association for Earthquake Engineering, 2008.

# CHAPTER 5

# Buckling initiation as a means for condition assessment

## 5.1 Introduction

### 5.1.1 Background

Out-of-plane deformations are inherent to the behavior of slit walls. By introducing slits in the plate, global plate buckling is prevented by concentrating the out-of-plane deformations in the flexural links [1]. Following this premise, out-of-plane deformations of the flexural links were experienced during the online test [2], and it was noticed that thicker links buckled whereas the conventional design zone did not for the drift angles experienced during the online test (up to 3% story drift angles). In the cyclic tests that followed, the flexural links located in the conventional design zone buckled for drift angles above 4.0%. The difference in the buckling drift angle between these two types of links presents the alternative of using the buckling behavior of flexural links as an application for condition assessment.

### 5.1.2 Organization

This chapter is divided in two part. In the first part the inclusion of condition assessment capabilities by following the buckling behavior of flexural links is proposed. Two types of flexural links, based on the independent behavior of flexural links, are introduced to achieve this objective: (1) "Monitoring links" that develop inelastic buckling at predetermined drift angles and (2) "Cushion links" that prevent the spreading of strains in between the monitoring links.

In the second part of this chapter, an experimental verification of the design proposed in the previous part is carried out on scaled specimens. The hysteretic performance, as well as the monitoring capabilities of the new design of slit walls are evaluated.

## 5.2 Independent flexural links

### 5.2.1 Concept

The link rotation angle is defined as the angle generated by out-of-plane buckling of the flexural link measured at the mid-height of the flexural link. In this chapter the link rotation angle is used as a parameter for the evaluation of damage sustained by a slit wall with unequal slitting. The link rotation angle can either be used independently, or in combination with the method of strain tracing that was introduced in the first section of Chapter 3.

As it was demonstrated in Chapter 3, flexural links with different geometries can be combined in a single SW to achieve different properties of strength and stiffness along the wall without loss of damping capacity. The variation of these properties in each of the flexural links determines the lateral deformation at which a given flexural link develops plastic hinges at the ends (this is the concept behind the estimation of the maximum strength of a slit wall). In the same manner these properties will determine at which lateral deformations the flexural links will develop inelastic buckling [3]. As a general rule, wider flexural links concentrate higher strains than thinner flexural links; in the same manner a wider flexural link would buckle at a smaller drift angle than a thinner flexural links, granted that the height of both flexural links is the same. Therefore it is possible to adjust the development of inelastic buckling in the flexural links for a specific drift angle e.g., 1.0% or 2.0% by taking into consideration these characteristics at the design stage.

After the earthquake event, the maximum drift angle to which the slit wall was subjected can be estimated by inspecting the residual link rotation angles. However, in the tests presented in Chapter 4, links with different widths developed buckling for the same drift angles when they were placed side by side. Figure 5.1 shows the strain patterns (obtained from an associated finite element model) developed at a drift angle of 1% in the third story slit wall specimen tested in the online test introduced in Chapter 4. This drift angle corresponds to the initiation of the out-of-plane buckling of the flexural links located at the center of the plate in the condition assessment zone. This slit wall was intentionally designed to propagate the strains to the maximum possible area.

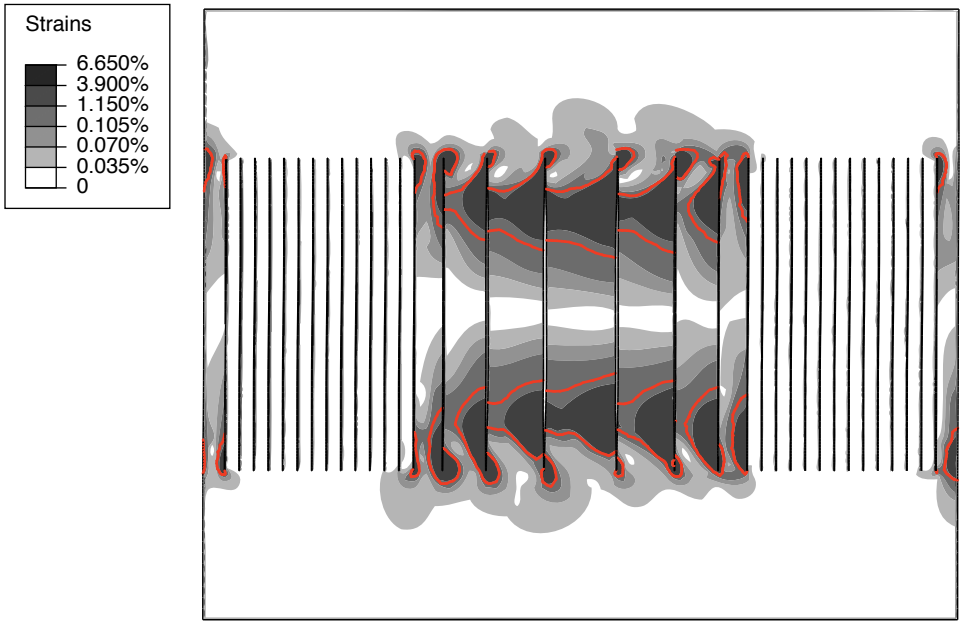


Figure 5.1. Selected strain levels for the third story slit wall at 1.0% drift angle

The downside of extending the strain areas is that the behavior of each flexural link is influenced by the behavior of its adjacent links, i.e. the strains propagated from a wider flexural link will invariable reduce the drift angle at which its neighboring links will develop plastic hinges. This figure also provides an alternative to overcome the effects of the propagation of the strain through

the plate: the flexural links located in the conventional design zone stop the propagation of strain. Although not shown in the picture, the strains developed in the conventional design zone remain concentrated in each of the flexural links and do not expand to their neighboring links.

Based on the behavior observed in these specimens it was concluded that strain spreading to adjacent links can be prevented by introducing thinner links between the wider ones. Therefore two different types of flexural links are introduced in this chapter: the flexural links intended for monitoring purposes are referred as "monitoring links" and those intended for the prevention of strain propagation between monitoring links are known as "cushion links".

### 5.2.2 Cushion Links

As observed in the bottom left corner of the strains shown in Figure 5.1, spreading of the strains outside the wider flexural links might extend beyond the smaller flexural links immediately next to it. Thus, several cushion links might be needed to isolate a monitoring link. To ensure the independence in the behavior of the monitoring links, a cluster of cushion links arranged side-by-side is used to separate the monitoring links.

Cushion links are intended to prevent the spreading of the strains generated by monitoring links. To achieve this, the strains generated at the end of the cushion links should be significantly smaller than those generated by the monitoring links.

The monitoring range encompasses the drift angles at which the monitoring links are expected to develop out-of-plane buckling. In other words, if the monitoring links were designed to detect drift angles of 0.5, 1.0 and 2.0%, the monitoring range would extend up to 2% drift angles. Hitaka and Matsui [1] observed that for flexural links with aspect ratios ($l/b$) larger than 3 and slenderness rations ($b/t$) of less than 10 the flexural links remained in-plane for drift angles up to 2.5%. The basic design of cushion links is based on this observation.

A parametric analysis was conducted in a finite element software [4] to establish the size of the cushion link cluster as well as the effects of the introduction of cushion links. For the analysis six simplified models of a slit wall were constructed. The baseline model consists of a 6 mm thick steel plate with dimensions of 1050 mm in height and 485 mm in width (Figure 5.2 on the left). Four slits are cut in the wall, creating a flexural link at the center with a width of 175 mm, and two flexural links on the sides with widths of 130 mm. The difference in widths of the flexural links will insure that the drift angle for which the links develop out-of-plane buckling is sufficiently different to function as an example. The flexural links in the baseline model have aspect ratios ($l/b$) of 3.65 and 4.92 for the 175 mm wide link and 130 mm wide link, respectively, which are compliant with the requirements stated above. The slenderness ratios ($b/t$) were 29.6 and 21.6 and did not comply with the slenderness required for in-plane behavior. The model was subjected to cyclic loading consisting of two cycles to a 0.5% drift angle followed by two cycles to 1.0%. The loading is intended to generate buckling in the wider flexural link for the smaller cycles (0.5% drift angle) without inducing buckling in the narrower flexural links, which would later buckle for the larger cycles to 1.0% drift angle.

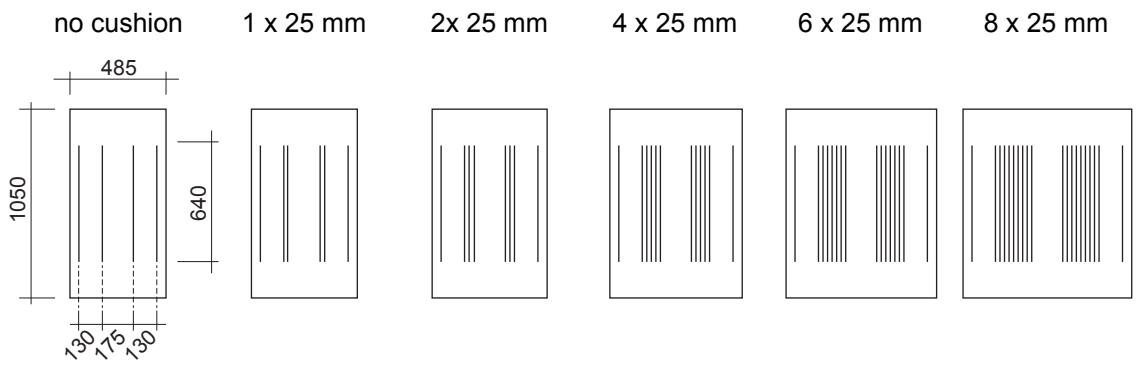


Figure 5.2. Models used for cushion parametric analysis (unit: mm)

The other models (see Figure 5.2) considered in the parametric analysis introduce a variable number of 25 mm wide cushion links between the flexural links to demonstrate the insulating effect provided by the introduction of cushion links. The parameter considered is the number of cushion links introduced between the wider flexural links, thus the models considered the introduction of clusters of one, two, four, six and eight cushion links.

Figure 5.3 shows the results obtained from the parametric analysis, tabulated according to the model they refer to, and the results presented in them. The first row in Figure 5.3 shows the strains generated at the maximum amplitude in the second cycle to 0.5% drift angle of the wall, the box in dashed line emphasizes the strains at the end of the flexural links. It can be seen in the boxes that the strains propagated to the neighboring flexural links. The introduction of a single cushion link does not seem to have any deterrent effect on the propagation of the strains from the central flexural link, but as the number of cushion links increased the strain concentrations at the end of the flexural links began behaving independently from each other. Finally, for the model with the largest number of cushion links the strain zones are clearly separated.

The second row of pictures in Figure 5.3 shows the residual strains after the cycles to 0.5% drift angle. On the base-line model the residual strains generated in the thinner monitoring links (130 mm in width in Figure 5.2) present an asymmetrical shape with respect to their center vertical axis. An asymmetrical distribution of the residual strains undesirable, since it facilitates the initiation of buckling. As the number of cushion links increased (moving towards the right in the figure) the strains in the thinner monitoring link became more uniform while the strains in the center monitoring link remained asymmetrical (as the flexural link had already buckled).

The residual out-of-plane deformations are plotted in the third row of pictures in Figure 5.3. In the base-line model the plate buckling can be observed dividing the plate diagonally, pulling the top-left half of the plate forward and pushing the bottom-right half of the plate towards the back. The lateral-torsional buckling is evident in the center link. The outer monitoring links do not show signs of lateral-torsional buckling in this scale, but the strain concentrations shown in the row above indicate that buckling will invariably be a trigger in these links even if the following cycles are of smaller amplitudes.

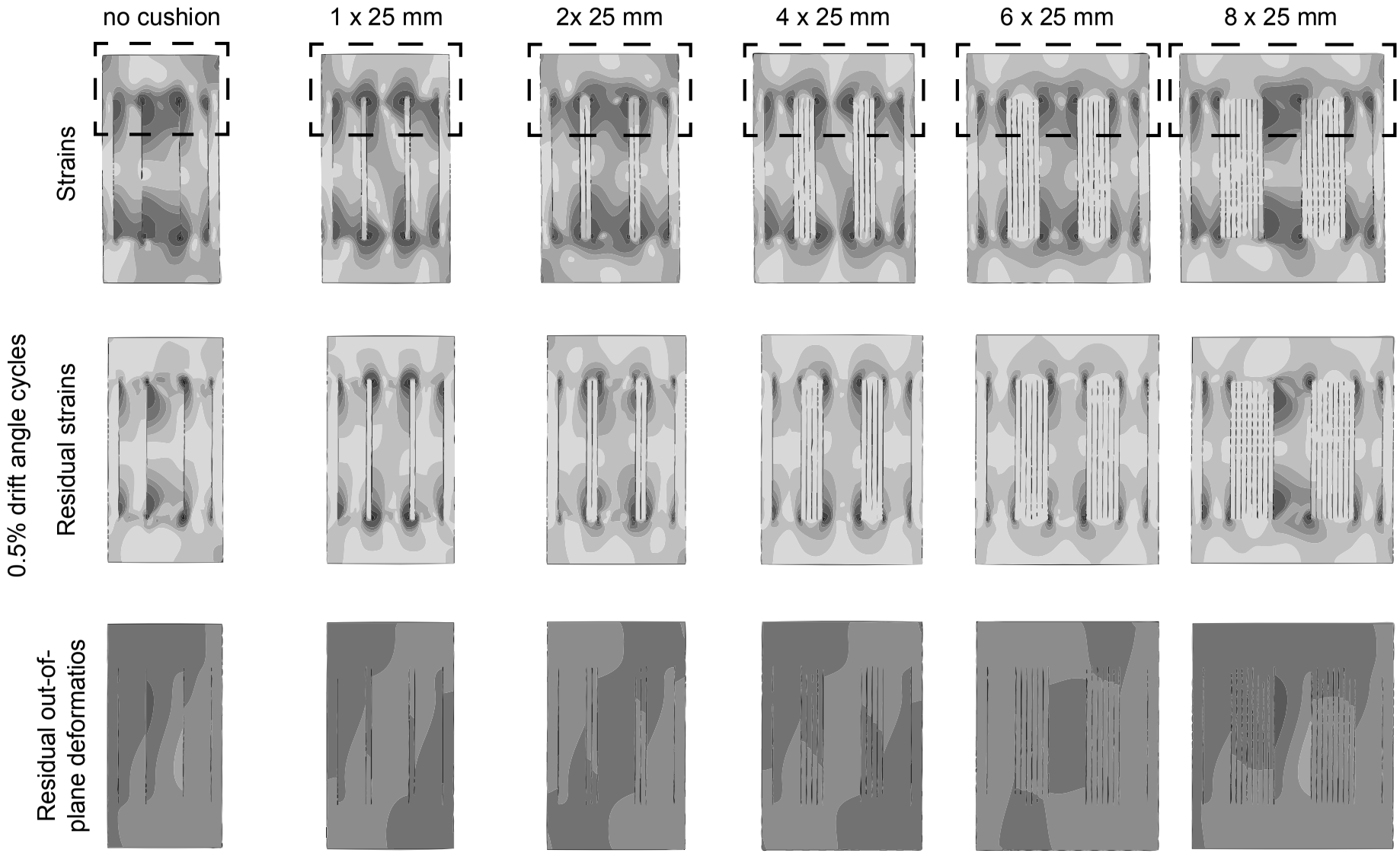


Figure 5.3. Results of parametric model on cushion links: (a) Strain distribution at 0.5% drift angle, (b) residual strains after two cycles to 0.5% drift angle, (c) residual out of plane deformations after two cycles to 0.5% drift angle

For the following cycles to 1% drift angles (see Figure 5.4), the spreading of the strains changed as the number of cushion links increased. In the base-line model the maximum strains spread towards the unslitted section of the plate, whereas on the model with two cushion links the strain concentrations are displaced towards the inside of the flexural links. For those walls with more than two cushion links the strains follow a more clear asymmetrical pattern that agrees with the out-of-plane deformations of the flexural links. The pictures at the bottom row in Figure 5.4 show the residual out-of-plane deformations after the cycles to 1.0% drift angles, in all cases the deformations are clear on both the wider (175 mm) and narrower (130 mm) monitoring links. The out-of-plane deformation in the wider monitoring link increase at this amplitude.

In conclusion, the effect of the cushion links can be appreciated in those models with 6 and 8 cushion links. The cluster of cushion links in these two models have a total width of 150 and 200 mm, respectively. The minimum cluster width (150 mm) amounts to approximately the average of the widths of the monitoring links ((130+175)/2=152.5 $mm$) that surround the cluster. Therefore, for design purposes, the width of the cushion cluster should be equal to this value.

### 5.2.3 Monitoring links

In the previous section the application of cushion links was demonstrated as a means to insulate the behavior of those flexural links whose out-of-plane deformations are used for monitoring purposes. In this section the buckling behavior of the monitoring links is established.

Buckling in the flexural links occurs after the formation of plastic hinges at the ends. Thus, it can be construed as inelastic buckling. Inelastic buckling is difficult to predict using elastic buckling equations [5]. In Chapter 3 a parametric numerical analysis was conducted under cyclic loading to establish the buckling drift angles of flexural links of different widths. Two loading protocols were considered for the analysis: 1) a single cycle per amplitude and 2) a double cycle per amplitude. These two protocols reflect the effect that the loading history has on the buckling initiation.

The drift angles at which the links buckled were obtained by visual inspection of the analysis results. Initiation of the buckling by visual inspection was defined by the buckling shape, as the link sustains double curvature deformation, i.e., the upper left of the link rises out-of-plane whereas, the lower left dips. The drift angle for which each flexural link buckles are summarized in Table 5.1. As it can be noted from the data presented in the table, some of the link widths buckle at different loading instances. This phenomenon requires further study on the effect of the loading history in the buckling behavior of flexural links.

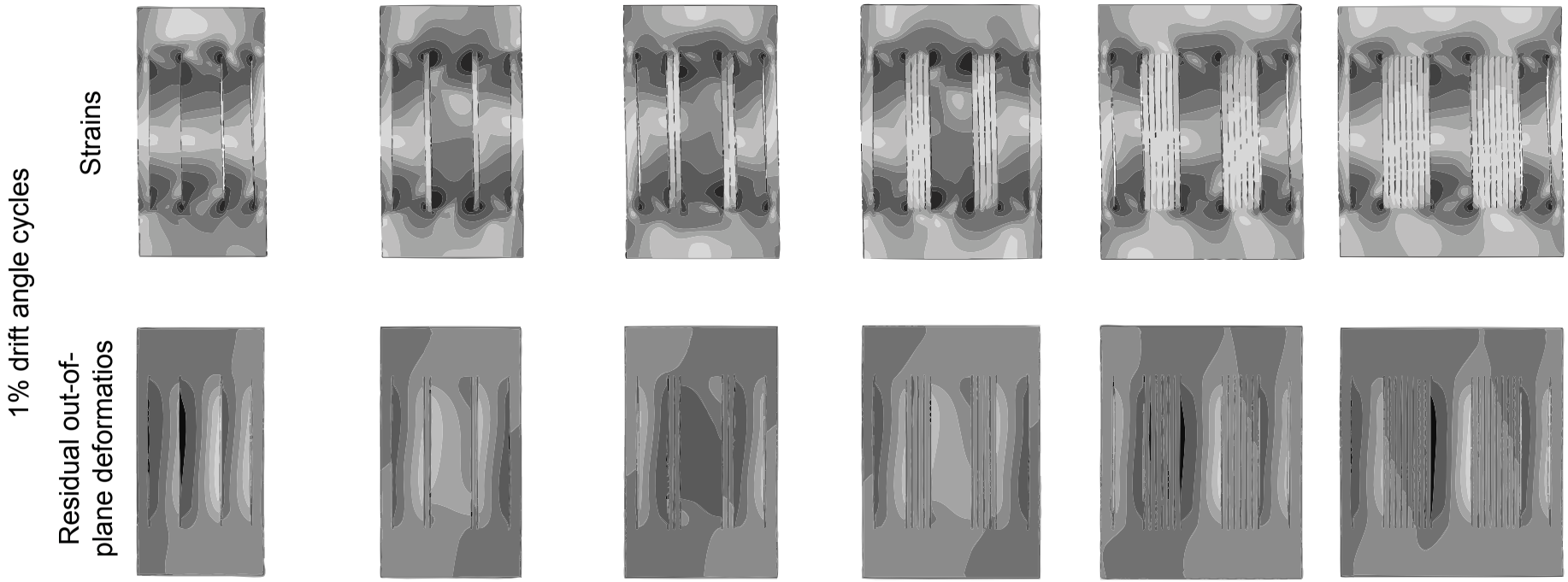


Figure 5.4. Results of parametric model on cushion links: (a) Strain distribution at 1.0% drift angle, (b) residual out of plane deformations after two cycles to 1.0% drift angle

Table 5.1. Drift angle and buckle initiation relationship

| Drift angle | Aspect ratio $(l/b)$ | |
|---|---|---|
| | Single cycle | Double cycle |
| 0.5% | 3.2 – 3.8 | 3.2 – 4.6 |
| 1.0% | 3.9 – 5.8 | 4.7 – 6.7 |
| 2.0% | 6.0 – 8.0 | 7.1 – 9.1 |
| 3.0% | 8.5 – 9.8 | 9.8 – 10.6 |
| More than 3.0% | 10.5 and less | 11.6 and less |

### 5.2.4 Parametric study on the effect of loading history in buckling initiation

A parametric study is conducted to establish the effect that the loading history has on the buckling of the flexural links. The parametric study consists of five models with aspect ratios equal to: 3.2, 4.7, 7.5, 8.5 and 18.2. The models ( similar to the one shown in Figure 5.2 on the left) were subjected to several cyclic loading protocols, each of which had a different number of cycles per amplitude. The protocols consisted of incremental cycles of 0.5%, 1.0%, 1.5%, 2.0%, and 3.0%, the number of cycles in each protocol were: 1, 2, 3, 4, 5 and 10.

Figure 5.5 shows some selected results from the parametric analysis. The plots show the residual out-of-plane deformations after each cycle. In order to readily compare the results, the out-of-plane deformations are presented as the rotation angles of the flexural links, measured at the mid-height of the specimen. The figure clearly indicates that the amount of buckling differs between a single cycle and multiple cycles per amplitude. Nonetheless, it can be appreciated that the initiation of buckling takes place for the same drift angle, i.e., 0.5% drift angle for the flexural link with *l/b=3.2*, 1.0% drift for links with *l/b=4.7*, and 1.5% for link with *l/b=7.5*. For the models subjected to 10 cycle loading, it can be noted that the large number of cycles increased the out of plane deformation obtained for the same amplitude, but it does not seem to influence the amount of out-of-plane deformation that is achieved for larger cycles. This can be seen as the increase in deformations in the 10 cycle curve at 1.5% drift angle for any of the models presented, however when the amplitude increases to 2.0%, the out-of-plane deformation achieved is very similar to that obtained when loading only to 2 cycles.

In general, the number of cycles to smaller amplitudes has little influence on the buckling angle achieved for larger amplitudes. Moreover, additional cycles to the same amplitude increase the out-of-plane deformations, but does not hasten the initiation of buckling. Finally, the loading to a single cycle stands out as the only case that does not follow the trend shown by the other loading protocols.

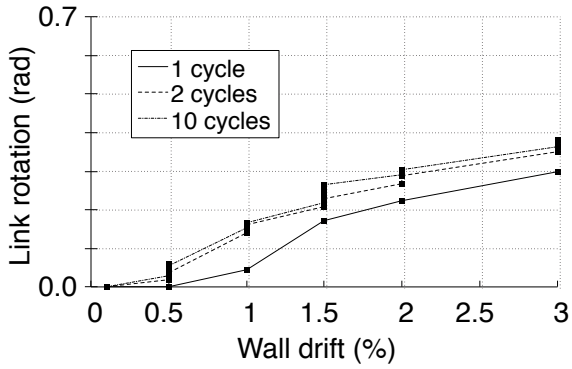


(a) Aspect ratio = 3.2

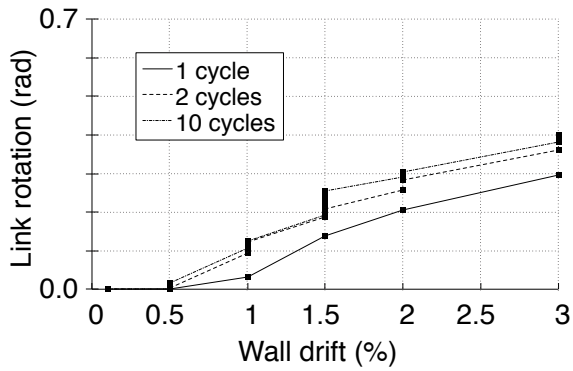


(b) Aspect ratio = 4.7

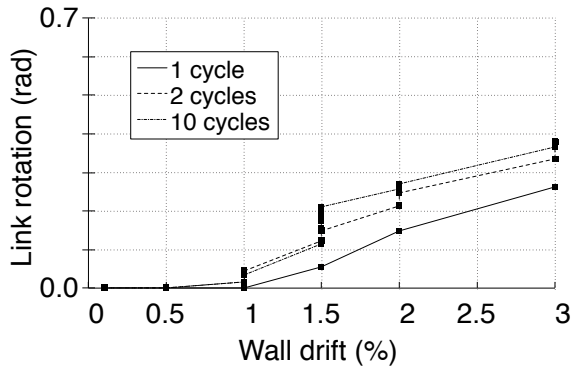


(c) Aspect ratio = 7.5

Figure 5.5. Effect of cyclic loading on buckling behavior

## 5.3 Test Program

### 5.3.1 Specimen design

Based on the parametric analysis described in the previous section, two scaled specimens were designed to verify the application of out-of-plane buckling for condition assessment. Specimen 1 (Figure 5.6 on the left) had monitoring links widths of 200, 135 and 85 mm, and Specimen 2 (Figure 5.6 on the right) had monitoring links widths of 170, 110 and 75 mm. Buckling of the monitoring links, determined by visual inspection of the finite element model, was expected to initiate for the values summarized in Table 5.2. The plate size was similar to the larger specimens from the online test presented in Chapter 4. The slit length was 640 mm for both specimens. The width of cushion links was set to 25 mm and 35 mm for Specimen 1, with the wider cushion links near the center of the plate. For Specimen 2, all cushion links were 25 mm wide. In addition, in Specimen 2 a single 50 mm wide link was added to the center of each cushion link cluster. The idea behind the use of this 50 mm link was to reduce the effect of the vertical forces caused by overturning moment of the SW (see Figure 5.7 (a)), thus providing some resistance against Euler buckling of the cushion link cluster (see Figure 5.7 (b)). The steel used for the specimens was mild steel, SS400. The average mechanical properties, obtained from three associated coupon tests, are summarized in Table 5.3.

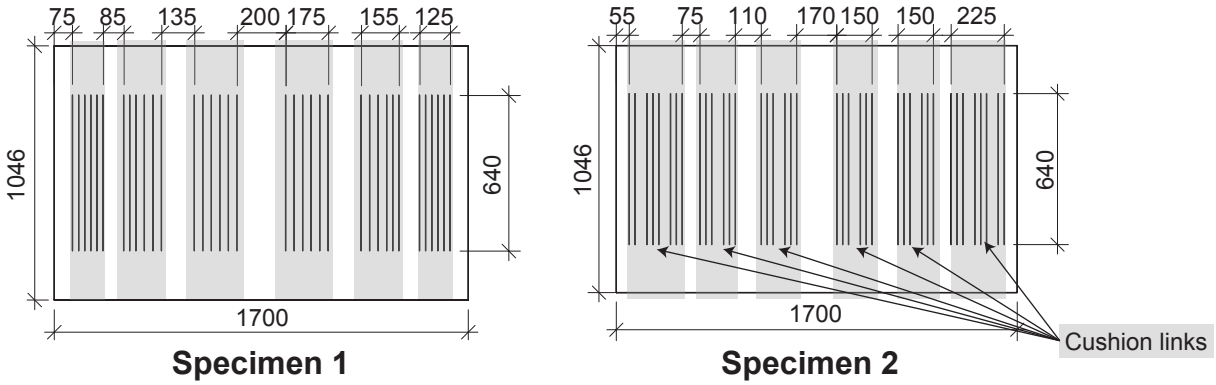


Figure 5.6. Test specimens

Table 5.2. Predicted buckling drift angle for test specimens

| Rotation angle | Specimen 1 | Specimen 2 |
|---|---|---|
| 0.5% | 200 mm-link | 170 mm-link |
| 1.0% | 135 mm-link | None |
| 2.0% | 85 mm-link | 110 mm-link |
| 3.0% | None | 75 mm-link |

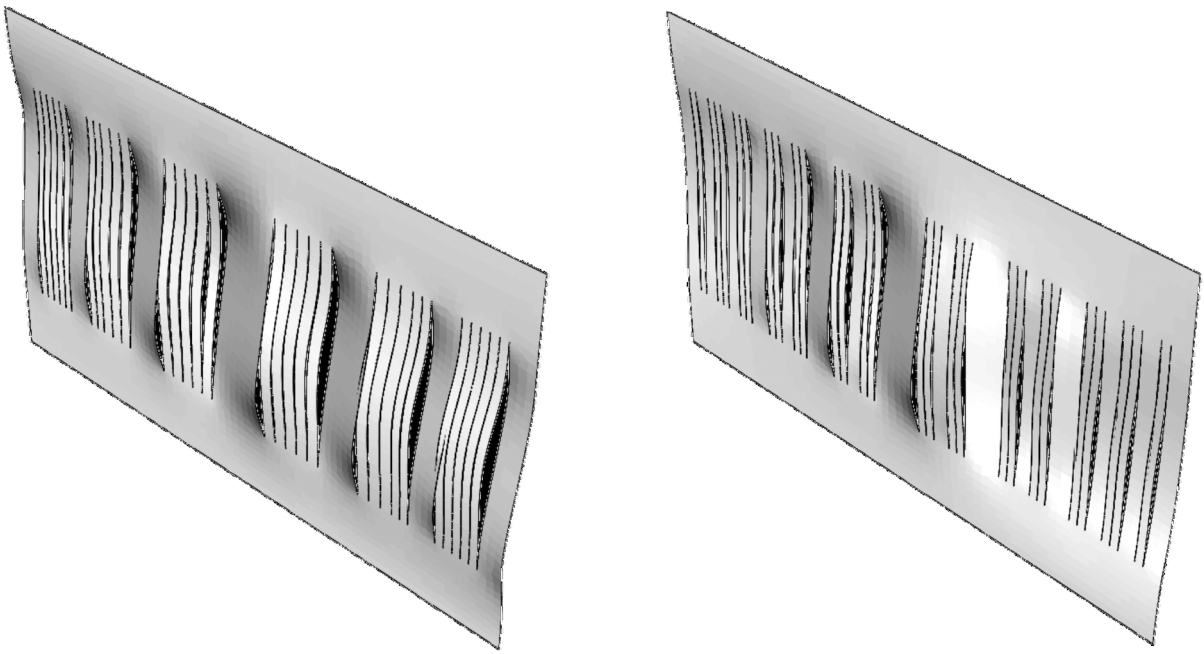

(a) Euler buckling of cushion links in Specimen 1

(b) Wider link prevents other links from buckling in Specimen 2

Figure 5.7. Effectiveness of 50 mm link to reduce Euler buckling of cushion links

Table 5.3. Material properties

| Steel Type | Young modulus [MPa] | Yield strength [MPa] | Maximum strength [MPa] | Yield ratio |
|---|---|---|---|---|
| SS400 | 189746 | 362 | 445 | 0.82 |

### 5.3.2 Test setup and loading program

The test specimen was placed in the loading frame shown in Figure 5.8. The foundation beam was fixed to the strong beam of the laboratory. Pinned columns ensured that the rotation at the top of the specimen was restrained. The loading was applied using a 1.5 MN static jack attached to the top reaction beam. This beam was also restrained by rollers in the out of plane direction. A displacement-controlled cyclic load was applied quasi-statically in the horizontal direction. The displacement was expressed in term of drift angle, defined as the horizontal displacement at the top of the slit wall relative to the height of the slit wall (1050 mm). Loading to drift angles of 0.1%, 0.5%, 1%, 2%, 3%, 4%, 6%, and 8% were adopted. Two cycles were performed at each drift angle up to the cycle to 4% drift. A single cycle was adopted for the last two amplitudes. The test was terminated when the drift angle reached 0.08 rad and then the jack was returned to the center position.

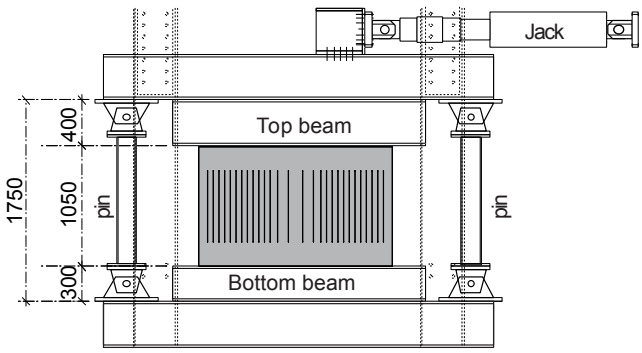


Figure 5.8. Elevation of the loading system (unit: mm)

### 5.3.3 Test Results

**Hysteretic characteristics**

The basic hysteretic characteristics of the two specimens tested in this series are presented in Table 5.4. The stiffness obtained from the test results show a good correlation with the predictions obtained with the analytical formulation developed in Chapter 3. However, the specimens developed a larger maximum strength than the equations predicted, with error of 16% and 25% for Specimen 1 and Specimen 2, respectively.

Table 5.4. Comparison in stiffness and strength between the prototype and test

| | Specimen 1 | | Specimen 2 | |
|---|---|---|---|---|
| | Experiment | Equation 3.9 | Experiment | Equation 3.13 |
| K [kN/mm] | 22.7 | 21.7 | 20.7 | 17.0 |
| Fy [kN] | 176.2 | 147.6 | 160.1 | 120.6 |

The hysteresis results for this series of tests are presented in Figure 5.9. The specimens tested in this series of tests presented a slightly different behavior when compared to those tested in Chapter

4. These specimens were characterized by a larger initial stiffness, and the maximum strength remained mostly constant throughout the loading, as opposed to the large post-yield stiffness of the previous specimens. Also for this series, the spindle shape of the curves became pronounced at earlier drift angles (3%) than those presented in the previous chapter. This was caused by the larger aspect ratios used to achieve out-of-plane buckling at early drift angles.

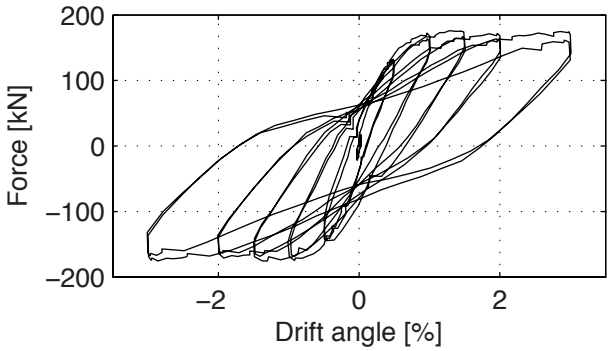


(a) Specimen 1 – small cycles

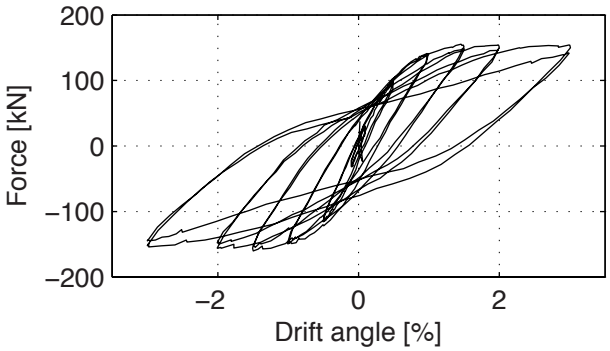


(b) Specimen 2 – small cycles

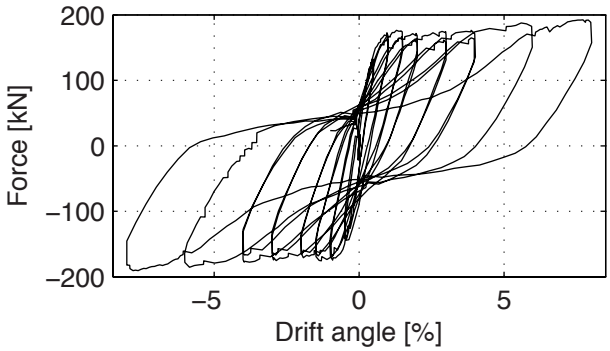


(c) Specimen 1 – large cycles

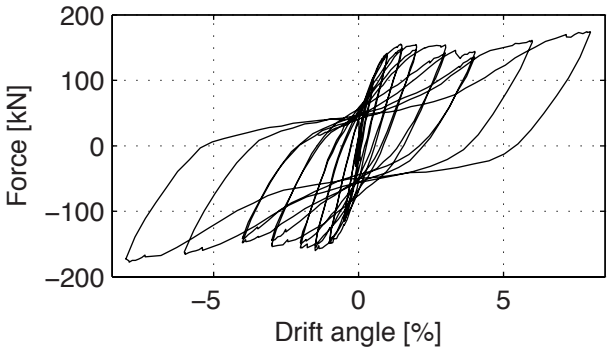


(d) Specimen 2 – large cycles

Figure 5.9. Test Results

A numerical FEM study on Specimen 1 was conducted in an attempt to replicate the results obtained from the test. The results obtained from the FEM analysis (based on the guidelines established in Chapter 3) did not replicate the results from the experiment accurately, in particular the maximum strength and unloading stiffness. After an examination of the boundary conditions of the analysis and the experiment, it was noticed that the top beam of the experimental setup moved in the vertical direction according to the cosine of the lateral drift angle. This movement was caused by the pins installed to prevent the top boundary of the wall from rotating. When these deformations are imposed on the FEM model the hysteretic curve presented in Figure 5.10 in solid line is obtained. For comparison the experimental result is presented in dotted line. In this case, the analysis reproduces the maximum strength and the initial stiffness of the test accurately. Unfortunately, the experimental behavior in the unloading stiffness could not be reproduced in the analysis.

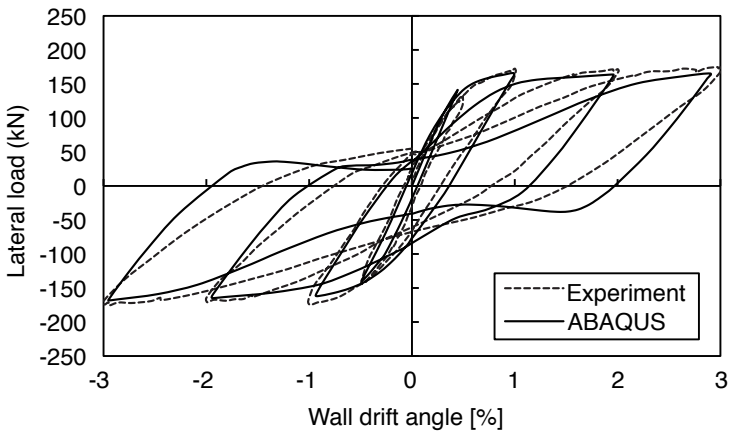


Figure 5.10. Replication of test results by FEM model

**Damping capacity**

Figure 5.11 shows the equivalent viscous damping coefficients calculated from the test data. Both specimens show a reduction of about 20% between consecutive cycles at the same amplitude, this drop is associated with the increase of out-of-plane of buckling of the flexural links. The damping coefficient of Specimen 2 is larger than that of Specimen 1 throughout the loading, although for drift angles beyond 4% the reduction that takes place on the second cycle seems to level the damping coefficients for both specimens. A possible explanation for the larger damping observed in Specimen 2 is that this specimen was design to develop buckling of the monitoring links later than in Specimen 1, i.e., Specimen 2 was expected to develop buckling for drift angles of 0.5%, 2%, and 3% whereas Specimen 1 was expected to develop buckling for drift angles of 0.5%, 1%, and 2%. It is also notable that the 50 mm cushion links had no effect on the damping behavior. This was probably caused by the boundary conditions in the experimental setup: the pinned columns restricted the rotation of the ends of the specimen, however the pinned columns also introduced a fixed vertical deformation on the specimens.

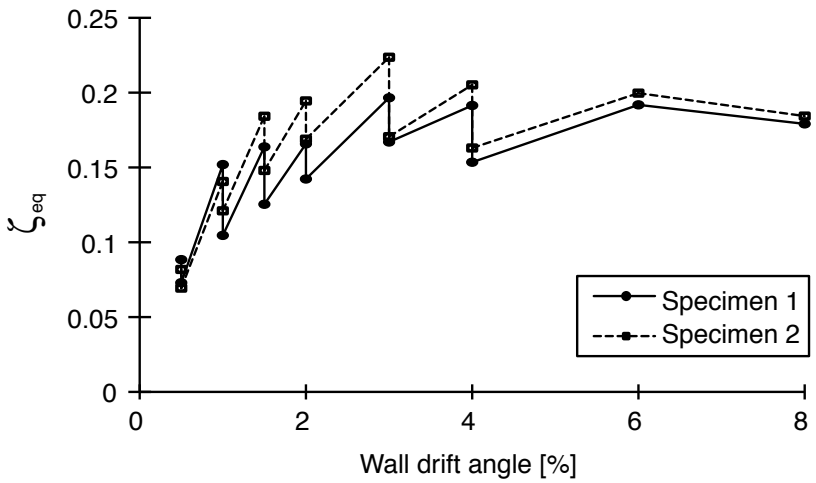


Figure 5.11. Damping capacity

### 5.3.4 Performance of buckling initiation for condition assessment

Damage evaluation by visual inspection of the buckling of the flexural links was implemented

for both specimens. Pictures of Specimen 1 at the end of each first cycle are presented in Figure 5.12. In Figure 5.12(a) and (b), the 200 mm link (*l/b*=3.2) rises out-of-plane in the upper left of the link and the lower right dips, as evidence of initiation of buckling caused by the double curvature deformation of the flexural link. In Figure 5.12(c), the buckling of two 135 mm links (*l/b*=4.7) is clearly visible. At this instance, the 85 mm links (*l/b*=7.5) looked slightly bent, but the buckling shape did not correspond to the inelastic buckling intended for condition assessment. Compression due to vertical forces as a result of the overturning moment caused this bending. In the cycle to 1.5% drift, one of the 85 mm links appeared to buckle, but when the load was released at the end of the cycle, it returned to the plane of the wall, thus no residual buckling was observed for the cycle to 1.5% drift angle. In Figure 5.12(d), all of the monitoring links have developed buckling. Moreover, after inelastic buckling took place at the designated drift angle, residual out-of-plane deformations remained clearly visible. Evidence of this can be found in the pictures, as they were taken after the lateral load was released.


(a) After 0.5% drift

(b) Close-up after 0.5%

(c) After 1.0% drift

(d) After 2.0% drift

Figure 5.12. Out-of-plane buckling in the monitoring links of Specimen 1 after each cycle

In an attempt to provide a more accurate measurement of the out-of-plane displacements of three of the monitoring links, two wires were placed at the right and left of the center of each link through a stud that was attached at the center of the link. A transducer was connected to the other end of the wires, and the transducers were fixed on a steel frame behind the SW. Each link rotation angle was calculated by using the data obtained from these transducers. Figure 5.13 shows the link rotation angles of Specimens 1 and 2. The markers show the predicted wall drift angle. The 200 and 135 mm links rotation angles prove that visual inspection was reasonable as a rapid increment of the

rotation was observed at the predicted rotations. However, such correlation was not observed for all flexural links.

It was observed that the buckling deformation was concentrated especially on the slit ends, and the link rotation angles preceded the overall buckling. It is speculated that the link rotation angle measured in the test may not be the best indicator for the out-of-plane deformation detected visually. In the future, the out-of-plane deformation should be measured near the slit ends to further explore the correlation between visual inspection and measured deformations.

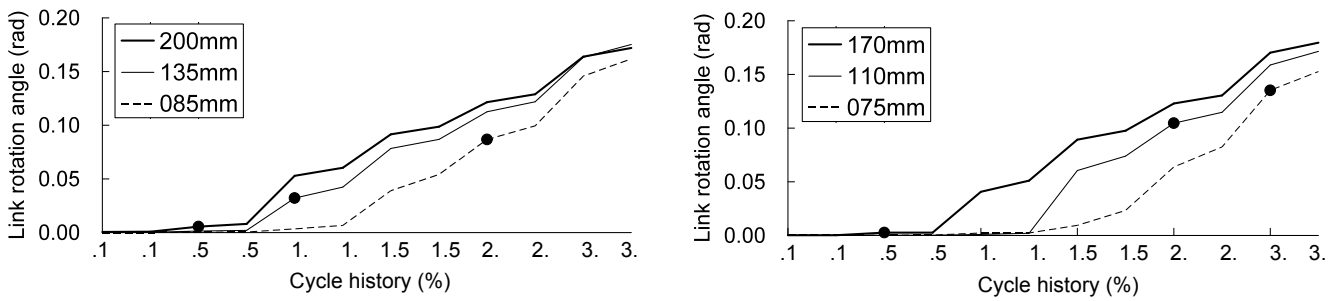


(a) Specimen 1 (b) Specimen 2

Figure 5.13. Measured out-of-plane deformations

## 5.4 Conclusions

This chapter presented an innovative application of slit walls for condition assessment. In this application inelastic buckling was predicted and traced to indicate different levels of the maximum story drift obtained during the loading. Two types of flexural links were introduced: (1) "cushion links", whose purpose was to act as buffers against the propagation of strains throughout the wall, and (2) "monitoring links" whose purpose was to develop out-of-plane buckling after specific lateral drift angles had been achieved. An experimental verification was carried out on two scaled specimens designed to develop out-of-plane deformations at drift angles of 0.5%, 1%, 2%, and 3%. The major findings are summarized as follows:

(1) The buckling behavior of flexural links due to lateral deformations can be predicted by means of finite element analysis with an accuracy of 0.5% in between drift levels. Condition assessment capabilities can be achieved based on the buckling behavior of flexural links.

(2) The spreading of strain in between neighboring monitoring links can be avoided by the inclusion of clusters of cushion links. The width of the cushion cluster should be at least equal to the average width of the monitoring links that the cluster separates. Furthermore, the aspect ratio of the cushion links should be larger than 10 to insure low strain concentrations at the end of the links.

(3) The slit distribution for condition assessment presented in this chapter does not deteriorate the hysteretic performance of the slit wall as a damper device. Damping coefficients up to 0.2 were obtained for drift angles of up to 4.0%. For very large lateral deformations (up to 8% drift angle) the damping coefficient remain above 0.15.

(4) Visual inspection proved to be a fast and accurate method to identify the initiation of buckling behavior in the monitoring links. In the experimental results, visual inspection proved accurate to detect lateral deformations of 0.5%, 1.0% and 2.0%. However, the results obtained from visual inspection did not fully match those obtained from measured out of plane deformations by displacement transducers.

# REFERENCES


[1] T. Hitaka and C. Matsui, "Experimental study on steel shear wall with slits," *J. Struct. Eng.-ASCE*, vol. 129, 2003, pp. 586 - 595.

[2] Jacobsen, A., Hitaka, T., and Nakashima, M., "Online Test of Building Frame with Slit-Wall Dampers Capable of Condition Assessment", *Journal of Constructional Steel Research* **66**, 2010, pp.1320 – 1329

[3] Timoshenko, S., and Gere, J. M. (1961). *Theory of elastic stability*, 2nd Ed., McGraw-Hill, New York, 239–250.

[4] Abaqus Inc., "ABAQUS Version 6.7 User's Manual," *http://www.abaqus.com*, 2007.

[5] Trahair NS. Flexural-torsional buckling of structures. London: E&FN SPON-Chapman and Hall, 1993.

# CHAPTER 6

# Paint as a means for condition assessment

## 6.1 Introduction

### 6.1.1 Background

The study of paint is commonly associated to rheology and chemical engineering, and it is mostly restricted to areas such as coloring, resistance to weathering, toxicity, and so on. Only a very limited number of studies have been carried out in order to ascertain the mechanical characteristics of paint, and most of those studies focus on improving characteristics such as elasticity or durability. Although these studies provide a valuable reference [1]-[3], their objectives differ from that of this study.

### 6.1.2 Organization

This chapter is divided in two parts: The first part focuses on the search for a suitable paint compound that allows for the recording of the spreading of strains throughout a steel plate. This study is carried out in three phases:

(1) A parametric study on different types of commercially available paints, in which several compounds were tested under monotonic load. This stage provides a number of compound candidates that flake when subjected to strain.

(2) A parametric study on the effectiveness of fillers and gridlines. Fillers and gridlines modify the composition and geometry of the film of paint. This stage defines the final compound to be used for the second part of the study.

(3) A study on the stability of the behavior of the compound selected, in which several identical coupons are tested.

The second part examines the performance of the spreading of the flaking of the paint compound under experimental conditions. The paint compound selected in the previous part was applied on the surface of three reduced-scale slit wall specimens. The flaking of the paint was recorded throughout the loading of the specimens.

## 6.2 Coupon research on paint

### 6.2.1 Introduction

A reliable method is needed to achieve condition assessment capabilities with slit walls. The

premise that the patterns defined in slit walls by different levels of strains represent an accurate indicator of the lateral drift angle was demonstrated in Chapter 3. In practice, the problem of recording the spreading of the maximum strains through the full extent of a shear wall has not been solved for the application required in this study. Several alternative methods have been proposed, e.g. ultrasound [4], x-rays [5], [6], brittle coatings [7]-[9], and nanotube films [10]. These methods provide accurate measurements of the levels of strains but lack crucial characteristics such as the possibility of covering large surfaces and resistance to corrosion (strain gauges) or require expensive equipment and trained operators (ultrasound and x-rays fall into this category). A brief summary of these non-destructive techniques for measuring strains is presented in Table 6.1.

Table 6.1. Summary of non-destructive strain measurement techniques

| | **Ultrasound (LCR waves)** | **X-ray-neutron diffraction** | **Brittle Coat** | **Nanotube films** |
|---|---|---|---|---|
| **Description** | Ultrasonic techniques rely on the variations in time of flight difference of ultrasonic waves, which can be related to the stress state through third order elastic constants of the material. | Measure lattice strains by studying the variations in the interplanar spacing of the polycrystalline material. The X-ray diffraction technique measures the strain on the surface of the material, while the neutron diffraction method measures the strain within a volume of the sample. | Thin brittle layers are deposited on the studied surface. Under loading conditions the brittle coating will fracture in response to the surface strain beneath it. The coating indicates the direction and magnitude of stress. Information on the direction of the principal strain is also given (coating cracks are perpendicular to the principal tensile strain) | The method uses a carbon nanotube polyelectrolite composite which is mechanically strong and where multiple sensing transduction mechanisms can be encoded i.e. films that exhibit changes in their electrical properties to strain. |
| **Uses** | Stress sensor | Identification of crystalline properties, determination of structural properties, etc. | Strain sensor, strain direction indicator | strain and corrosion sensing |
| **Accuracy** | $\sigma$<20 MPa 12% error (±2.5 MPa) $\sigma$>20 MPa 2% error (±2 MPa) | 0.0017% | .03% - .017% depending on atmospheric conditions | ~0.02%, max strain = 1% |

Paint offers an inexpensive alternative to record the spreading of strains in the plate through flaking. The tracing of the flaking of paint is of particular interest for three reasons. (1) Once the paint has flaked, the areas developed are permanent. (2) The area encompassed by the maximum strains is always larger than the area encompassed by residual strains of the same intensity, making the identification easier by means of visual inspection. (3) Visual inspection is a fast method that requires little training of the operator.

The objective of this stage of the research is to estimate the viability of using commercially available paints as a strain-recording method, focusing on the selection of a compound that flakes under strain, an experimental testing procedure, and an analytical verification of the experimental results. The research aims for several characteristics in the paint that are fundamental for condition assessment. The objectives can be summarized as: (1) a stable strain/stress behavior in order to provide results that are comparable among similar test specimens; (2) flaking has to initiate at low levels of strain to make the strain recording compatible with strain levels developed in steel, the objective of this research is to achieve flaking for the yield strain of steel, i.e., 0.15% of strain; (3) flaking has to be localized in the zones that show higher strains and do not spread to lower strain zones.

**Test setup**

A parametric study composed of sixty pure tension tests was carried out on steel coupons. On these coupons a 100 mm strip of paint was applied in the central zone. Each painted coupon represented different characteristics of thickness, composition or application technique. Two types of coupons, shown in Figure 6.1, were considered: (a) a standard steel coupon with a 150 mm by 60 mm steady-strain zone, and (b) a coupon of the same characteristic with a 30 mm slit in the mid zone intended to study the behavior of paint under strain concentrations and verify that the strain patterns observed after the experiment would represent the strain distribution predicted using finite element models.

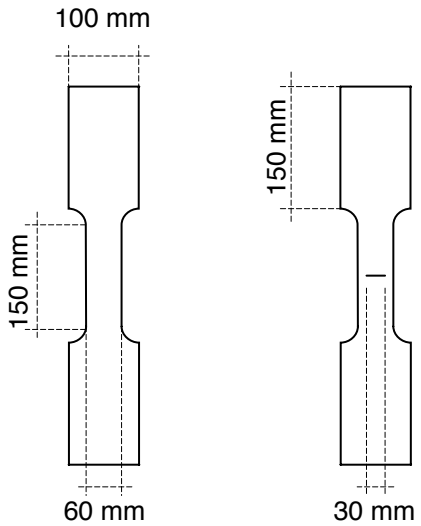


(a) Standard coupon (b) Slitted coupon

Figure 6.1. Types of coupon

Two different methods were considered for the application of the paint. The first method uses an applicator (Figure 6.2 (a)), which consists of a 100 mm long stainless steel rod with two guides at the ends; these guides are oversized with respect to the diameter of the rod, leaving a fixed height separation between the rod and the surface of the coupon. This application method was adequate for either high or low viscosity paints, although the width limit of 100 mm was seen as a shortcoming when the area to be applied was larger than a single coupon.

The second application method considered was a spray gun (Figure 6.2 (b)). In this method the paint was applied on the surface of the coupon by pressurized air blown through a nozzle. The spray gun method provided less control on the thickness of the layer of paint than the applicator described above, but it allowed for the application of paint in larger areas. However, only low viscosity paints could be applied using this technique since the paint had to go through small ducts to reach the nozzle.

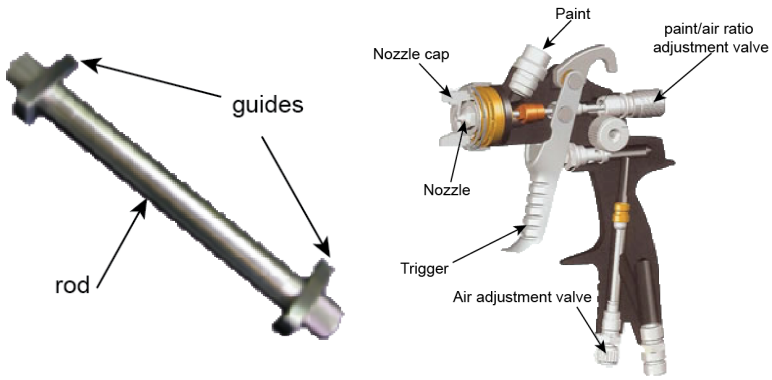


(a) Applicator (b) Spray gun

Figure 6.2. Paint application techniques

The paint thickness was estimated as the average of nine measurements taken at different locations in a grid pattern throughout the painted area. The thickness of the paint was measured through electromagnetic induction. In these instruments, a soft, ferromagnetic rod wound with a coil of fine wire is used to produce a magnetic field. A second coil of wire is used to detect changes in magnetic flux. These instruments measure the change in magnetic flux density at the surface of a magnetic probe as it nears a metal surface. The magnitude of the flux density at the probe surface is directly related to the distance from the metal substrate. By measuring flux density, the thickness of the coating can be determined. The instrument uses a constant pressure probe to provide consistent readings that are not influenced by different operators. The tolerance of the readings is ±1%.

The thickness of the coating was measured seven days after the application of the paint, and the tests were conducted within 10 days of the application of the paint. The procedure was respected in order to avoid differences in the properties of the paint caused by allowing for different drying times between the specimens. External factors such as temperature and atmospheric humidity were not controlled during the tests. However, all the specimens were allowed to dry indoors and under the same atmospheric conditions. The thickness of the coating varied between 10 μm and 480 μm, the average thickness was 70 μm.

The tests were conducted in a universal testing machine (Figure 6.3). The machine consisted of three parts, i.e., the top crosshead, the bottom crosshead and the loading platform. The bottom crosshead was fixed during the loading, while the loading platform and the top crosshead moved up to provide tension or compression. The coupons were placed between the top and bottom crossheads and fixed in position through clamps.

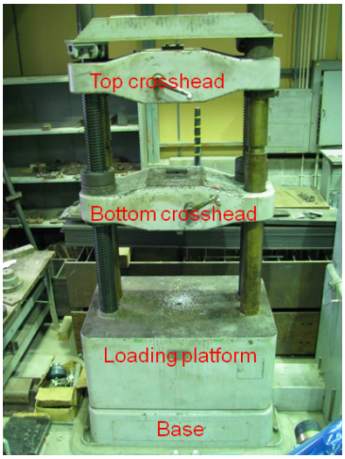


Figure 6.3. Universal testing machine

### 6.2.2 Measurement

Forces and strains were measured for all the specimens. The force was measured through a load cell installed in the loading platform. Strains were measured through strain gauges attached to the side opposite to the painted face. For the standard coupon (Figure 6.1 (a)) a single strain gauge was placed in the middle of the coupon. For the slitted coupon (Figure 6.1 (b)) two strain gauges were used: one at the middle of the coupon, centered between the end of the slit and the edge of the coupon. This strain gauge was intended to measure where the largest strains were obtained. The second strain gauge was placed 50 mm below the slit in order to measure the average strain in the coupon. The behavior of the paint during the tests was recorded using a video camera. These recordings were later synchronized with the readings from the load cell and strain gauges. In the post-processing stage, the strain levels were associated to qualitative characteristics of the paint, i.e., flaking or other observable phenomena.

### 6.2.3 Parametric study on different types of paint

The first stage of testing was composed of 27 specimens. In this stage a parametric study on different types of paint was conducted to ascertain the correlation between the thickness of the layer and the flaking behavior of paint. Four types of paint were used in this stage: lacquer, poster color, urethane and water-based acrylic. Two types of lacquer were used: with and without resin. The lacquer without resin was tested with different concentrations of thinner.

The thickness of paint were chosen based on the assumption that thinner films are more appropriate to induce earlier flaking. This assumption was reached by assuming that paint, once it has dried, behaves in the same way as a solid element, and therefore solid mechanics should apply. In a solid, the forces are distributed through the section as strains through the strain flow. Therefore

a thin film of paint reduces the variation of the strains along the thickness and should induce earlier flaking than a thick film.

For each of the paint compounds selected, four different thicknesses were tested. The paint was applied with a spray gun, and the number of layers of paint applied (from 1 to 4 layers) controlled the thickness of the film. The application method described above was reliable with an average coefficient of variation (ratio of standard deviation to the mean) of 14%.

Nine of the 27 specimens tested in this stage presented visible reactions under strain, whereas the other 18 specimens remained attached to the plate until the coupons failed in tension at approximately 30% strains. The results for these specimens are summarized in Table 6.2. Seven of these specimens were lacquer without resin, one of them was lacquer with resin and one with poster color. The strain levels required for visible effects in the paint ranged between 1.7% and 12%. The strains at which the paint flaked were larger than the original target of approximately 0.15% (approximately the yield strain of steel). However, these results demonstrate the viability of using paint as a method of recording strains.

Table 6.2. Summary of paint flaking strain for parametric analysis

| **Paint** | **Average thickness** | **Visible effect minimum** |
|---|---|---|
| Lacquer (30% | 107.7 | 3.82% |
| | 85.2 | 4.98% |
| | 47.7 | 4.39% |
| | 23.6 | 6.94% |
| Lacquer (60% | 51.3 | 1.77% |
| | 28.2 | 2.68% |
| | 20.2 | 5.34% |
| Lacquer (resin) | 74.9 | 5.21% |
| Poster color | 118.2 | 12.24% |

Figure 6.4 illustrates the general behavior of paint observed during this series of tests. In the figure, four sequential images of one of the poster color specimens are shown. The thickness of the paint was 112 μm. The first effect that can be observed in the pictures (Figure 6.4 (a)) is the appearance of small cracks in the center of the specimen. As the strain increased (Figure 6.4 (b)), the cracks developed into small stretch marks along the width of the specimen. When the strain reached 25% (Figure 6.4 (c)) the stretch marks detached from the surface of the steel plate. Finally for a strain of 30% (Figure 6.4 (d)) the paint fell off.

Figure 6.5 illustrates the behavior of a lacquer specimen. The thickness of the paint was 20 μm. As opposed to the poster color specimen (Figure 6.4) where effects on the paint developed gradually for strains between 12% and 30%, in these specimens the cracks developed quickly throughout the painted area for strains between 5.6% and 6%. After the cracks developed, there were no further distinguishable effects on the paint for larger strains.

It was apparent that the most adequate paint was the combination of lacquer and thinner, as

these specimens were the most successful in flaking when subjected to strain. It was recognized from these set of experiments that a trend exists (Figure 6.6), suggesting that as the average thickness of the film of paint increased, the minimum strain required for the paint to present visible effect decreased. This was contrary to our earlier assumption based on [11], in which a thinner film would induce earlier flaking in the paint than a thicker one. It was reasoned that a minimum threshold level exists for which the bonds that give the film of paint a uniform quality do not form. In other words, the Van der Waals bonds that attach the paint to the steel plate are stronger than the strains generated within the paint film and thus the paint film loses its uniformity and behaves as independent "islands" of paint that appear uniform to the naked eye. This observation was also supported by the fact that the specimen with the thinnest layer of paint ( 9.8 μm) did not flake for any strain level.

Among the lacquer specimens with thinner, the higher concentration of thinner (60%) produced better results than the lower concentration of thinner (30%). The reason behind this probably lies in that thinner is the medium in which the pigments reside, and a higher concentration of thinner permits a more uniform spreading of the pigment particles. The downside of using high concentrations of thinner is that the paint has to be applied in many layers with a wait time of approximately 20 minutes in between applications to prevent the paint from running. From this series of tests it is recognized that the ideal range for thickness of the layer of paint lies between 50 μm and 125 μm, although the upper limit could be higher.

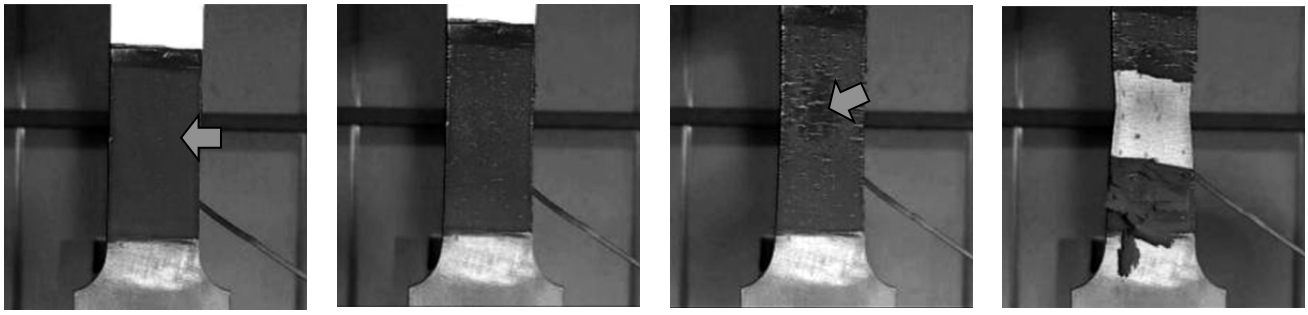

(a) 12% strain (b) 20% strain (c) 25% strain (d) 30% strain

Figure 6.4. Response of poster color under different levels of strain

(a) 5.6% strain (b) 5.9% strain (c) 6.5% strain

Figure 6.5. Response of lacquer under different levels of strain

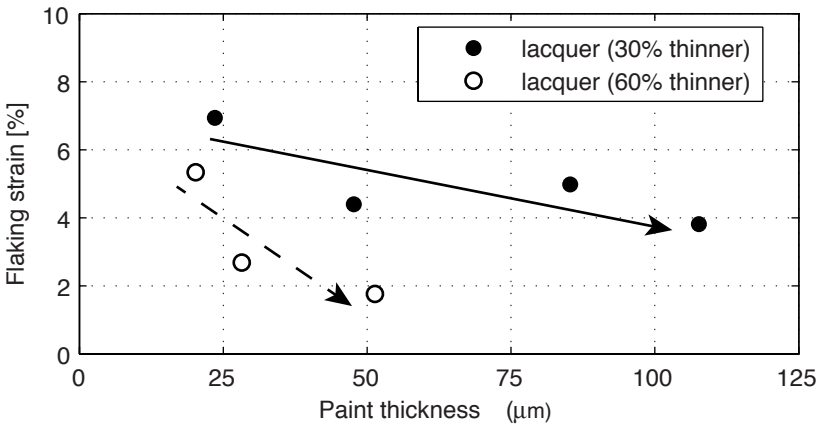


Figure 6.6. Paint thickness versus flaking strain for lacquer compounds

### 6.2.4 Modifications to the paint composition and film mechanics

The second stage of testing was composed of 21 specimens. Three objectives were intended in this stage:

(1) To study the behavior and viability of epoxy paint,

(2) To study the use of additives (filler) in the paint. Filler is a fine granulometry powder that is added to the paint compound, and

(3) To evaluate the inclusion of artificial boundary conditions to the paint coating. This is achieved by adding gridlines to the coating with a cardboard cutter after the paint has dried. Gridlines limit the shear strain propagation within the coat of paint to a fixed strip.

In the same fashion as in the previous set of experiments, lacquer, with and without filler, was applied with a spray gun. Three layers of paint were applied on each specimen to achieve an ideal thickness between 50 μm and 125 μm. The high viscosity of the epoxy paint did not allow for the use of the spray gun, therefore the applicator was used for the specimens with epoxy paint. All specimens in this stage flaked for strains ranging from 0.3% to more than 11%. The results for this stage of testing are summarized in Table 6.3.

The first specimens tested consisted of a layer of lacquer with a 50% concentration of thinner. In these specimens, two-millimeter wide gridlines were introduced (Figure 6.7 (a)). By adding gridlines, the strain propagation within the paint is restricted to a very thin strip, thus the strains concentrate and the cracking or flaking in the paint should take place for smaller strain levels. The efficacy of introducing gridlines is demonstrated by a reduction of the minimum flaking strain from 1.7% obtained in the previous stage to an average of 0.7% obtained in this stage. Figure 6.7 (b) illustrates how cracking developed independently for each strip.

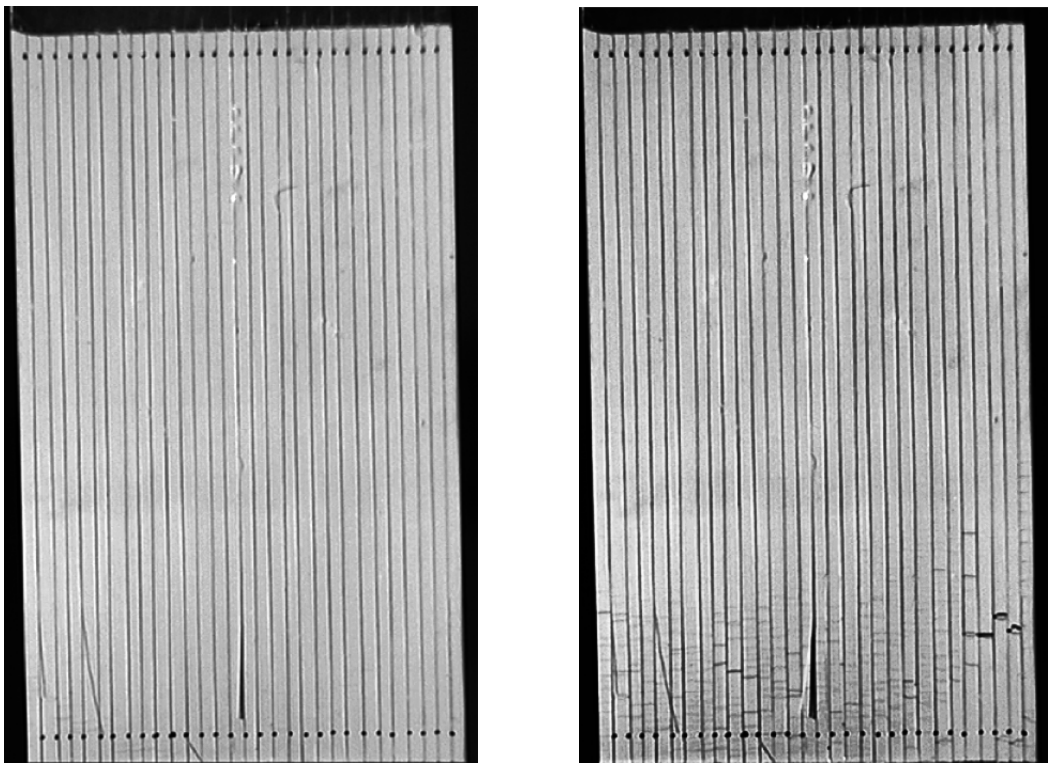

(a) 2% strain (b) 4% strain

Figure 6.7. Response of gridded lacquer under different levels of strain

Following the recommendations from the supplier of the filler, three different types of fillers were used (two different types of silica, denoted by capital letters A and E, and talc, denoted by the capital letter T) on both the epoxy and lacquer specimens.

**Epoxy paint**

Five epoxy and filler specimens were tested, four of the specimens were tested using an epoxy compound (referred to as "compound 1" from here onwards) with the three fillers (A, E and T) with a concentration of 20 mg/100 ml, and a single specimen with a different epoxy compound (referred to as "compound 2" from here onwards) with filler T in the same concentration. Further tests on epoxy paint were planned if the results were suitable. The preparation of epoxy paint differs from the other compounds tested before. In epoxy paint two reacting compounds are mixed, and the paint hardens due to the chemical reactions triggered by the mixing of the compounds. The mixing process of epoxy paint is a sensitive procedure where the two reactants and the filler have to be combined into a uniform mix while avoiding the formation of bubbles.

The specimens using epoxy paint presented some cracking in the surface, but the results did not present any improvement over those obtained for the lacquer specimens. The demands of the mixing process, added to the difficulties encountered when applying the epoxy paint with the applicator, deemed this compound too inefficient to use. Furthermore, the application procedure could not be extended to large surfaces, such as a shear wall. For these reasons epoxy paint was discarded as an alternative.

**Fillers**

In the case of the lacquer specimen with silica fillers, two levels of concentration were used: 17

and 33 mg/100 ml of paint. The granulometry of the talc filler (T) is larger than that of the silica fillers, thus the concentrations used for talc were 3 and 5 mg/100 ml of paint. It can be observed from the data in Table 6.3 that the thickness of the specimens including filler is between 2 and 5 times larger than that applied in the previous stage of testing despite using the same application procedure for both stages. The average thickness of the lacquer specimens in the previous stage was 52 μm, compared to 260 μm in this stage. This increase in the thickness of the film is recognized as an effect of adding filler to the paint because filler did not evaporate when the paint dried. Some problems with the spray gun occurred when the lacquer compound with filler was used, it was difficult to apply the paint on the steel plate and usually clumps of filler would form instead of a uniform film. Another drawback of adding filler is that the paint is more likely to be damaged during the cutting of the grid, and as a result, the flaking of the paint might be hastened, i.e., take place for lower strains than it would if the film was undamaged. When lacquer with filler was subjected to strain, the paint behaved in a similar fashion as poster color (shown in Figure 6.4), although the cracking strain was significantly reduced (20% of the strain levels obtained for poster color), and the results appear to be more stable than the aforementioned paint.

Table 6.3. Results of second stage of tests

| Paint | Average thickness (μm) | Visible effect minimum strain |
|---|---|---|
| Epoxy 1 + filler A 20 | 95.8 | 2.51% |
| Epoxy 1+ filler E 20 | 113.1 | 6.17% |
| Epoxy 1 + filler T 20 | 182.9 | 2.44% |
| Epoxy 1 + filler T 20 | 92.6 | 14.07% |
| Epoxy 2 + filler T 20 | 155.9 | 2.47% |
| Lacquer (50% thinner) grid | 121.9 | 0.37% |
| | 118.0 | 1.10% |
| Lacquer (50% thinner) + filler A 33 | 343.6 | 2.59% |
| Lacquer (50% thinner) + filler A 17 | 401.6 | 2.10% |
| Lacquer (50% thinner) + filler E 33 | 287.0 | 2.45% |
| Lacquer (50% thinner) + filler E 17 | 482.6 | 1.42% |
| Lacquer (50% thinner) + filler T 5 | 99.4 | 1.80% |
| Lacquer (50% thinner) + filler T 3 | 113.0 | 4.45% |
| Lacquer (50% thinner) + filler A3 grid | 95.3 | 1.82% |
| Lacquer (50% thinner) + filler A3 grid | 117.1 | 2.18% |
| Lacquer (50% thinner) + filler A7 grid | 132.2 | 1.60% |
| Lacquer (50% thinner) + filler A10 grid | 204.6 | 0.47% |
| Lacquer (50% thinner) + filler A10 grid | 70.6 | 2.26% |
| Lacquer (50% thinner) + filler A10 grid | 59.0 | 1.61% |
| Lacquer (50% thinner) + filler E10 grid | 67.6 | 1.41% |
| Lacquer (50% thinner) + filler T10 grid | 57.8 | 1.11% |

**Filler and gridlines**

The specimens that combined filler and gridlines considered several concentrations of filler A (the concentration is mg/100 ml is noted next to the filler type in Table 6.3). Fillers E and T were also tested. The amount of filler added to the paint for the tests with gridlines was reduced in an attempt to maintain the uniform quality of the paint. It is apparent that a quantity of 10 mg/100 ml is most appropriate if filler is to be used. It is also worth of notice that for the initial tests of paint with filler, 17 mg/100 ml were used and the flaking strain was 2.1% in average; therefore it is noted that 10 mg/100 ml is more appropriate than a higher concentration since this concentration maintains the uniformity of the film of paint. Unfortunately, the results were not stable and no trend was observed with regard to the paint thickness, amount of filler, and flaking strain. In conclusion: (1) The good result, i.e., flaking at 0.47% strain (highlighted in light gray in Table 6.3) obtained for the lacquer specimen with 10 mg/100 ml concentration of filler A could not be replicated. The lower flaking strain observed could be associated to the thicker layer of paint applied, but it is more likely to be associated to other factors e.g. humidity or temperature at the time of testing. 2) When the results with a reduced amount of filler are compared, none of the different fillers is clearly better than the other. Therefore, there is no conclusive evidence that suggests an improvement of the performance of the paint by using filler. On the other hand, the results obtained in this stage indicate that the inclusion of gridlines reduces the flaking strain of lacquer (without the inclusion of fillers) from an average of 5.86% obtained in the previous phase to an average of 0.74% (highlighted in dark gray in Table 6.3), which makes it a suitable improvement for recording strains.

When the flaking performance and the ease of use of the different compounds were taken into consideration, it was apparent that using lacquer with a 50% concentration of thinner was the best alternative to record the spreading of strains. The preparation of the compound by mixing two fluids was straightforward and easy to replicate. Furthermore, the durability of the paint coating without filler was far superior to the quality of the coating when filler was added.

### 6.2.5 Compound stability

The last stage of the study consisted of two control specimens and 9 specimens of lacquer with a 50% concentration of thinner and similar thickness (68.5 μm in average). Five of these specimens were standard coupons (Figure 6.1 (a)), and the other four were slitted coupons (Figure 6.1 (b)). This last series of tests were intended to determine the stability and reliability of the selected paint.

The following list summarizes the conclusions from the previous series of tests and characterizes the final choice of compound:

(1) The ideal thickness of the film of paint ranges between 50 μm and 125 μm.
(2) There is no substantial benefit of adding filler. Furthermore, the disadvantages of adding filler to the compound outweigh any reductions in the flaking strain that filler might provide
(3) Lacquer with a 50% concentration of thinner presented the lowest flaking strain throughout the tests
(4) The introduction of gridlines reduces the flaking strain of paint.

The average thickness of the paint layer for this stage was 68.5 μm and the average flaking strain was 0.31% with a standard deviation of 0.23% (0.10% if the second test is counted as an

outlier). These results provide a concrete confirmation of the viability of this compound for recording strains. The flaking strains and the corresponding thickness of the film are shown in Table 6.4.

Table 6.4. Results of third stage of tests

| Paint | Average thickness (μm) | Visible effect minimum strain |
|---|---|---|
| Lacquer grid | 119.3 | 1.18% |
| Lacquer (50% thinner) resin grid | 26.3 | 2.00% |
| Lacquer (50% thinner) grid | 58.2 | 0.14% |
| | 134.1 | 0.76% |
| | 79.0 | 0.86% |
| | 68.0 | 0.27% |
| | 64.6 | 0.14% |
| | 60.8 | 0.15% |
| Lacquer (50% thinner) grid (Slitted coupon) | 67.7 | 0.34% |
| | 74.7 | 0.26% |
| | 72.1 | 0.43% |
| | 72.1 | 0.23% |

Figure 6.8 shows the flaking progress of one of the standard coupon tests. Figure 6.8 (a) shows a picture taken when the strains reached 0.10%, at this point no flaking is apparent. Figure 6.8 (b) shows the initiation of flaking in the lower left corner, where five strips began to crack (left arrow) and one of the strips began detaching itself from the steel plate (right arrow); when the strains reached 0.20% (Figure 6.8 (c)) cracking was apparent in all the lower section of the painted zone. Figure 6.8 (d) shows cracking throughout the painted zone for strains of 0.30%.

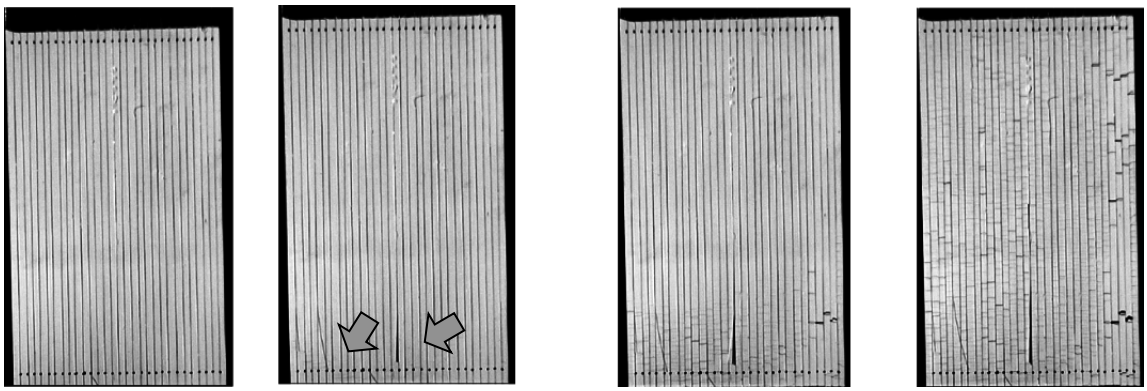

(a) 0.10% (b) 0.15% (c) 0.20% (d) 0.30%

Figure 6.8. Paint flaking induced by strain: lacquer (50% thinner) grid (60.8 μm thickness)

The slitted coupon specimens were intended to study the ability of paint to represent strain patterns and to study the behavior of paint under strain concentration. The responses of all four tests showed a clear indication of the strain zones (Figure 6.9 (a)), furthermore, the cracking did not

propagate to zones that experienced lower strain levels (Figure 6.9 (b)).

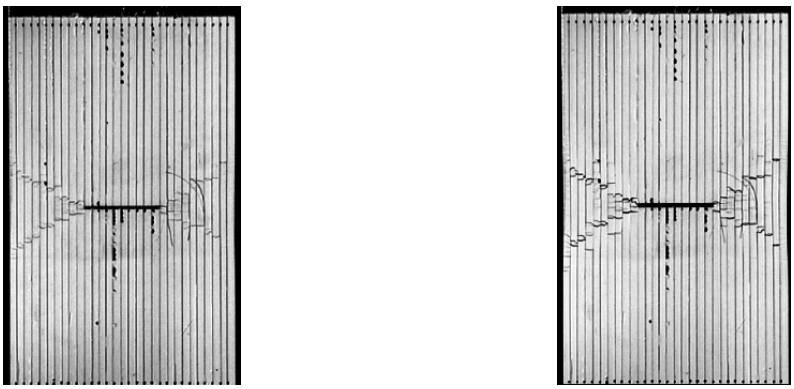

(a) 0.35 % strain (b) 0.50% strain

Figure 6.9. Paint flaking induced by strain: lacquer (50% thinner) grid - slit (74.7 μm)

### 6.2.6 Comparison to FEM model

A finite elements model (FEM) was constructed in ABAQUS [12] to verify the correct determination of the strain pattern shown by the cracked paint in the coupon. The model was constructed following a similar procedure as that described in Chapter 3 and subjected to axial loading in the same fashion as the tested specimen. Figure 6.10 shows a comparison between the results obtained from the FEM model: in darker shades of gray are shown the strains that exceed the yield strain of steel (0.15%) (Figure 6.10 (c)), and on the sides the four slitted specimens as seen after the detached paint had been scraped (Figure 6.10 (a), (b), (c), and (d)). A very good agreement is observed between the results of the finite element model and the results obtained from the flaking of the paint in the four slitted specimens. The extension of the strain areas in the FEM model correspond to the sections where paint detached in the coupons.

The good results from the comparison between the FEM model and the flaking behavior of the paint confirm the viability of paint as a method for recording strains.

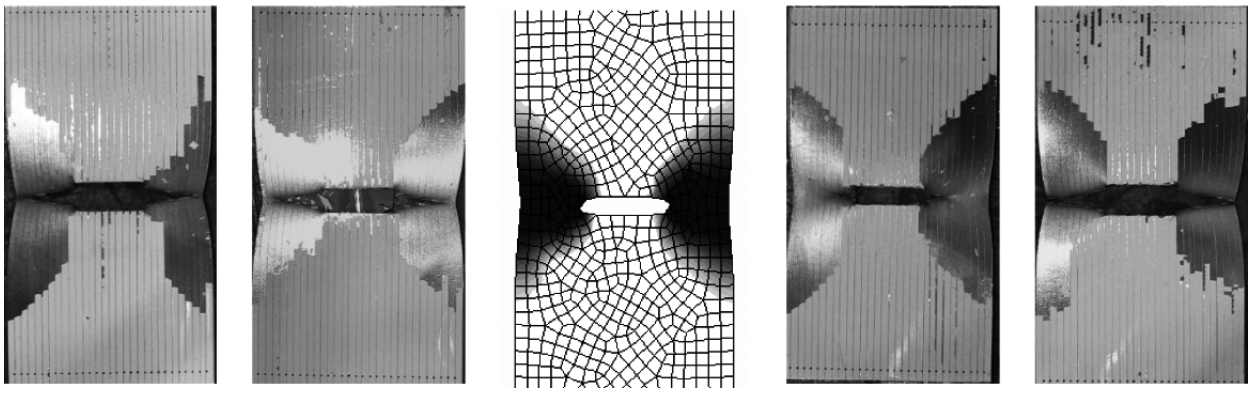

(a) Specimen 1 (b) Specimen 2 (c) FEM model (d) Specimen 3 (e) Specimen 4

Figure 6.10. Strain pattern comparison

## 6.3 Performance of paint for strain recording in slit walls

The paint selected in Section 6.2 was applied to slit walls that were tested under an online hybrid test on a first stage, and afterwards, under statically applied cyclic load. The results regarding the structural performance of the slit walls have been discussed in Chapter 4. The lacquer compound with a 50% concentration of thinner was applied on the slit walls with a spray gun in three successive layers. The paint was applied directly on top of the steel plate on the condition assessment section of the walls ( Figure 6.11). The surface of the steel plate was sanded with a fine grain sand paper and cleaned with acetone to remove any remainders of the oil in which steel plates are coated to avoid corrosion.

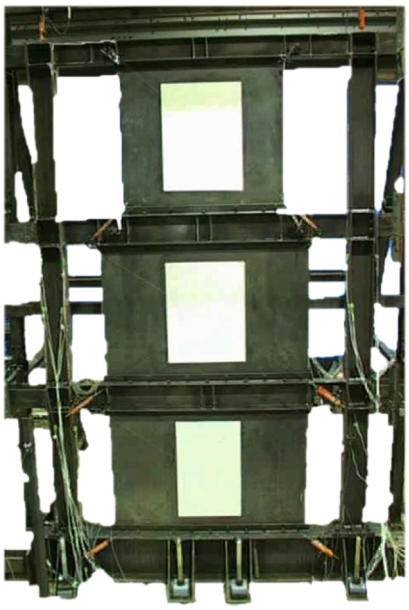

Figure 6.11. General view of the online test specimen (see Chapter 4)

Two standard coupon tests were conducted following the same protocols as during the parametric study to achieve a twofold objective: (1) determine the elastic modulus and yield strain of the steel used for the experiment and (2) establish the flaking strain of the paint compound. The results from these tests indicate that the flaking of the paint used for the online-hybrid test flaked for an average strain of 2.5%. Unfortunately, this larger flaking strain reduced the extension of the area where flaking took place, and thus decreased the drift identification capabilities in the element.

### 6.3.1 Performance of paint flaking during tests

Three digital cameras were placed in a scaffold located opposite to the experimental test specimen to record the progress of the flaking of the paint in the walls. Pictures were taken at the positive and negative displacement peaks throughout the test. Before the pictures were taken, the painted areas of the walls were scraped with a metal brush to remove the paint that had already detached. A similar procedure was implemented during the cyclic tests that followed the online test.

The pictures taken during the two experiments generated a total of 168 high-resolution color

images. To extract the flaking area, the pictures were post processed using ImageJ [13], [14] after the following procedure:

(1) A mask was applied to the color image to isolate the painted area in the picture. This step was necessary, because it eliminated false white areas introduced by lights reflecting on the surface of the steel plate. Figure 6.12 (a) shows an original image and Figure 6.12 (b) shows an example of the image if it were converted directly to black and white. The mask that is detected for the picture is shown in Figure 6.12 (c) and the result from applying the mask is shown in Figure 6.12 (d).

(2) The color image was then transformed into a black and white image. Digital color images are composed from the addition of three grayscale images that represent the level of darkness in a particular spectrum, e.g. red, green and blue, known as channels. The rest of the chromatic spectra can be represented by different combinations of these three basic colors. Separating color images into each of these channels has been and operating between them is a common technique to identify colored object in an image. However, there was little advantage in separating and operating the three channels in the spectrum, as the color of the paint used was white, and it appeared identical in either channel. The threshold for the conversion was set at a level of 100 out of 256. In practical terms it means that all color values below 100 were turned into black and all color values above 100 were turned into white. This procedure generated images with a white background and only the flaked area and the slits in black as shown in Figure 6.12 (e).

(3) The black areas defined by the slits are removed manually. For small deformations, the black areas defined by the slits represented only a small fraction of the total dark areas, but as the lateral drift sustained by the slit wall increased, the flexural links separated due to inelastic lateral-torsional buckling. The separation of the flexural links was also shown as dark areas in the pictures, which distorted the readings from the flake areas of the paint. An image where the slits have been removed is shown in Figure 6.12 (f).

(4) Scale images. As the pictures were taken with cameras at different locations and with different levels of magnification, the images were all resized to the same scale. The length of the slits was used as a reference parameter to obtain a good approximation of the scale of each image.

(5) Calculate area. One of the features of the software used for post-processing of the images (ImageJ) is the analysis of particles within an image. This feature was used after removing all the dark areas in the image that did not represent the flaking of paint. The areas obtained by this method were later exported to text files.

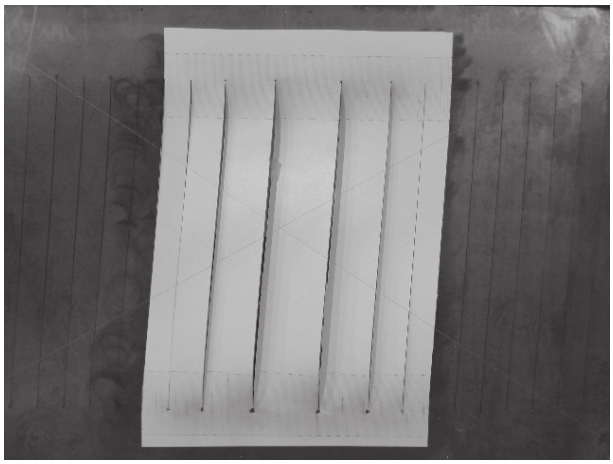

(a) Original image

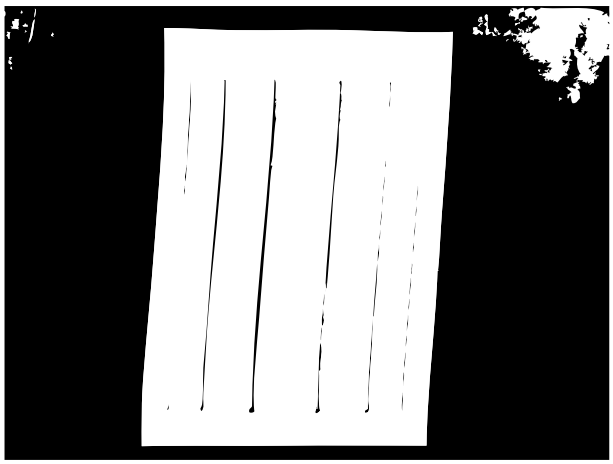

(b) Thresholded image

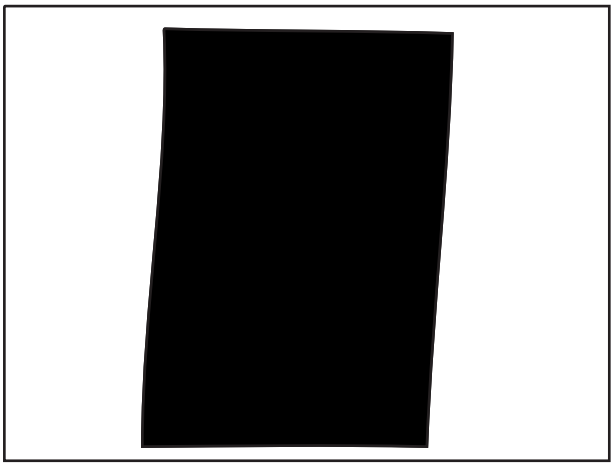

(c) mask

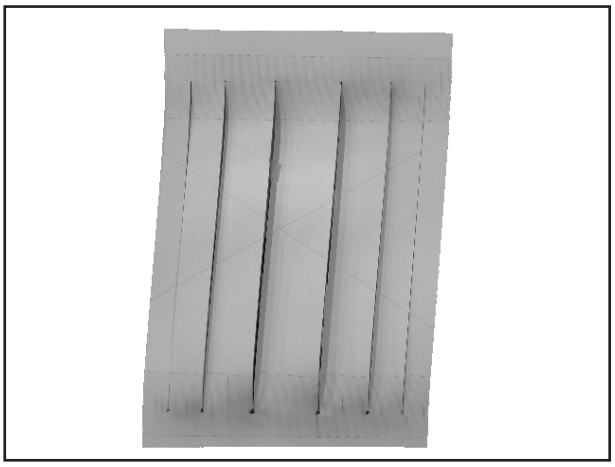

(d) after application of mask

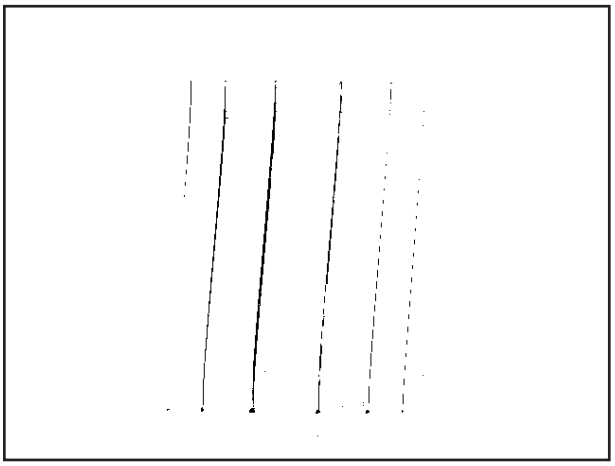

(e) Thresholded image

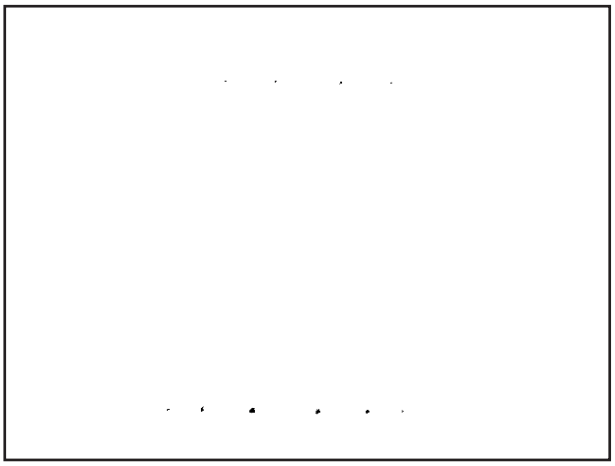

(f) Final image (only flaking area)

Figure 6.12. Image processing example

It is worthy to mention that the procedure could be fully automated, and it was implemented as a macro for all steps with the exception of step (4). The automation of step (4) would be implemented by isolating circular patterns (that represent the flaking of paint) within the images.

The elongated elements (slits) would be discarded. The development of this feature allowed for the processing of a large number of images and it can easily be extended to the processing of video files.

From the experimental data, the history of drift angles and the date and hour of each step of the experiment were obtained. The timing of the experiment is compared against the metadata of the pictures to confirm the instant at which the pictures were taken and thus the corresponding drift angles can be calculated. Figure 6.13 shows the peaks identified for the first story slit wall, the numbers in bold font represent peaks in the positive direction and the numbers in normal font represent peaks in the negative direction. The metadata available from the pictures is plotted as stems, it can be observed from the figure that pictures were available for the first five positive peaks and for both positive and negative peaks after this. A delay becomes apparent for the latter pictures taken, this delay is associated to differences in the internal clock of the cameras and the computers, where small differences in time accumulated as the test progressed. For the case of the cyclic test, the coordination between the experimental data and the pictures was easier to achieve since pictures were taken at every step.

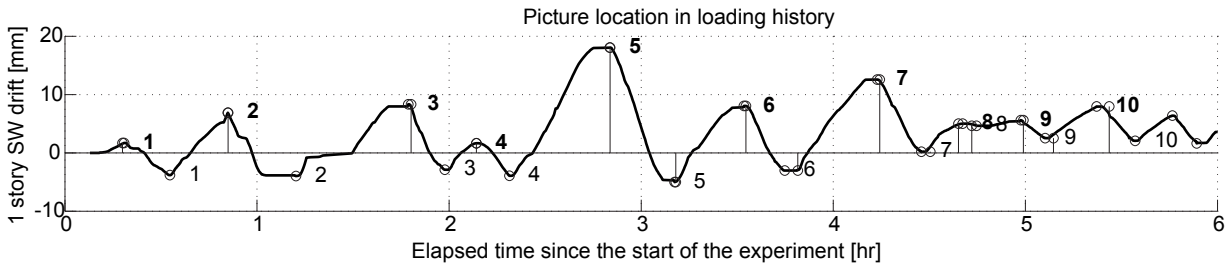


Figure 6.13. Loading history of first story slit wall during the online test

Figure 6.14 presents the results from the flaked areas accumulated throughout the online test for all three slit wall specimens, it can be observed that the general progression of the flaking data points tends to grow as the drift angle increases. With the exception of specific outliers that are most probably associated with problems in pictures the capture than with the behavior of the paint.

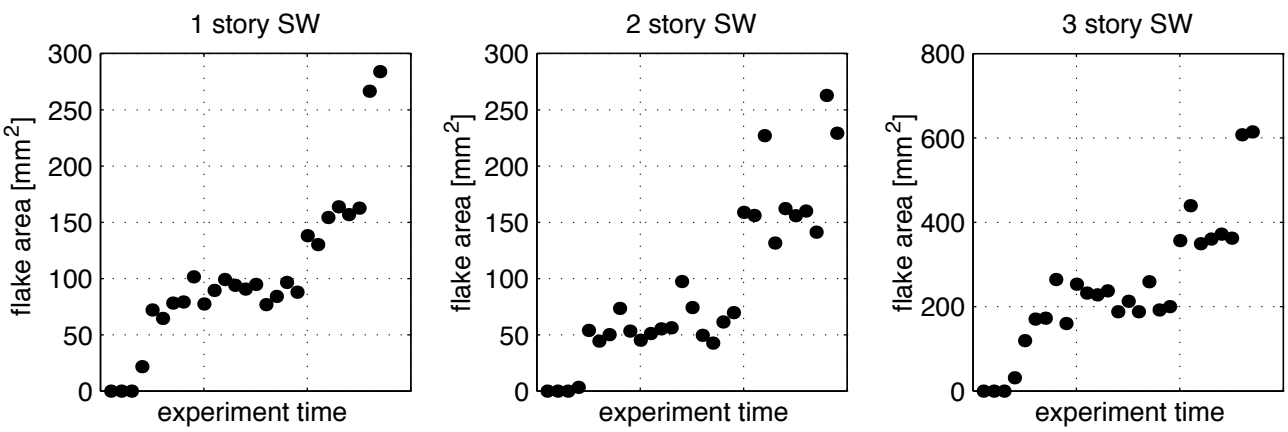


Figure 6.14. Progression of flaked area in the three slit wall specimens during the online tests

A more representative interpretation of the data is shown in Figure 6.15 (a), here the flaking areas of the first story slit wall are organized according to the maximum drift angle that the wall had ever experienced during the test. In the figure, red crosses represent the flaking of the paint during the online test, whereas the blue dots represent the flaking of the paint during the cyclic test. Several aspects of this figure are interesting:

(1) The flaking of the paint is clustered in relatively well defined zones for each of the drift angle studied. The large variability in the 1.5% band is probably explained by the large number of cycles that were experienced after this drift level was achieved during the online testing. The procedure followed to remove the paint that had detached involved scraping the paint with a metal brush, which also removed small areas from the edges of the flaked area. This was exacerbated by the large flaking strain of the paint, which reduced the flaking area and therefore made the rather small areas scraped from the edges introduce larger errors in the calculation of the area. This problem would not be experienced in a real application situation, because the scraping would take place only once before the pictures were snapped.

(2) The maximum drift angle achieved during the final loading in the online test was 3.25%. In the cyclic loading test, the loading protocol started with cycles to a drift angle of 1%.The paint that flaked for those cycles below the maximum drift angle achieved earlier in the online test (3.25%) were not reflected as a significant increase in the flaking area.

(3) For the largest lateral deformations in the cyclic test (above 3% drift angle) a single data point falls within same range as for smaller deformations. This point corresponds to the first peak achieved in the corresponding loading amplitude and since the pictures were taken at the peaks, it might be argued that the flaking areas were not representative of the behavior during the complete cycle, since the wall had been loaded only in a single direction and the paint was under strain at the time of the capture of the picture.

(4) When the outlier points described above were removed, drift bands representing each of the levels of loading can be identified within the plot (Figure 6.15 (b)). In addition, the coefficient of variation for these three drift angles is significantly reduced, in particular for the 6% and 8% drift angles. A summary of the average flake area, the standard deviation, and the coefficient of variation is presented in Table 6.5.

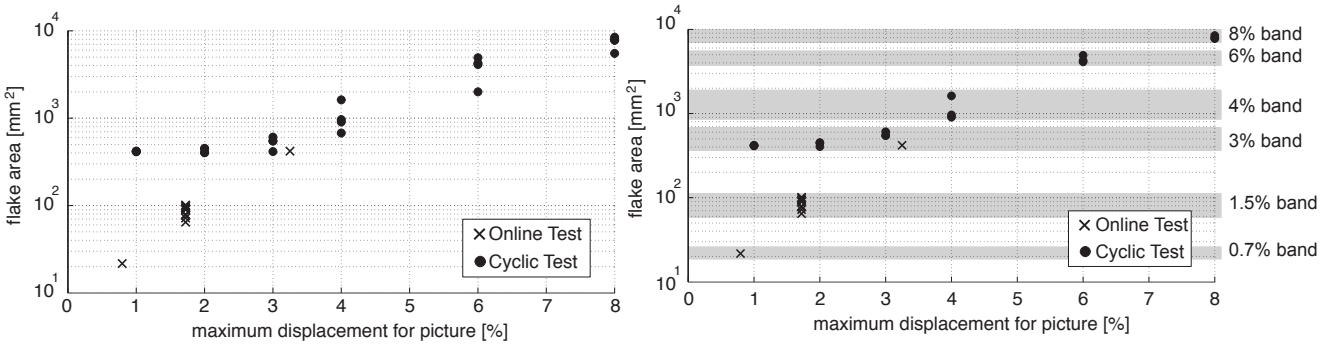


(a) All data points (b) Banded results – outliers removed

Figure 6.15. Flaking area dispersion for different drift angles (1st story SW specimen)

Table 6.5. Statistical summary of paint flake results

| | All data points | | | Without outliers | | |
|---|---|---|---|---|---|---|
| **Drift angle** | Average ($mm^2$) | Std. deviation ($mm^2$) | Coeff. of variation | Average ($mm^2$) | Std. deviation ($mm^2$) | Coeff. of variation |
| **1.7%** | 86 | 12 | 14% | 87 | 12 | 13% |
| **3.0%** | 455 | 67 | 15% | 457 | 70 | 15% |
| **4.0%** | 1041 | 406 | 39% | 1163 | 397 | 34% |
| **6.0%** | 3822 | 1264 | 33% | 4429 | 432 | 10% |
| **8.0%** | 7405 | 1295 | 17% | 8035 | 366 | 5% |

### 6.3.2 Accuracy of strain recording compared to FEM analysis

Despite the late flaking of the paint, the coatings in all SWs presented flaking for drift angles as low as 0.5%, i.e., the strain concentration at the end of the slits caused the strain in these locations to exceed 2.5% for drift angles of 0.5%, although in an area much smaller than would have appeared if the coating had flaked for lower strains. The flaking pattern expanded as the drift angle increased and was not altered by succeeding cycles of smaller amplitudes. Figure 6.16 (a) and (b) show the flaking pattern in the bottom of the central slit of the first story SW at 0.5% drift during the online test. In Figure 6.16 (a) the location of the strain gauges in the vicinity of the slit are shown as black rectangles and the strains recorded when the wall was subjected to a 0.5% of drift angle are written alongside the rectangles. The vertical strain contours including the corresponding strain values in percentage obtained from an associated finite element model are overlaid on top of the picture. The readings from the strain gauges agree with the results obtained from the finite element model. Figure 6.16 (b) shows the maximum principal strains at 0.5% drift obtained from the finite element model. The strains at the flaking area reaches 2.25% which are very similar to the flaking strain obtained from the standard coupon test (2.5%).

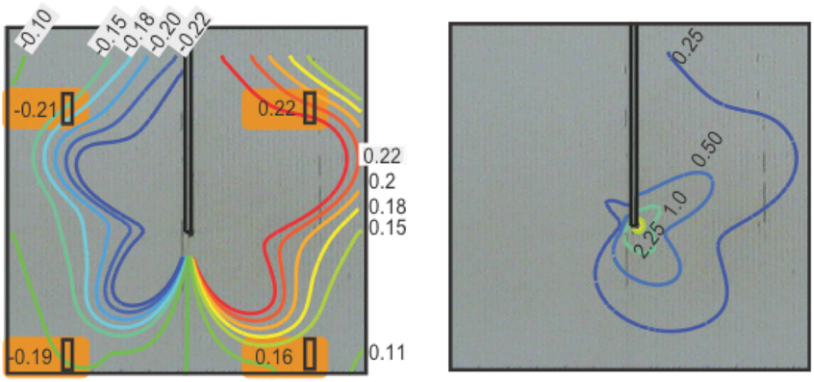


(a) Vertical strains (b) Principal strains

Figure 6.16. Strains from FEM model compared to experimental results

## 6.4 Conclusions

This chapter presented the development of a method to record the spreading of the maximum strains through the surface of a steel plate. A series of tests were conducted on steel coupons under tensile strain in order to identify a strain sensitive paint for condition assessment purposes. Afterwards the paint compound was applied on the surface of three reduced-scale slit wall specimens and tested in an online-hybrid test and under a static loading protocol. The main finding of this chapter can be summarized as follows:

(1) A reliable paint compound, composed of lacquer with a 50% concentration of thinner and with 2 mm wide gridlines cut into the film, was identified as presenting visible responses to strain. The response initiates at strains not higher than 0.4%

(2) The flaking of the paint takes place only in those areas that exceed the flaking strain and does not propagate to lower strain areas. Thus, preserving the maximum strains experienced.

(3) The extension of the strain areas determined by the flaking of the strains agree with the extension of strain areas determined by finite element models.When paint is applied to slit walls, the flaking areas develop in the zones with high strain concentrations. This strain areas can be recorded and later associated to different levels of drift angle.

(4) Pictures of the flaking of paint can be analyzed to determine the extension of the areas where flaking has taken place. Larger areas of flaking represent larger drift angles to which the slit wall has been subjected. Thus identification of maximum drift angles by means of paint flaking can be achieved.

# REFERENCES


[1] de Joussineau, G., Petit, J.P. and Barquins, M. (2005) "On the simulation of the flaking paint due to internal stresses: A simple model", *International Journal of Adhesion and Adhesives*, 25(6), pp. 518 – 526

[2] Kendall K. (1975) Crack propagation in lap shear joints*, Journal of Physics D*, 8(5), pp. 512 – 522

[3] Devos, P., Baziard, Y., Rives, B, and Michelin, P., (2001), "Adherence evaluation of paint coatings using a three-point flexure test and acoustic emission", *Journal of Applied Polymer Science*, 81:8, pp. 1848 – 1857

[4] Santos, A., Bray, D., (2000), "Ultrasonic stress measurement using PC based and commercial flaw detectors", *Review of Scientific Instruments*, 71(9), pp. 3464 - 3469

[5] Hilley, M., (1971), "Residual Stress Measurement by X- Ray Diffraction" , SAE J784a, *Society of Automotive Engineers*, Warrendale, PA, 1971, pp. 21-24

[6] Prevéy, P.S., (1986), "X-Ray Diffraction Residual Stress Techniques," *Metals Handbook* , **10**, (Metals Park, OH: ASM), pp. 380-392

[7] Alexopoulos, P., and O'Sullivan, T. (1990), "Mechanical Properties of Thin Films", *Annu. Rev. Mater. Sci.*, 20, pp. 391 – 420

[8] Evans, H., Crumley, G., and Demaray, R., (1983), "On the Mechanical Behavior of Brittle Coatings and Layers", *Oxidation of Metals,* 20(5/6), pp. 193 – 216

[9] Strawbridge, A., and Evans, H., (1995), "Mechanical Failure of Thin Brittle Coatings", *Engineering Failure Analysis*, 2(2), pp. 85 – 103

[10] Loh, K., Kim, J., Lynch, J., Kam, N., amd Kotov, N., (2007), "Multifunctional layer-by-layer carbon nanotube–polyelectrolyte thin films for strain and corrosion sensing", *Smart Materials and Structures*, 16, pp. 429 – 438

[11] Suo, Z., and Hutchinson, J., (1989) "Sandwich Test Specimens for Measuring Interface Crack Toughness" *Materials Science and Engineering*, **A107**, pp. 135 – 143

[12] Abaqus Inc., "ABAQUS Version 6.7 User's Manual," *http://www.abaqus.com*, 2007.

[13] Rasband, W., ImageJ, U. S. National Institutes of Health, Bethesda, Maryland, USA, http://rsb.info.nih.gov/ij/ , 1997-2009.

[14] Abramoff, M., Magelhaes, P., Ram, S. (2004) "Image Processing with ImageJ". *Biophotonics International*, 11(7), pp. 36 – 42

# CHAPTER 7

# Distributed Online Test to Collapse

## 7.1 Introduction

### 7.1.1 Online testing to collapse

In Chapter 4 a conventional hybrid test method [1]-[3] was used to study the earthquake response behavior of a steel moment frame equipped with unequally slitted steel shear walls. This chapter explores the extensibility of the testing scheme on the simulation of collapse. The hybrid test method has great potential to test large scale structural systems to collapse as it is not required to physically simulate the inertial effect and gains from the extensibility associated with the substructure technique. In particular, the experimental substructures can be strategically selected and tested at large scales to capture the sequence of local failures leading to collapse.

In the past decade, various geographically distributed hybrid tests have been conducted between different laboratories including remote experimental and numerical substructures [4], [5] [6]-[9]. Watanabe et al. [4] conducted several rounds of distributed tests on a base-isolated bridge with multiple piers. Two rubber bearings were tested at two distributed laboratories, each bearing loaded by two hydraulic actuators. More recent efforts have focused on developing a general software framework for hybrid experimental-computational simulation such as OpenFresco at the University of California, Berkeley [5]. Demonstration tests included a base-isolated bridge pier tested collaboratively between Japan and U.S with only one rubber bearing tested using three quasi-static jacks. Another hybrid test framework, Internet-based Simulation for Earthquake Engineering ( ISEE), was developed at National Center for Research on Earthquake Engineering (NCREE), Taiwan [6]. A three-site hybrid test was conducted on three piers of a multi-span continuous bridge. Each laboratory handled one pier using two hydraulic actuators. Mosqueda et al. [7] conducted a five-site collaborative test within the NEES [8] laboratories in the U.S. Five piers of a six-span bridge were taken as the substructures, in which two were physically tested, each using one hydraulic actuator, while the others were numerically simulated. Also as part of the NEES, a hybrid test framework UI-SIMCOR was developed at the University at Illinois at Urbana-Champaign [9]. Recently, a three-site large scale bridge hybrid test was conducted with two experimental sites, each loading one pier by two hydraulic actuators.. Most past distributed hybrid tests have been on multi-span bridges with the piers as substructures. This model provides relatively simple boundary conditions that could be controlled by limited number of actuators. Further, few

hybrid tests have examined structures up to collapse with significant geometric and material nonlinearities [10], [11]. A key step in a hybrid test to collapse is partitioning the structure to capture the collapse mechanism experimentally while properly enforcing boundary conditions.

Schneider and Roeder [12] examined typical substructuring assumptions that simplify inflection point is expected. Although the numerical global response compares well between the original model and a model that includes moment releases, larger differences have been observed in the local behavior near the hinges [13]. Moreover, at the partition, stiff degrees of freedom such as axial deformations in columns may emerge at the boundaries. Modern testing facilities have limited control tolerance which may introduce large experimental errors into the whole hybrid test system, particularly when controlling the stiff degrees of freedom, such as axial and rotational deformations. Thus, the exactness of the boundaries requires a compromise between the overall simulation accuracy and the facility control capabilities.

In this chapter, the seismic response of a four-story steel moment frame to collapse is examined using an extensible hybrid test framework for collaborative testing. Two experimental substructures located in Japan and the U.S. are each loaded with four actuators to properly simulate boundary forces including varying axial loads on the columns. The prototype structure is based on the full-scale specimen tested to collapse at the Hyogo Earthquake Engineering Research Center of Japan (E-Defense) in September 2007 [14], which provides a benchmark for the expected results. The substructure hybrid test framework used in these experiments is extensible for various types of finite element programs and the laboratories with different software and hardware environment [15]. A new flexible test scheme associated with open- and closed-loop control was implemented at the boundary degrees of freedom to compromise with the difficulties in controlling stiff degrees of freedom. In this study, particular attention was given to the substructuring approach in order to minimize related errors while enabling a realistic simulation within laboratory capabilities. An innovative substructuring approach with overlapping domains between the experimental and numerical substructures is explored to apply complex boundary conditions.

### 7.1.2 Organization

This chapter first describes the hybrid test framework and numerical studies conducted to select the substructures. The proposed framework is then applied to evaluate the seismic performance of large-scale steel structures from the onset of damage through collapse. In this approach, only the critical subassemblies of the structural system leading to the collapse mechanism are evaluated experimentally while the global response of the remaining structure is captured numerically. The selection of the subassemblies and the sensitivity in enforcing boundary conditions between experimental and numerical substructures in order to capture the initiation of collapse is examined in detail. Further, the hybrid test results are compared to the full scale earthquake simulator test to examine both the global response and the distribution of stresses in the frame.

## 7.2 Basics of Iterative Hybrid Test Framework

The theoretical basis and detailed implementation of the distributed hybrid test system can be found

in previous studies [15]. Only the major features are introduced here with new capabilities highlighted in the next section. In this system, the simulated structure is divided into multiple substructures, as shown in Figure 7.1. All substructures are equally treated and can be geographically distributed to various laboratories, with the dynamics considered in each substructure rather than in the overall structure model. A central part of this system, called the "Coordinator", is devised to achieve the compatibility and equilibrium at the boundaries between substructures. The boundary displacements and the corresponding forces are exchanged between each substructure and the "Coordinator" via an I/O interface. In this manner, each substructure is implemented as a highly encapsulated "Partner", and can be treated as either an experimental part or an analytical part.

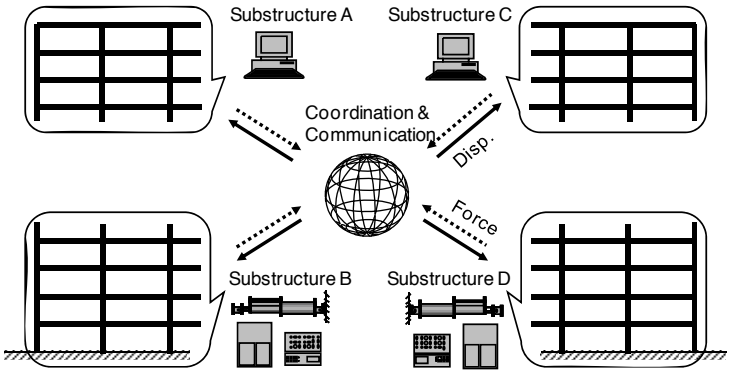


Figure 7.1. Concept of distributed hybrid test framework

An example containing one tested substructure and one analytical substructure is used to explain the implementation of the hybrid test. At the beginning of one step, the "Coordinator" sends a trial displacement, which can be the displacement of the previous step, to both substructures. Compatibility between the two substructures is explicitly satisfied. Then, the substructures are analyzed independently either by numerical simulation or physical test. The boundary forces are sent back to the 'Coordinator', where the equilibrium at the boundaries is examined. If the boundary is balanced in force, the current step is completed, and the analysis proceeds to the next step. Otherwise, the 'Coordinator' calculates a new trial displacement based on the unbalanced force at the boundary. The above procedure is essentially an iterative procedure which considers two key issues: an efficient algorithm to find the real boundary displacement systematically, and a test procedure to avoid iterations for tested substructures.

The "Coordinator" only requires the unbalanced force at the boundary to determine the next trial displacement. However, the typically-used tangential stiffness matrix is difficult to estimate in a hybrid test because the measurement of the tested substructures has limited resolution. One alternative is to use the secant stiffness, which can be updated by the quasi-Newton method with the gradient information from previous steps. It should be noted that the initial value of the stiffness may not be necessarily close to the tangential stiffness, but any positive-definite matrix is acceptable. The updated trial displacement can be calculated by the common equation solution procedure using the unbalanced force and the updated secant stiffness. The quasi-Newton method has a super-linear (between linear and quadratic) rate of convergence, which is faster than the

typically used modified Newton-Raphson method with a linear rate of convergence.

To avoid iterations on the experimental substructures, the test procedure is designed as a predictor-and-corrector pattern. In the predicting stage, a round of the quasi-Newton procedure is used to calculate the predicted boundary displacements in which the reaction force of a tested substructure is calculated using an assumed linear stiffness, commonly the initial stiffness. Once equilibrium is satisfied, the predicted displacement is then imposed on the experimental specimen as a physical loading, and the reaction force is measured. The boundary forces may become unbalanced in this step due to the nonlinear behavior of the substructure. A second round of the quasi-Newton procedure is then conducted to correct this unbalanced force using the same secant stiffness for the experimental substructures.

## 7.3 Flexible Test Scheme

A combined open-loop and closed-loop control is incorporated into the test scheme to release the strict boundary conditions at insignificant degrees of freedom, which are often difficult to control at high precision. This test scheme is hereafter called the flexible test scheme. This approach is able to maintain acceptable accuracy for the overall structure seismic performance while simplifying the implementation of complex boundary conditions.

Both open-loop and closed-loop control as used here refer to the interaction between substructures. Closed-loop control is used to enforce strict boundary compatibility and equilibrium by the coordinator program. Taking a six-story base-isolated building as an example, the two isolators at the base isolation layer are tested, while the superstructure is simulated numerically, as shown in Figure 7.2. The horizontal deformation of the base isolation layer is passed from the "Coordinator" to all substructures, and the restoring force obtained from each substructure is returned to the "Coordinator" to check the balance. This process is defined as closed-loop control by which both equilibrium and compatibility are strictly satisfied.

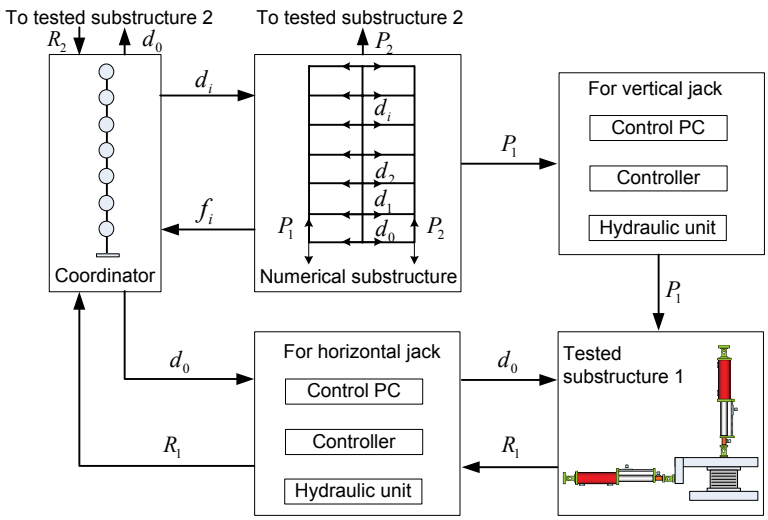


Figure 7.2. Example of combined closed-loop and open-loop control

Theoretically, the compatibility and equilibrium shall be satisfied for all degrees of freedom at the boundaries. In the above example, the isolators are always in compression, and the axial pressure has significant influence on the horizontal behavior of the isolators. Nonetheless, the axial stiffness of the isolators is so large that the axial deformation is small and thus has little effect on the overall structural responses. If the axial deformation is also treated by the closed-loop control, the high axial stiffness of isolators may result in facility control difficulty. One compromise is to apply the force control in the axial direction, and the target force is obtained from the numerical substructure at the end of the previous step, while the axial deformations of the isolators are not necessarily fed back to the "Coordinator" to strictly satisfy compatibility. Therefore, the physical boundary implementation is significantly simplified. By this treatment, the effect of the axial load on the horizontal behavior of isolators can be reproduced as close as possible, although the vertical displacement compatibility is not satisfied. This is referred to here as open-loop control.

## 7.4 Target Structure and Substructure Validation

The Hyogo Earthquake Engineering Research Center of Japan (E-Defense) conducted a full scale 3-D earthquake shaking table test of a four story steel moment frame shown in Figure 7.3 [14]. The structure was designed following the typical Japanese seismic design procedure and the member sections are listed in Table 7.1. The structure was excited in three dimensions using the Takatori acceleration record at 5, 20, 40, 60 and 100% amplitude. At the 100% amplitude, the structure collapsed primarily in the longitudinal direction by forming a first-story mechanism consisting of the local failure of the first story columns at the top and bottom ends. One objective of this study was to verify if hybrid tests can be used to reproduce the collapse behavior observed on the earthquake simulator. However, to physically implement a hybrid test considering laboratory limitations, only the primary structural steel frame is considered with unidirectional loading. The concrete slabs and nonstructural systems in the shake table tests are not included, though the concrete slabs are approximately accounted for by selecting a beam section stiffness that considers the composite action of the slab and beam.

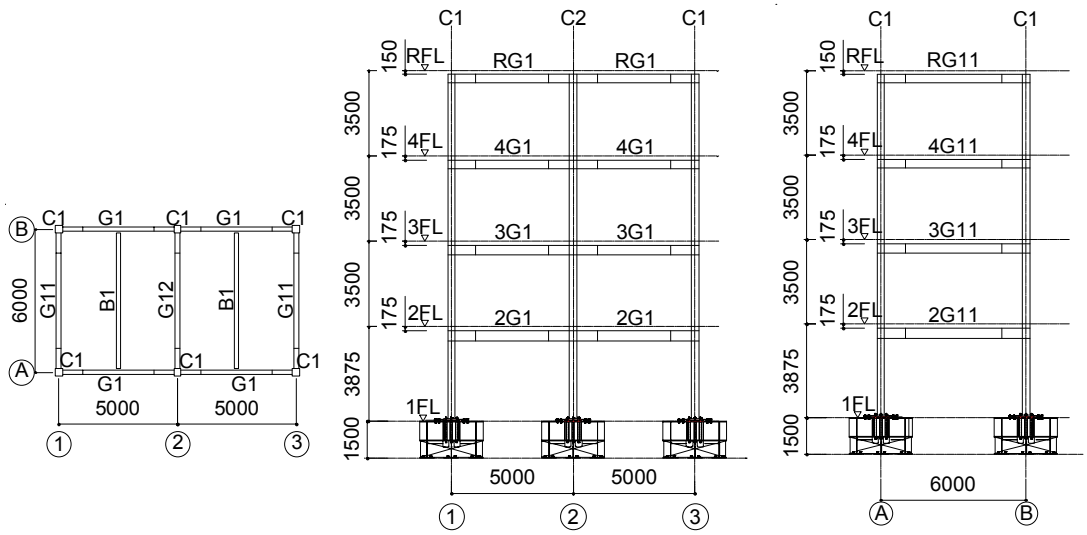


Figure 7.3. Four-story steel moment frame tested at E-Defense

Table 7.1. Section of each structural member (Units: mm)

| Beam (SN400B) | | | | Column(BCR295) | |
|---|---|---|---|---|---|
| Story | G1 | G11 | G12 | Story | C1, C2 |
| R | H-346×174×6×9 | H-346×174×6×9 | H-346×174×6×9 | 4 | BOX-300×300×9 |
| 4 | H-350×175×7×11 | H-350×175×7×11 | H-340×175×9×14 | 3 | BOX-300×300×9 |
| 3 | H-396×199×7×11 | H-400×200×8×13 | H-400×200×8×13 | 2 | BOX-300×300×9 |
| 2 | H-400×200×8×13 | H-400×200×8×13 | H-390×200×10×16 | 1 | BOX-300×300×9 |

### 7.4.1 Flexible implementation of substructures

In the E-Defense shaking table test, it was found that the structure collapsed by forming a story mechanism at the lower level with plastic hinges at the top and bottom of all first story columns. The beams and upper story columns had relatively limited damage. Therefore, in this hybrid test, the experimental substructures focused on the first story columns with the remainder of the upper stories simulated numerically. Assuming just the columns were tested as shown in Figure 7.4 (a), there are seven degrees of freedom at the boundaries among all substructures, if considering the same horizontal deformation at the first story level. This horizontal deformation is to be implemented in the closed-loop control because the reaction forces obtained from the substructures are fed back to the coordinator to maintain the compatibility and equilibrium requirements.

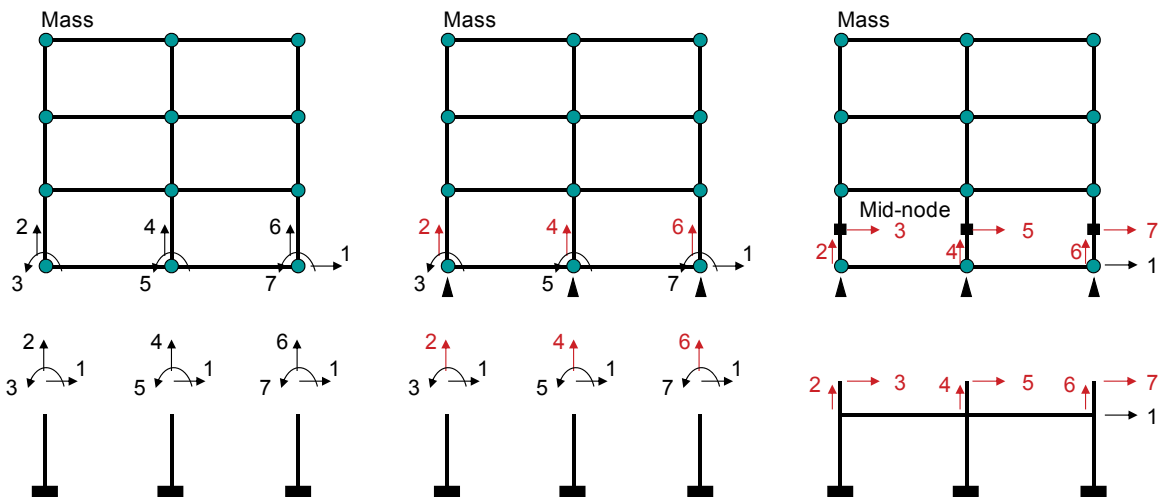


(a) Exact boundary condition (b) Vertical incompatibility (c) Released rotations

Figure 7.4. Flexible implementation of boundary degrees of freedom

Control of stiff axial deformations is challenging because of the limited control resolution of actuators. Since the axial deformation of the first story columns have limited influence on the responses of the superstructure, it is acceptable to neglect this vertical compatibility. However, the axial force is important as it can affect the local failure and global collapse of the first story column. Therefore, these axial deformations are implemented in the open-loop control as shown in Figure 7.4 (b). The vertical displacements of the boundary nodes of the numerical substructure are restrained and the corresponding reaction forces are collected and sent to the tested substructure for

physical loading using force controlled actuators. The axial deformations of the columns of the tested substructure were not fed back to the numerical substructure. This simplification avoids iterations in the axial direction, at the expense of not explicitly satisfying compatibility with the column axial deformations.

The laboratory loading mechanism is further simplified through an innovative substructuring approach with overlapping domains between the numerical and experimental substructures. The boundaries of the physical substructures are extended to the mid-height of the second story columns, as shown in Figure 7.4 (c). Hinges are assumed at the mid-height of the second story columns only for the experiment. Note that the experimental and numerical substructures have overlapping members at the lower half of the second story. The behavior of the second story is obtained from the numerical model only since numerical studies indicate that when hinges are assumed at the substructure boundaries, the distribution of stresses and strains have large localized errors near the assumed hinges [13]. Thus, the experimental response of the half-story columns at the second floor may not be reliable. The supplemental members such as beams and second story half columns in the specimen have the same sections as those in the numerical substructure and serve an important role in transferring the shear and moment at the top end of the panel zone to the first story specimen. By applying the displacements obtained from the numerical substructure to the corresponding second story mid-nodes in the tested substructure, the rotation at the top ends of the first story columns can be approximated to account for other flexibilities in the system. Further, the actual panel zone and beam behavior can be observed experimentally to capture other potential collapse mechanisms within the frame.

### 7.4.2 Interaction between substructures

The interaction between substructures is summarized as Figure 7.5, where the iterative predictor-and-corrector method associated with the flexible test scheme is illustrated. The predicting procedure predicts the horizontal displacement at the first story level only, assuming the tested substructure behaves linearly in the current increment. Once a force balance is achieved at this degree of freedom, does the physical loading initiate while the numerical substructure waits. The target horizontal displacements, including the first story level and the mid-point of the second story columns, and the target axial forces are collected from the numerical substructure output and sent to the tested substructure. Once the physical loading is completed, the restoring forces of the first story columns are measured and fed back to the “Coordinator” to examine equilibrium, where the correcting procedure is applied to minimize the unbalance caused by the nonlinearity of the tested substructure.

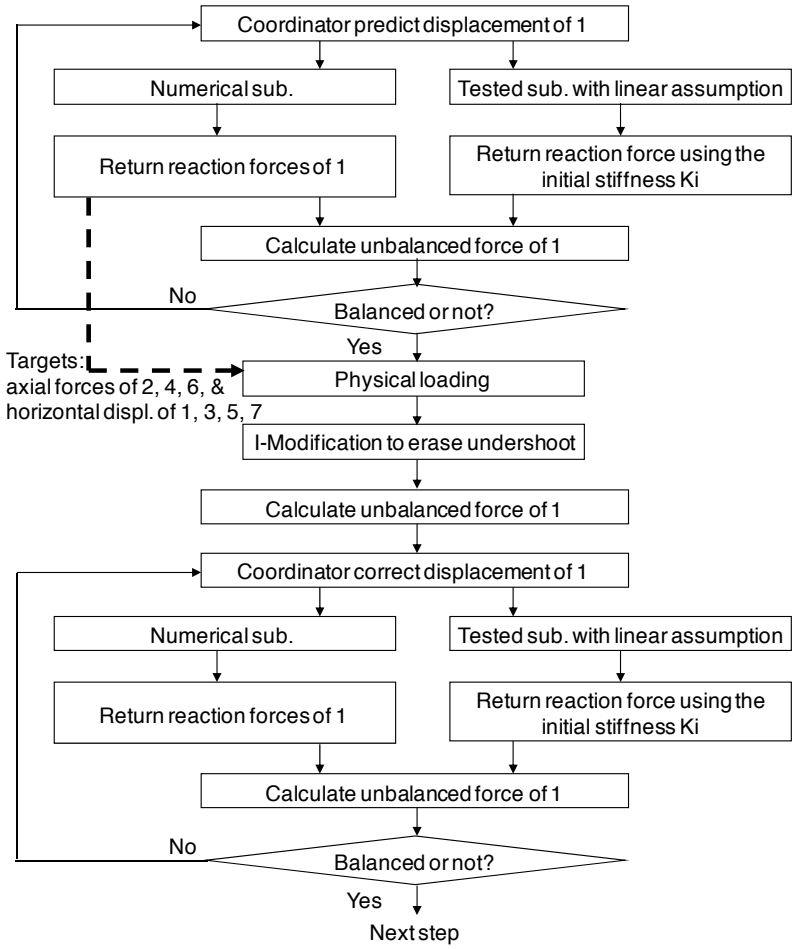


Figure 7.5. Interaction between numerical and tested substructures in the predictor-and-corrector test procedure

### 7.4.3 Numerical evaluation the flexible test scheme

Considering equipment and space limitation of structural laboratories, the tested substructure is further partitioned into two parts at the mid-span of the right beam. The complete frame and locations where hinges are assumed are shown in Figure 7.6 (a). A supplemental link shown in Figure 7.6 (a) and (b) at the assumed hinge between two substructures enforces vertical compatibility, through a mechanical rather than an actuated device. The use of this supplemented link was examined to provide acceptable results in a numerical study [13]. In order to further examine the hinge assumptions and approximate flexible test scheme, a round of pure numerical simulation was conducted with all substructures numerically modeled using OpenSEES [16]. Each beam and column was simulated by a beam element with concentrated plasticity. To consider the floor slab contribution, the stiffness and strength of each beam was revised based on the measurement from the full-scale shaking table test [17]. A lumped mass was concentrated at each beam-to-column joint. To reproduce the collapse behavior, geometric nonlinear behavior was also considered. Since all masses were modeled in the numerical substructure, the analysis of each tested substructure was actually a static process. The JR Takatori ground motion at various amplitude scales was used for the numerical simulations. Only 60% results are presented here.

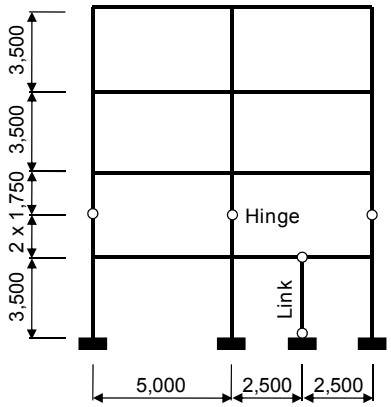


(a) Numerical model with hinges

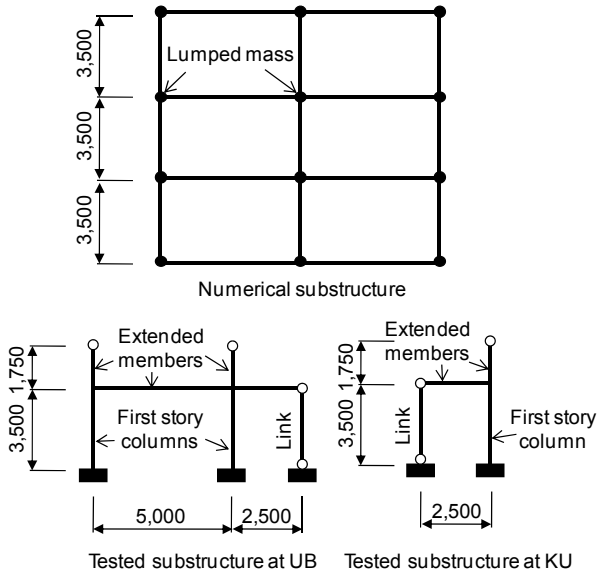


(b) Numerical substructures

Figure 7.6. Substructures for numerical hybrid simulation

Figure 7.7 shows the displacement responses of the first story and roof level for a full frame model, the model with hinges (Figure 7.6 (a)) and the approximate boundary treatment by means of the flexible test scheme (Figure 7.6 (b)). To quantify errors from these assumptions,, the peak displacement are compared and listed in Table 7.2. Compared with the overall numerical analysis, the model with hinges has a peak displacement difference of 1.91 mm at the first story, about 3.18% of the amplitude, and the difference at the roof level is 1.32 mm, approximately 0.62% of the amplitude. The influence of the flexible test scheme is slightly larger, but within acceptable limits. In terms of the peak displacement, the difference at the first story level is 2.96 mm, about 4.93% of the amplitude, and 12.11 mm at the roof, about 5.68% of the amplitude.

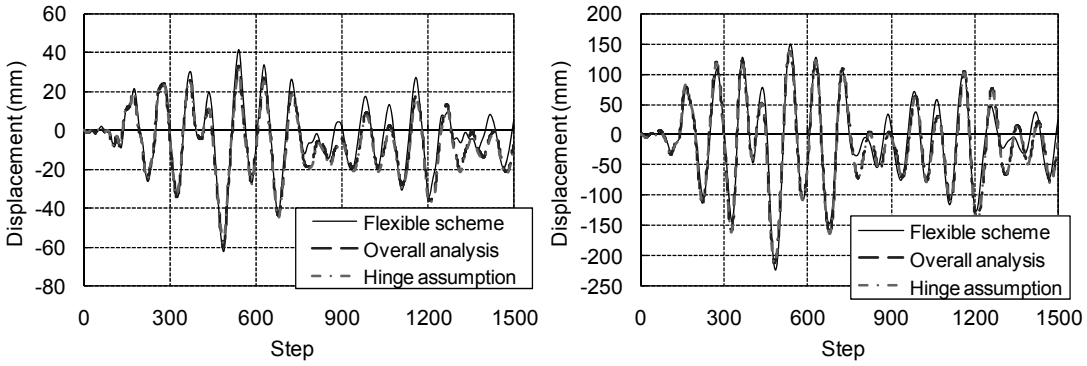


(a) First story level (b) Roof level

Figure 7.7. Comparison of displacement responses of numerical studies

Table 7.2. Error analysis between numerical studies (unit: mm)

| | First story level | | Roof level | |
|---|---|---|---|---|
| | Max. displacement | % Error | Max. displacement | % Error |
| Overall analysis | -59.99 | 0 | -213.06 | 0 |
| Model with hinges | -58.08 | 3.18 | -214.38 | 0.62 |
| Hybrid simulation | -62.95 | 4.93 | -225.17 | 5.68 |

## 7.5 Distributed Hybrid Test

The objectives of this study are to demonstrate the capability of the hybrid test system to reproduce the collapse behavior of a structure and to verify the effectiveness of the flexible boundary implementation. For these purposes, a round of substructure hybrid tests was conducted internationally between Structural Engineering and Earthquake Simulation Laboratory of University at Buffalo and the structural laboratory of Disaster Prevention Research Institute of Kyoto University. The test results were compared with those obtained from the full-scale earthquake-simulator test at E-Defense.

### 7.5.1 Specimens at different locations

The entire structure was partitioned into three substructures as shown in Figure 7.6(b). The superstructure was simulated numerically by OpenSEES while the remaining two were tested at the laboratories of University of Buffalo (UB) and Kyoto University (KU), respectively. The specimen at UB consisted of one and half bay by one and half story, while the KU specimen consisted of one-half bay by one and one-half story height. To reproduce the damage progress and the collapse behavior, the specimens were designed as half-scale models following similitude. The measured strength and stiffness from the shaking table test accounting for the concrete slab effect were used to determine the specimen sections, where the material difference and the welding detailing were taken into consideration. The columns and panel zones were scaled based on the geometry of the sections. The beams were designed as reduced section beams with the length and minimum flange width of the reduced section selected to match the measured strength of the composite beam and slab from the shaking table test. The remainder of the beam section was selected to match the

composite stiffness. A link controlled the deflections of the hanging beam ends considering the assumed point of inflection [13]. All member sections are listed in Table 7.3, and the specimens are shown in Figure 7.8.

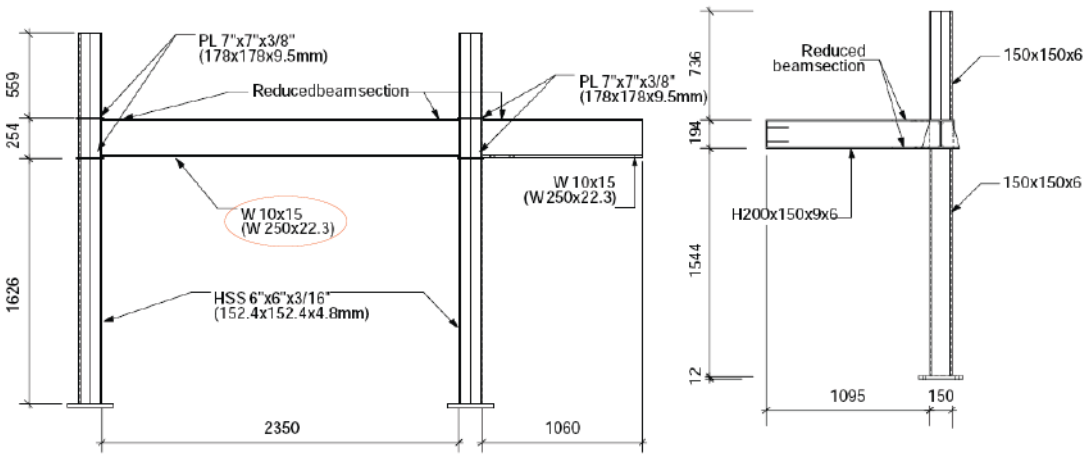


Figure 7.8. Specimens at University at Buffalo (left) and at Kyoto University (Right)

Table 7.3. Sections of specimen members (unit: mm)

| Story | Buffalo | | Kyoto | |
|---|---|---|---|---|
| | Beam | Column | Beam | Column |
| 2 | - | BOX-152.4x152.4x4.8 | - | BOX-150x150x6 |
| 1 | H-254x102x6.9x5.8<br>(RBS254x69x6.9x5.8) | BOX-152.4x152.4x4.8 | H-200x150x9x6<br>(RBS200x110x9x6) | BOX-150x150x6 |

For the specimen located at UB, a support structure was set around the specimen to avoid out-of-plane deformation and provide reactions for actuators. Figure 7.9 (a) illustrates the test setup at UB. The top beam supported by four hinged columns supports two vertical actuators applying gravity loads. The lower beam in the loading plane applied the same horizontal displacements to the top of both second story half-columns. A second horizontal actuator was attached directly to the first story level of the frame. In total, four actuators were used, the lower horizontal one was used to achieve the closed-loop control for the horizontal deformation of the columns; the upper horizontal one was used to control the rotation by means of the extended half column, while the others in open-loop force control provided axial forces for columns considering overturning moments and the P-Delta effects. The photo of the completed setup is shown in Figure 7.9 (c).

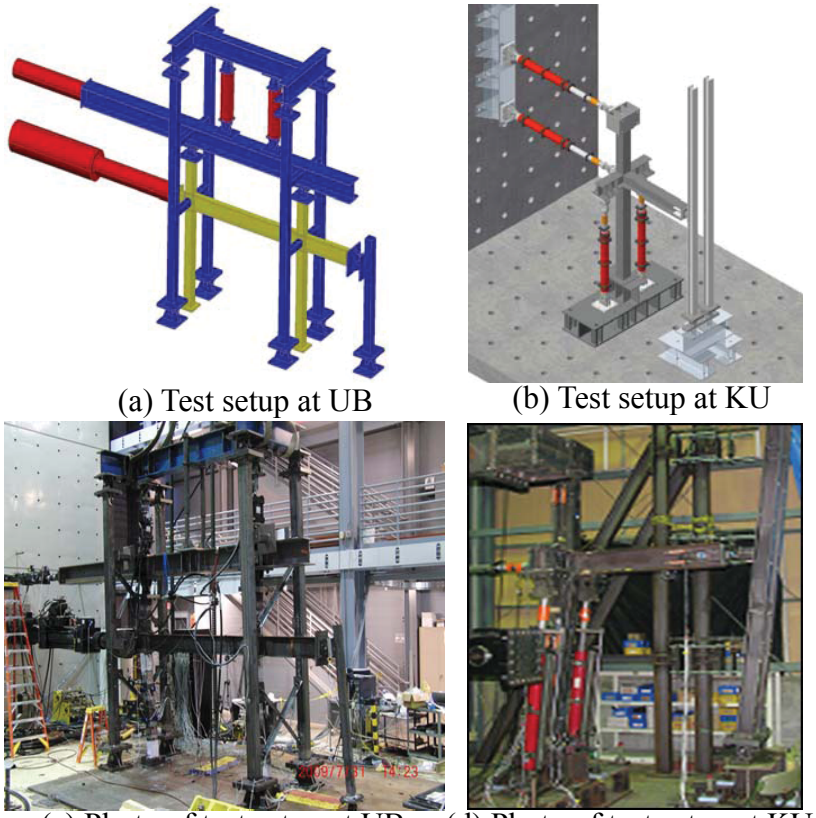

(a) Test setup at UB (b) Test setup at KU

(c) Photo of test setup at UB (d) Photo of test setup at KU

Figure 7.9. Test setups at two laboratories

The specimen at KU, as shown in Figure 7.9 (b) and (d) contained one first-story column as the target component, the extended half column at the second story, and a half-span beam. The links having similar vertical flexibility as the specimen at UB was used to maintain vertical compatibility with the UB specimen. Two wing beams were extended from the panel zone out of the loading plane, and two vertical jacks were connected to them to provide the axial force while maintaining the loading in plane. The two horizontal jacks were used to control the horizontal deformation at the first story and the rotation of the top end of the column, respectively.

### 7.5.2 Instrumentation

Prior to the hybrid test, multiple types of instrumentation were applied to the test specimens in order to collect data during the test. A total of 71 strain gages, 18 potentiometers, and a set of Krypton CMM camera together with 35 LEDs were placed on the test specimen at UB in order to measure strains and deformations in the steel. The strain gages were placed in regions where the steel was expected to remain elastic, as shown in Figure 7.10 (a). The measured strains were used to calculate the moment distribution along each member. The potentiometers, or string pots, were used to directly measure story drift and the rotation at the ends of members where plastic hinges were expected to form, as shown in Figure 7.10 (b). The measurement of the specimen at KU consisted of a total of 15 strain gages and 12 digital displacement transducers, as shown in Figure 7.11 (a) and (b), respectively. The gages were positioned in the elastic region of the column and the beam, similarly as those used in the UB specimen. Digital displacement transducers were placed as pairs to measure the rotation of the plastic hinges on the beams and columns.

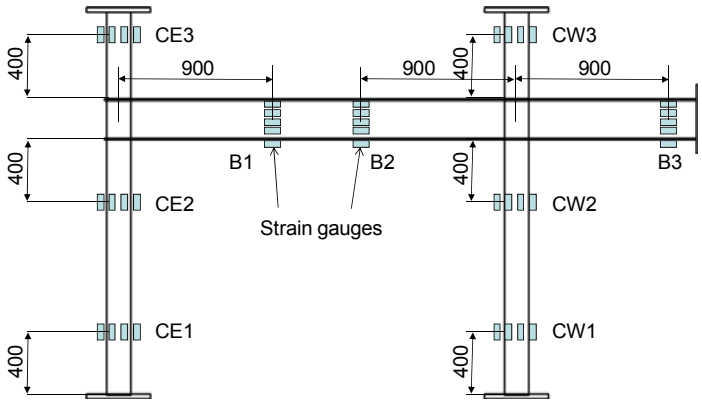


(a) Placement of strain gages

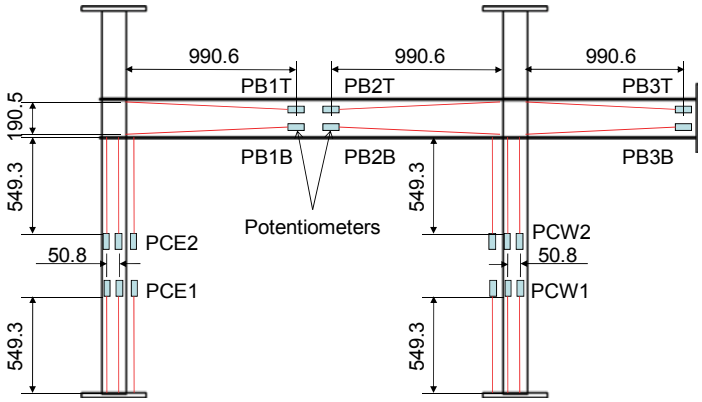


(b) Placement of potentiometers

Figure 7.10. Instrumentation of specimen at UB

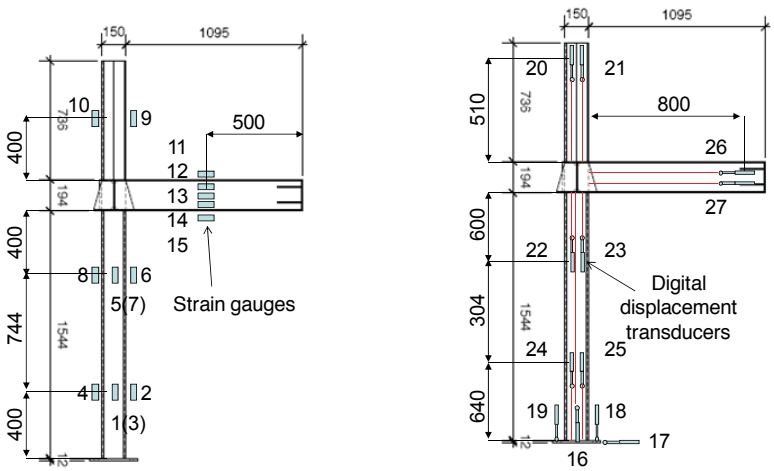


(a) Position of strain gages (b) Placement of transducers

Figure 7.11. Instrumentation of specimen at KU

### 7.5.3 Physical constitution of distributed hybrid test system

The two structural laboratories collaborating in the distributed hybrid test are equipped with different actuator control systems. UB has an MTS Hybrid Simulation Controller with an xPC programmable environment for real-time custom applications and compensation algorithms. The KU facility has a control system manufactured by Riken Kiki Co. Ltd., which works at a low rate of

about 2 mm/s and high control precision of 0.01 mm. Visual Basic is adopted as the programmable environment at the KU structural laboratory. For cooperative testing, a generalized data exchange scheme was developed, which is capable of transferring data through strict firewalls and compatible to both xPC programmable environment and Visual Basic.

Figure 7.12 shows the physical constitution of the distributed hybrid test system. It contained two domains, i.e., UB laboratory and KU laboratory. The "Coordinator" computer was located within UB laboratory domain together with the numerical substructure and one of the experimental substructures. KU laboratory only hosted the corresponding experimental substructure. The data was transferred between these two domains using the generalized data exchange scheme. Since the two domains were each protected by a strict firewall, a proxy computer was set within the UB domain but outside the strict firewall protecting UB domain network. It worked as a messenger to exchange data between the two domains. Two computers, called "StationUB" and "StationKU" respectively, were charged with the predictor-and-corrector scheme, the data exchange and communicating with the experimental control hardware at each site. The target displacements and forces were transformed from the global coordinates to the local jack coordinates in the "StationKU" computer, and directly sent to the control computers to each loading facility. The UB domain, utilized an intermediate Matlab application to transfer the data to the xPC controller.

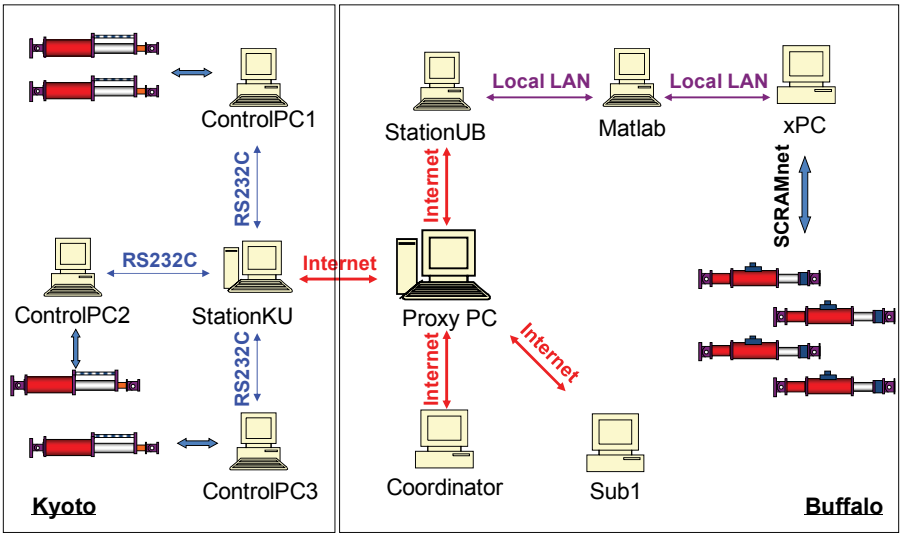


Figure 7.12. Physical implementation of internationally distributed hybrid test system

### 7.5.4 Test results

**Global response and error analysis**

The 1995 JR Takatori earthquake record was applied to the specimen, beginning at 20% magnitude, then 40% and 60%. Eventually, the full strength 1995 JR Takatori earthquake record was applied to test specimens, which induced local buckling in the columns leading to global collapse.

The experimental and numerical data was analyzed in an effort to identify the key sources of error between the 3D E-Defense shake table test and the 2D distributed hybrid test with substructures. Errors are expected in the numerical modeling assumptions and experiments

including: two dimensional modeling of the steel structure, approximate boundary implementation using both hinge assumption and flexible test scheme, and experimental errors and material variability in the distributed hybrid test. To quantify these errors, the displacement time histories of the first story and the roof levels using the 60% Takatori ground motion record are shown in Figure 7.13. The plot compares the hybrid test results, the E-Defense earthquake simulator test, the 2D base numerical model, and the numerical hybrid simulation (hybrid test framework with numerical models of experiments). The peak displacements and percent errors are listed in Table 7.4. At the first story, there is 18.5%, 14.5%, and 22% error going from a 3D E-Defense shake table test to a 2D overall numerical model, the numerical hybrid simulation and the hybrid test, respectively, while the differences are 9%, 15%, and 22% at the roof level. The difference between the 3D E-Defense test and the 2D overall numerical model indicates that the model simplifications, such as the reduction of loading directions, nonstructural components, and concrete slabs, result in the major part of the error, while the boundary approximation and the experimental variability are relatively minor contributors.

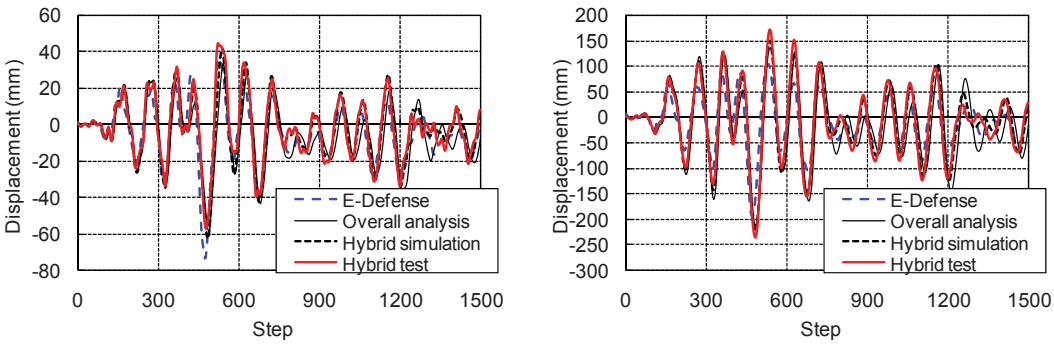


(a) First story level (b) Roof level

Figure 7.13. Comparison of displacement responses of experimental studies

Table 7.4. Error analysis of experimental analyses (Unit: mm)

| | First story level | | Roof level | |
|---|---|---|---|---|
| | Max. displacement | %Error | Max. displacement | %Error |
| E-Defense | -73.65 | 0 | -195.56 | 0 |
| Overall analysis | -59.99 | 18.53 | -213.06 | 8.95 |
| Hybrid simulation | -62.95 | 14.53 | -225.17 | 15.14 |
| Hybrid test | -57.64 | 21.73 | -237.71 | 21.55 |

The test control accuracy is shown in Figure 7.14 in terms of the difference between the target and measured displacements in the first story jack and actuator for two specimens under the 60% Takatori test. The tolerance of the displacement control was set at ±0.1 mm. According to the figure, the average error resides within this range, demonstrating an accurate control of the test, despite some particular cases where the error spikes to 0.6 mm at KU and 1.0 mm at UB. Those spikes largely occurred at the moment when the jack or actuator ran at a fast loading rate, thus the control

response was relatively slow which was believed to be reason for these spikes. However, the associated force at these instances was small, resulting in negligible energy input into the system, that the effect on structural responses could be neglected.

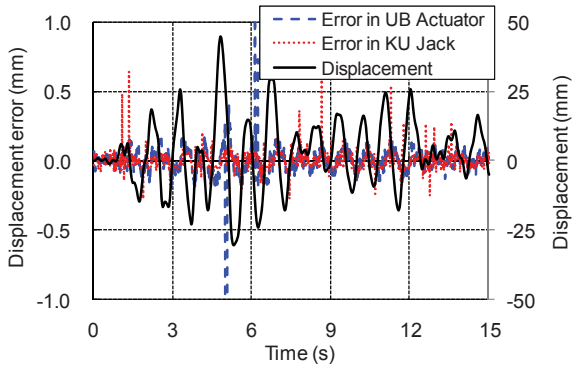


Figure 7.14. Facility control error

**Distribution of stresses**

In order to further examine the selected substructures and the modeling assumptions, the distributions of stresses in the frame were compared during the hybrid test and the E-defense earthquake simulator tests by means of moment diagrams. The moment diagrams were calculated at the peak displacement response for the distributed tests using the experimental strain data. For the E-Defense test, the moments were calculated at the same time step that the moments for the distributed test were calculated. In both tests, strain gauges were located at the one-third and two-thirds length of the beams and columns where the members are assumed to remain elastic. A linear moment diagram is then fitted to these two points to obtain the moment diagram for the member and extrapolate the moment at the member ends. The member end moments at peak displacements calculated for the 60% and 100% Takatori tests are listed in Table 7.5 where the moment $M_{ij}$ corresponds the moment at end $i$ of the element connecting nodes $i$ and $j$. For the 60% Takatori tests, the moment in the first story columns are at most 30% different from the E-Defense test results. Errors in the 100% Takatori simulation are much larger due to the large levels of nonlinearity. The material variability between the E-Defense specimen and the one used for the hybrid test substructures is likely a major contributor to these errors.

Coupon specimens were extracted from the beam and column elements and tested following standard procedures for determining tensile properties of steel. The resulting yield stress and ultimate stress for the various experimental specimens are compared in Table 7.6. Note that the steel material used in the hybrid test substructures had beams with at least 9% lower strength and columns with 30% greater stress capacity, which results in larger ultimate moment capacities. In particular, the strengths of the columns are 52% and 26% larger than the E-Defense columns for the KU specimen and UB specimen, respectively.

Table 7.5. Comparison of moment diagram between distributed test and E-Defense test (Unit: kNm)

Location reference

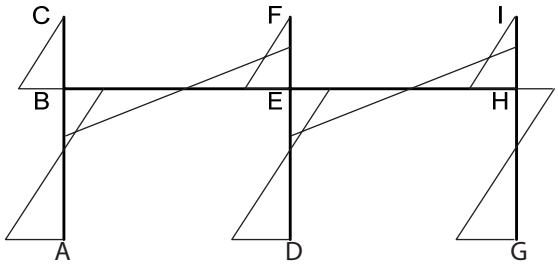


| EQ level | 60% Takatori | | | 100% Takatori | | |
|---|---|---|---|---|---|---|
| Location | Hybrid test | E-Defense | % Error | Hybrid test | E-Defense | % Error |
| $M_{AB}$ | 370 | 353 | 4.8 | 312 | 229 | 36.2 |
| $M_{BA}$ | 200 | 289 | 30.8 | 415 | 315 | 31.7 |
| $M_{DE}$ | 405 | 351 | 15.4 | 335 | 187 | 79.1 |
| $M_{ED}$ | 320 | 317 | 0.94 | 413 | 284 | 45.4 |
| $M_{GH}$ | 453 | 380 | 19.2 | 453 | 191 | 137.2 |
| $M_{HG}$ | 344 | 280 | 22.9 | 344 | 304 | 13.2 |

**Capability to trace collapse**

The first story shear force and story drift angle relationships in the longitudinal direction at the 60% and 100% JR Takatori records for the distributed test and E-defense test are shown in Figure 7.15 (a) and (b), respectively. For the 60% JR Takatori distributed test only the first 5 seconds of the test are shown including the peak displacement. During this test, an actuator interlock was triggered at UB, which temporarily shut down the actuators. The test setup was recovered and the test continued, but with some temporary offset in the measured force data. From the hysteretic behavior, it is evident that similar strengths were achieved for both tests, but smaller peak displacements were observed for the distributed test. During the 100% JR Takatori distributed test, the peak story drift angle is 0.017 radians at the first story at a story shear of 788 kN. Figure 7.15 (b) shows a substantially higher strength for the distributed tests compared to the shake table test. After the 60% test, the shake table specimen appeared to have suffered much more damage as indicated by the loss in strength in the 100% test. These differences observed in behavior may be due to several reasons, the most important reason being the simplification of the hybrid test such as loading in only one direction. Additionally, the hybrid test did not include the non-structural components and concrete slabs as in the E-Defense tests that accumulated damage under smaller ground motions. Further, the boundary condition simplification adopted for the distributed test such as restraining the vertical deformations in the numerical substructure and neglecting their influence in large deformations, may have contributed to these differences. Unavoidably, there were also differences in the material properties in the hybrid test specimens, as indicated in Table 7.6.

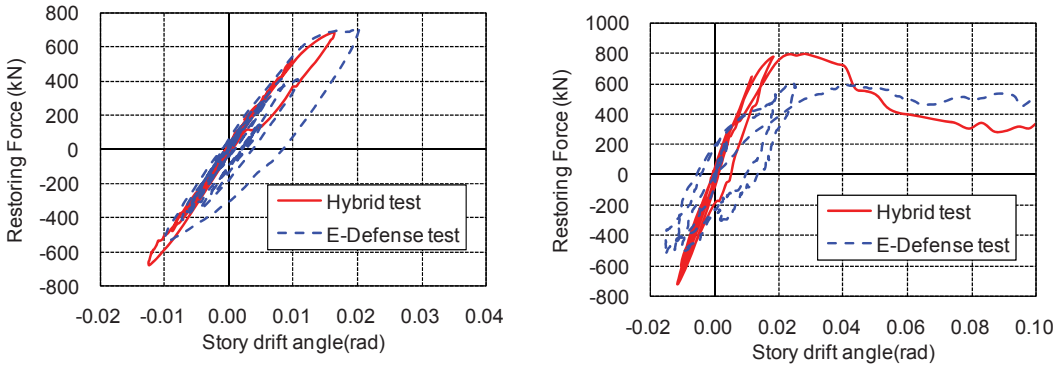


( a) 60% Takatori (b) 100% Takatori

Figure 7.15. Comparison of hysteretic behavior at first story between hybrid test and E-Defense test

Table 7.6. Material properties

| | E-Defense | | KU specimen | | UB specimen | |
|---|---|---|---|---|---|---|
| | Beam | Column | Beam | Column | Beam | Column |
| Yield Stress (MPa) | 373.0 | 331.0 | 328.5 | 443.5 | 340.0 | 447.9 |
| Ultimate Stress (MPa) | 482.0 | 423.0 | 459.0 | 510.1 | 440.3 | 545.5 |
| Mp (kNm) | 619.8 | 483.7 | 697.6 | 734.4 | 736.0 | 610.4 |

The collapse mechanism for the internationally distributed hybrid test was a first story mechanism with local buckling and hinging at the top and the bottom of the first story columns. Figure 7.16 compares the collapse mechanism for the E-Defense test and the distributed hybrid test. It can be seen, that similar failure modes were observed for the center column of the frame. The difference in hinge rotations is due to the different limits set for each test; the hybrid test was not allowed to exceed 10% drift, whereas twice the drift was allowed on the shake table test.

(a) E-Defense Test (b) Distributed Hybrid Test

Figure 7.16. Collapse mechanism comparison

### 7.5.5 Efficacy of the proposed system

The hybrid test framework used in this study is in essence an iterative predictor-corrector method. In spite of the significant nonlinearity and strength degradation, convergence was always achieved after 3-4 iterations, as shown in Figure 7.17 (a) and (b) for 60% and 100% Takatori ground motion, respectively, in which the predicting procedure used 1-2 iterations, while the correcting took about 1-2 for mild nonlinearity, and 3-4 for large responses. One spike of 15 iterations occurred at around 300th step for 60% test, because of the yielding at that instant. Another spike of 24 iterations was observed at around 500th step, when the structure began to collapse. The trial and error procedure finally converged, which demonstrates the proposed procedure is reliable and thus suitable for structural collapse simulation.

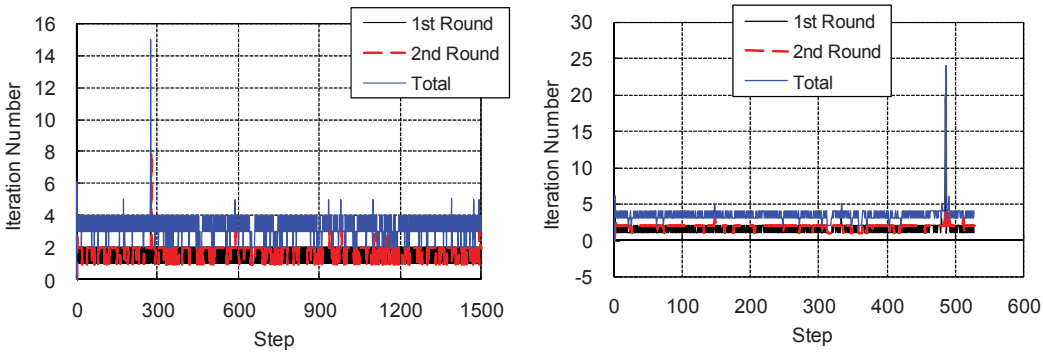


(a) 60% Takatori (b) 100% Takatori

Figure 7.17. Number of iterations employed in predictor-corrector procedure

### 7.5.6 Challenges in Conducting Distributed Tests

A collaborative hybrid simulation to collapse is a significant undertaking and many difficulties were encountered through this project. These difficulties are much more administrant, rather than technical. First are the unit and material differences between the industries in Japan and U.S. Construction of the specimens locally, to avoid major shipping expenses meant that the same section dimensions and mechanic properties cannot be guaranteed? In this particular case, the material used for KU specimen was 30% higher in strength than the specimen of UB, which resulted in different failure mode for KU specimen and expected differences in the overall responses. Time difference is another concern. There is also a twelve hour difference between Japan and the Eastern U.S. Since one test may take a few hours, it becomes necessary for one lab works through the night. The operators may make some mistakes because they are working in an unusual period. These difficulties shall be of significant concerns to the project administrator.

## 7.6 Summary and Conclusions

A distributed online hybrid test was conducted in this chapter to trace the collapse behavior of a steel moment frame. Two key issues were investigated: (1) the implementation of the boundaries between substructures; and (2) the capability of the distributed hybrid test framework to capture the

realistic collapse behavior of a structure. With these two objectives, both numerical and experimental studies were conducted to examine the boundary implementation and to explore the collapse behavior by comparison to a four-story steel moment frame which was tested at E-Defense, Japan. Several observations were summarized as follows:

(1) The boundary implementation is a key issue in the distributed hybrid test. In order to achieve the highest precision, both equilibrium and compatibility shall be satisfied at all of the boundary degrees of freedom. The reality, however, is that it is difficult to control stiff degrees of freedom, and the loading facilities and test space are sometimes limited to control all degrees of freedom. Therefore, the simplified implementation is often adopted. The flexible boundary implementation proposed in this study was verified effective and accurate enough through both numerical and experimental examinations.

(2) The distributed hybrid test frame used in this study encapsulated each substructure with a standard interface. A significant advantage of this is to increase compatibility with numerical substructures using different finite element programs and more important, laboratories with different hardware equipment. In this distributed test, two different types of facilities: servo-controlled hydraulic actuators and simply-controlled jack system, were employed. Each laboratory developed its control software separately, but collaborated smoothly without any malfunction.

(3) Even though the hybrid test included several simplifications such as unidirectional loading and boundary assumptions, a similar response and collapse mechanism was observed in the distributed hybrid test. Examination of the local distribution of stresses in the experimental substructure reveals that the substructuring assumptions were adequate in capturing the distribution of forces in the frame. While the hybrid test approach cannot match the realism of full-scale earthquake simulator testing, it can provide a cost-effective method for evaluating the seismic performance of buildings at large scales with the capabilities available in many laboratories.

# REFERENCES


[1] Takanashi K, Udagawa K, Tanaka H. (1978), "Earthquake response analysis of steel frames by computer-actuator on-line system". *Proceedings of the 5th Japan Earthquake Engineering Symposium*, pp. 1321 – 1328.

[2] Mahin SA, Shing PB. (1985), "Pseudodynamic method for seismic testing". *Journal of Structural Engineering*, ASCE **111**(7), pp. 1482 – 1501.

[3] Nakashima M, Akazawa T, Igarashi H. (1995) "Pseudo-dynamic testing using conventional testing devices". *Earthquake Engineering and Structural Dynamics* **24**, pp. 1409 – 1422.

[4] Park DU, Yun CB, Lee JW, Nagata K, Watanabe E, Sugiura K. (2005) "Online pseudo-dynamic network testing on base-isolated bridges using Internet and wireless Internet". *Experimental Mechanics*; **45**, pp. 331 – 343.

[5] Takahashi Y, Fenves GL. (2006) "Software framework for distributed

experimental-computational simulation of structural systems". *Earthquake Engineering and Structural Dynamics*; **35**, pp. 267 – 291.

[6] Yang YS, Wang SJ, Wang KJ, Lin ML, Weng YT, Cheng WC, Chang YU, Tsai KC, Lau DT, Hsieh SH, Lin FP, Lin SY (2006). "Network system for a transnational collaborative pseudo-dyanmic experiment on a DSCFT pier bridge system". *Proceedings of 8th National Conference on Earthquake Engineering*, San Francisco, USA.

[7] Mosqueda G, Stojadinovic B, Hanley J, Sivaselvan M, Reinhorn MA. (2008), "Hybrid seismic response simulation on a geographically distributed bridge model". *Journal of Structural Engineering*; **134** pp. 535 – 543.

[8] NEESinc—George E. Brown Jr. Network for earthquake engineering simulation. http://www.nees.org (24 January, 2007).

[9] Kwon OS, Elnashai AS, Spencer BF. (2008) "A framework for distributed analytical and hybrid simulations". *Structural Engineering and Mechanics*; **30**: pp. 331 – 350.

[10] Schellenberg A, Yang T, Mahin S, Stojadinovic B. (2008) "Hybrid simulation of structural collapse". *Proceedings of the 14th World Conference on Earthquake Engineering*, Beijing, China.

[11] Wang T, McCormick J, Yoshitake N, Pan P, Murata Y, Nakashima M. (2008), "Collapse simulation of a four-story steel moment frame by a distributed online hybrid test". *Earthquake Engineering and Structural Dynamics*, **37**: pp. 955 – 974.

[12] Schneider PS, Roeder WC. (1994) "An inelastic substructure technique for the pseudodynamic test method". *Earthquake Engineering and Structural Dynamics*; **23**: pp. 761 – 775.

[13] Mosqueda G, Cortes-Delgado MD, Wang T, Nakashima M. (2010) "Substructuring techiniques for hybrid simulation of complex structural systems". *9th US National/10th Canadian Conference on Earthquake Engineering,* Toronto, Canada.

[14] Suita K, Yamada S, Tada M, Kasai K, Matsuoka H, Sato E. (2008) "Results of Recent E-Defense Tests on Full-Scale Steel Buildings: Part 1 --- Collapse Experiments on 4-Story Moment Frames"*, ASCE Conf. Proc*. 314, 266 (2008), DOI:10.1061/41016(314)266.

[15] Pan P, Tomofuji H, Wang T, Nakashima M, Ohsaki M, Mosalam KM. (2006). "Development of peer-to-peer (P2P) Internet online hybrid test system". *Earthquake Engineering and Structural Dynamics*; **35**: pp. 867 – 890.

[16] OpenSees version 1.7 user manual, Pacific Earthquake Engineering Research Center, University of California, Berkeley. http://opensees.berkeley.edu. 2006.

[17] Akazawa M. (2007) "Collapse behavior and non-structure damage assessment of a full-scale four story steel building by shaking table test". *Master thesis,* Kyoto University.

# CHAPTER 8

## Summary and Conclusions

In seismic design of steel structures, passive dampers have gained popularity as a response to the shortcomings of conventional structural design. Thin steel-plate shear walls may serve as passive dampers in both new construction and seismic upgrade of existing structures. However, unless heavily stiffened, the response of thin steel-plate shear walls is commonly accompanied by significant pinching in their hysteretic response, although the strength deterioration is compensated for by the development of a tension field. An passive damping device that consists of a steel plate shear wall with vertical slits (SW hereafter) has been previously devised as an extension of thin-plate shear walls. In this system, the steel plate segments between the slits behave as a series of flexural links, which undergo large flexural deformations relative to their shear deformation, providing a ductile response without significant out-of-plane stiffening of the wall.

This study tries to extend the unique capacity of SWs so that they can also serve as a tool for structural condition assessment. Structural condition assessment focuses on techniques for evaluating the integrity of a structure after an earthquake event to ascertain the danger that it represents for re-occupation of the building. Since its introduction, this evaluation has been performed through health-monitoring or through performance-evaluation analyses that rely on detailed computer models of the structure. Unfortunately, the required technologies remain untested against actual large earthquakes, and the cost of implementing this technique restricts its use to important structures, such as large spatial structures, bridges, dams, and high-rise buildings. The small number of sensors used in these structures is only sufficient to identify the existence of damage by observing global changes in the vibration modes and frequencies. These restrictions encourage the development of a simpler method of estimating the damage sustained by a structure.

This dissertation consists of eight chapters. Chapter 1 is the introduction, including the background and objectives of the dissertation. Chapter 2 presents a summary of the previous research conducted on steel shear walls up to date, and Chapter 3 presents the conceptual work to achieve condition assessment capabilities through the tracing of strains. Design equations and a numerical verification of the equations are also presented. Chapter 4 presents a practical application of the slit wall design and the testing of a structure with an online testing scheme, Chapter 5 presents an alternative method of achieving condition assessment capabilities through the tracing of the inelastic buckling behavior of the flexural links in slit walls. Chapter 6 presents a means of recording through the flaking of paint the strain patterns that develop in the slit walls presented in

Chapter 3. Chapter 7 presents an extension of the online testing system used in Chapter 4 in order to geographically distribute the physical testing substructures and the application of this system to the reproduction of the collapse of a steel frame building. A summary and major findings obtained from each component of this dissertation is presented below.

***Summary of Previous Research***

Experimental and analytical research on thin unstiffened SPSWs has shown that the SPSW system possesses high initial stiffness, ultimate strength, and ductility, as well as stable hysteresis curves and a large energy dissipation capacity. It has been recently demonstrated that the use of perforations or the cutting of slits in the plates reduces the strength and stiffness of the walls, and thus the demand for the boundary framing members.

Two different approaches have been considered to estimate the strength and stiffness of SPSWs: one approach approximates the behavior of the tension field in the steel plate with strips that work in tension and model the inelastic behavior in the material properties. This approach has been used to design unstiffened SPSWs, either with or without perforations. In the second approach, intended for the design of steel plates with slits, the slits prevent the formation of the tension field, and allow the links formed between the slits to behave as beam-columns in bending.

Unfortunately, the research conducted on SPSWs has not yet addressed several issues. The first such issue relates to the need of SPSWs to be attached to the boundary frame to develop the tension field. The tension field generates large forces in the boundary members and special provisions have to be taken in the design to avoid damage from taking place in these members. Also, as the SPSW has to occupy the full beam span, no space is left for window or door openings, reducing the possible locations where SPSWs can be installed. Recently some studies have considered the inclusion of openings for utilities but these applications still require the SPSW to be attached to the frame members. A second issue refers to the extension of the research on SPSWs. The research has been focused on element tests, whether simple SPSW specimen or frame assemblies, and FEM analyses. There is yet no record of research of the application of these walls in actual frame buildings subjected to seismic demands.

***Slit Walls with Unequal Slitting***

The conceptual work and analytical formulation of unequally slitted steel shear walls is presented. The slit walls featured an innovative slitting pattern to add condition assessment capabilities without reducing the energy dissipation characteristics of the walls. A parametric study was conducted on individual flexural links to determine their performance. The major findings are summarized as follows:

(1) Unequally slitted steel shear walls retain the damping characteristics of conventional slit walls. Altering the slit configuration generates strain patterns that are unique to specific drift angles.

(2) The strength and stiffness of slit walls can be accurately predicted using a traditional formulation. The behavior of the slit walls can be separated into the behavior of the unslitted and slitted sections and the total behavior of the wall can be computed as the aggregation of the

behavior of these sections. The predictions obtained from the equations developed show good agreement with finite element models.

(3) The out-of-plane deformations that take place in the flexural links can be predicted using the flexural-torsional equations of elastic beams. Furthermore, the drift angle at which buckling develops for specific aspect ratios can be predicted by these equations. Results from finite element models confirm the validity of the aforementioned equations.

***Online Test of a Three-Story Building with Slit Walls***

The seismic simulation of a three-story steel frame with slit walls (SWs) was conducted using an online hybrid test system. The SWs feature an innovative slitting pattern to add condition assessment capabilities without reducing the energy dissipation characteristics of the SWs. The structure is divided into two substructures. The backup frame is treated numerically using OpenSees, while the span featuring the SW is an experimental substructure that is physically tested. Ground motion was imposed on the structure at two different magnitudes. After the online hybrid test was completed, the slit wall specimens were salvaged and further tested under cyclic load.

The major findings are summarized as follows:

(1) During the online test, all unequally slitted SW specimens sustained large ductility (ductility ratios above 3 for the Level 2 ground motions). The shear walls provided the structure with large stiffness and energy dissipation at small (0.47%) drift levels. Fat hysteresis loops without strength deterioration were obtained. Thus, unequally slitted shear walls retained the hysteretic characteristics of conventional slit designs.

(2) A nonlinear finite element analysis gave reasonable predictions of the elastic (within 70% of the experimental value) and post-yield behavior (within 85% of the experimental value) of the SW. The equivalent brace models used in the early prediction model, with properly adjusted strain-hardening properties, were able to accurately duplicate the response of the test structure in the online test (4% error in amplitude for the Level 2 ground motion).

(3) During the cyclic test, the slit walls showed a reduction of approximately 50% in stiffness and maximum strength when compared to the results from the online test. However, fat hysteresis loops were obtained for drift angles up to 3% with pinching only apparent after the second cycle to this amplitude. No deterioration of the maximum strength was observed, even drift angles of 8%

(4) Out-of-plane deformations of the flexural links were evident in both the online test, where the links intended for condition assessment buckled for drift angles of approximately 2%. The buckling of the flexural links in the online test did not translate into pinching for this test. In the cyclic test, the flexural links outside the condition assessment zone buckled for drift angles of 4%.

***Buckling Initiation as a Means for Condition Assessment***

Inelastic buckling of flexural links was predicted and traced to indicate different levels of the maximum story drift obtained during the loading. Two types of flexural links were introduced: (1)

"cushion links", whose purpose was to act as buffers against the propagation of strains throughout the wall, and (2) "monitoring links" whose purpose was to develop out-of-plane buckling after specific lateral drift angles had been achieved. An experimental verification was carried out on two scaled specimens designed to develop out-of-plane deformations at drift angles of 0.5%, 1%, 2%, and 3%. The major findings are summarized as follows:

(1) The buckling behavior of flexural links due to lateral deformations can be predicted by means of finite element analysis with an accuracy of 0.5% in between drift levels. Condition assessment capabilities can be achieved based on the buckling behavior of flexural links.
(2) The spreading of strain in between neighboring monitoring links can be avoided by the inclusion of clusters of cushion links. The width of the cushion cluster should be at least equal to the average width of the monitoring links that the cluster separates. Furthermore, the aspect ratio of the cushion links should be larger than 10 to insure low strain concentrations at the end of the links.
(3) The slit distribution for condition assessment presented in this chapter does not deteriorate the hysteretic performance of the slit wall as a damper device. Damping coefficients up to 0.2 were obtained for drift angles of up to 4.0%. For very large lateral deformations (up to 8% drift angle) the damping coefficient remain above 0.15.
(4) Visual inspection proved to be a fast and accurate method to identify the initiation of buckling behavior in the monitoring links. In the experimental results, visual inspection proved accurate to detect lateral deformations of 0.5%, 1.0% and 2.0%. However, the results obtained from visual inspection did not fully match those obtained from measured out of plane deformations by displacement transducers.

***Paint as a Means for Condition Assessment***

The development of a method to record the spreading of the maximum strains through the surface of a steel plate was presented. A series of tests were conducted on steel coupons under tensile strain in order to identify a strain sensitive paint for condition assessment purposes. Afterwards the paint compound was applied on the surface of three reduced-scale slit wall specimens and tested in an online-hybrid test and under a static loading protocol. The main finding of this chapter can be summarized as follows:

(1) A reliable paint compound, composed of lacquer with a 50% concentration of thinner and with 2 mm wide gridlines cut into the film, was identified as presenting visible responses to strain. The response initiates at strains not higher than 0.4%
(2) The flaking of the paint takes place only in those areas that exceed the flaking strain and does not propagate to lower strain areas. Thus, preserving the maximum strains experienced.
(3) The extension of the strain areas determined by the flaking of the strains agree with the extension of strain areas determined by finite element models. When paint is applied to slit walls, the flaking areas develop in the zones with high strain concentrations. This strain areas can be recorded and later associated to different levels of drift angle.
(4) Pictures of the flaking of paint can be analyzed to determine the extension of the areas where

flaking has taken place. Larger areas of flaking represent larger drift angles to which the slit wall has been subjected. Thus identification of maximum drift angles by means of paint flaking can be achieved.

***Distributed Online Test to Collapse***

A distributed online hybrid test was conducted to trace the collapse behavior of a steel moment frame. Two key issues were investigated: (1) the implementation of the boundaries between substructures; and (2) the capability of the distributed hybrid test framework to capture the realistic collapse behavior of a structure. With these two objectives, both numerical and experimental studies were conducted to examine the boundary implementation and to explore the collapse behavior by comparison to a four-story steel moment frame which was tested at E-Defense, Japan. Several observations were summarized as follows:

(1) The boundary implementation is a key issue in the distributed hybrid test. In order to achieve the highest precision, both equilibrium and compatibility shall be satisfied at all of the boundary degrees of freedom. The reality, however, is that it is difficult to control stiff degrees of freedom, and the loading facilities and test space are sometimes limited to control all degrees of freedom. Therefore, the simplified implementation is often adopted. The flexible boundary implementation proposed in this study was verified effective and accurate enough through both numerical and experimental examinations.

(2) The distributed hybrid test frame used in this study encapsulated each substructure with a standard interface. A significant advantage of this is to increase compatibility with numerical substructures using different finite element programs and more important, laboratories with different hardware equipment. In this distributed test, two different types of facilities: servo-controlled hydraulic actuators and simply-controlled jack system, were employed. Each laboratory developed its control software separately, but collaborated smoothly without any malfunction.

(3) Even though the hybrid test included several simplifications such as unidirectional loading and boundary assumptions, a similar response and collapse mechanism was observed in the distributed hybrid test. Examination of the local distribution of stresses in the experimental substructure reveals that the substructuring assumptions were adequate in capturing the distribution of forces in the frame. While the hybrid test approach cannot match the realism of full-scale earthquake simulator testing, it can provide a cost-effective method for evaluating the seismic performance of buildings at large scales with the capabilities available in many laboratories.

# ACKNOWLEDGEMENTS

First, I would like to express my sincere gratitude to my thesis advisor, Professor Masayoshi Nakashima. Throughout the course of my doctoral studies, his knowledge, foresight and ingenuity were fundamental to the completion of my research. His devotion to his work and to his students are an example to follow. I consider myself fortunate to have had such a kind, generous, and intelligent person as my advisor.

Due gratitude to Professor Yoshio Kaneko and Professor Keiichiro Suita for their kindness to be the members of the dissertation committee, and for their thorough reviews and helpful comments on this dissertation.

Special thanks are due to Professor Toko Hitaka for her readiness to share her extensive knowledge on slit walls. Her kindness and cheerful disposition brought joy to my life in Japan. I wish to thank Dr. Tao Wang, Dr. Jason Mc Cormick and Dr. Masahiro Kurata, for their insightful comments and their great help with my research.

I wish to thank Dr. Yao Cui, Dr. Yulin Chung and Dr. Dimitrios Lignos for their friendship and support during my years as a graduate student.

I am grateful to Mrs. Chisato Gamou, Mrs. Mieko Kimura and Mrs. Tomomi Shinagawa for their kind assistance regarding office matters.

I would also like to show my thanks to my group members, Mr. Takuya Okamura, and Mr. Yosuke Murata for their great assistance on preparing and conducting physical experiments.

I am also grateful to my other colleagues, Dr. Masahiro Ikenaga, Mr. Ryuta Enokida, Mr. Toru Tai, Mr. Shuhai Song, and Miss. Sachi Furukawa for their kindness and help with the daily life in Japan.

Finally, I would also like to thank my family for their love, support, and encouragement during my studies. I would also like to show my sincere gratitude to my wife, for her understanding and selfless support through these years. Without them, this dissertation would not have been possible.